University of Stavanger

Faculty of Science and Technology

Master Thesis

Study program/ Specialization: Petroleum Engineering / Drilling Technology	Spring semester, 2014 Open
Writer: Abdullah Tariq	…… (Writer's signatures)
Faculty supervisor: Mesfin Belayneh External supervisor: Hans Joakim Skadsem	
Title of thesis: **"Wellbore stability in Shale formations"**	
Credits (ECTS): 30	
Key words: Shale Collapse Chemical Activity	Pages: 93 +enclosure: 1 Stavanger, 16.06.2013

Acknowledgements

I would firstly like to thank Mesfin Belayneh; Professor at the University of Stavanger and Hans Joakim Skadsem; External Supervisor from IRIS for their supervision and support throughout my master thesis.

Stavanger, 16th June 2014

Abstract

Well instability in shale formations has been a very major problem due to physiochemical interactions between drilling fluid and formation. In this thesis, chemical, thermal and diffusion effects on the well collapse strength are evaluated in order to investigate the dominating driving forces. A case study on the designed Heidrun well program was also performed in order to study the dynamics of the collapse pressure during drilling phase due to various driving forces.

Table of Contents

List of figures

List of tables

List of abbreviations

EM – Scanning Electron Microscope

FI – Failure Index

1 Introduction

This thesis deals with the well bore stability issues of shale formation with special focus on the transient effect of pore pressure on the well collapse pressure and stress fields. The main driving forces are chemical, hydraulic and thermal effects. For the analysis, a Heidrun well program case study was considered (G. Stjern 2003).

1.1 Background

It is reported that shale makeup 75% of drilling formation where 90% of well instability occurs (Ronald Steiger 1992). Well instability is a major cost factor for the industry. The wellbore instability problems increase the overall drilling budget by about 10% (Aadnøy 2003). The wellbore instability problems are basically well collapse and well fracturing. The problems are caused by shear and tensile failure mechanisms respectively. Several well stability theoretical and experimental studies have been done in the industry today. Despite the efforts and more understanding about the subject, the industry is still facing this problem in shales. This is due to the complex nature of this formation in terms of its transient phenomenon resulting from the physiochemical interaction of rock and drilling fluid. Several models have been derived in order to understand these transient effects in order to adjust the mud weight density accordingly. In a formation where the drilling window is very small, a slight change in pore pressure may cause well fracturing or well collapse. During a drilling operation, the change in pore pressure is due to the physio-chemical interaction between the chemistry of drilling fluid, well pressure and temperatures. This change in pore pressure and temperature causes a change in the stress concentrations around the wellbore. Therefore the overall effect is modifying the original well collapse and fracture strength. The hydraulic diffusion, chemical and thermal effects are transient effects. Therefore, a good model is needed which is capable of predicting these effects. In this thesis, the linear elastic and poro-elastic based models are reviewed in order to analyze these transient effects.

1.2 Problem formulation

Due to the low permeability of shale formations, the time it takes for the stress to redistribute after a new hole is being drilled is very long and hence a failure can occur in the borehole even after a few days of drilling. This is because the pore pressure prior to drilling in a low permeable

formation is very high compared to that of a high permeable formation due to pore pressure not able to dissipate that easily when in contact with the mud (Jianguo Zhang 2006). Also, for the chemically-active shale, the water causes the shale to swell which results in a change in the physical properties of the shale. Experimental studies show changes in strength and young's modulus during such chemical interactions (Jianguo Zhang 2006). Effects on the properties of shale and the critical mud weight density due to temperature is also very important when taking into account the time delayed or transient changes in the properties of the shale formation. In the small analysis above, it can be seen that there are a lot of parameters which are taken into consideration when drilling in the shale formations and these parameters are changing with respect to time and the human controlled attributes such as the mud weight density are to be adjusted accordingly when this happens. Also, since due to so much happening at the same time, coupling all the changes is a troublesome process and an optimal solution is very intricate and most of the times not possible.

The primary step before drilling is designing of well operation programs. The main objective of well program is to drill safely without facing well instability problems such as well collapse and well fracturing. The well pressure should be designed to be within the allowable safe operational window. The physiochemical rock-fluid interaction effect tends to alter the well program.

This thesis addresses these issues with respect to the collapse pressure gradient and analyses the following:

- Single effect of hydraulic diffusion, thermal and chemical effects around the wellbore
- Combined effect of hydraulic diffusion, thermal, and chemical around the wellbore
- Dominant driving forces
- Sensitivity analysis of the model parameters with respect to the driving forces

The overall study may assist design well program with respect to drilling fluid chemistry design. In addition, it will improve understating of time dependent well program conditions.

1.3 Objectives

The main objective of this thesis is to analyze the transient wellbore instability caused by different driving forces. The activities are:

- Review the shale and well instability
- Review the theory of linear elastic and poro-elastic rock mechanic theories along with failure criteria
- Review transient pore pressure changes due to thermo, chemo and hydraulic driving forces
- Perform sensitivity study at the near and far well field stresses with respect to the single and combined transient effects
- Present Heidrun field case study

2 Literature Study on Shale

2.1 Geology

Sedimentary rocks are a type of rocks that are formed by the deposition of the material on the earth's surface or beneath the water bodies. Shale comes under this category of rocks and is formed by the compaction of silt and clay sized mineral particles commonly known as mud (Geoscience). They come under the category of mudstones in the sedimentary rocks classification. Table 1 shows some types of sedimentary rocks with some of their characteristics.

Rock Type	Subdivision	Characteristic
Shale	Soft (ductile)	• Generally occurs in shallower depths (~10,000 ft). • Soft and pliable due to high porosity (15 - 60%) and high water content (25 - 70%). • Fracture pressure approximately same as injection pressure. • Pliable texture allows formation fractures to heal to original strength. • Methylene Blue Test (MBT) 20 - 40 (meq/100 g). • Semectite + illite clays. • Associated with swabbing, lost circulation, hole washout and hole packoff.
	Hard (brittle)	• Generally occurs in deeper depths (>10,000 ft). • Hard and brittle due to low porosity (4 - 15%) and low water content (3 - 10%). • Fracture pressure higher than injection pressure. • MBT 3 - 10 (meq/100 g). • Illite, kaolinite and chlorite clays. • Brittle texture prevents formation fractures from healing. • Associated with hole packoff/bridging.
Sandstone	Unconsolidated	• Generally occurs in the surface hole section (surface to ~5,000 ft). • High porosity (>25%). • High permeability (>2 darcies). • Associated with lost circulation, hole washout and hole packoff.
	Consolidated	• Occurs mostly in middle to deep hole sections (>4,000 ft). • Porosity range (1 - 25%). • Permeability range (10 millidarcies - 2 darcies). • Associated with differential sticking and undergauge hole when abrasive.
Limestone dolomite	Soft (chalk)	• Low compressive strength. • High porosity (~40%). • Permeability range (10 millidarcies - 2 darcies). • Chalk (calcium carbonate) will disperse in freshwater mud. • Associated with hole washout and calcium contamination of mud.
	Hard	• High compressive strength. • Usually fractured by natural forces. • High porosity (20 - 40%). • Permeability range (500 millidarcies - 4 darcies). • Associated with hole packoff/bridging, differential sticking and lost circulation.

Table 1: Relative characteristics of sedimentary rocks (SWACO)

Shales are unique in nature compared to other mudstones due to them having a laminated structure and that they are fissile. This laminated structure is made of thin layers or beds which are less than one centimeter in thickness as illustrated in scanning electron microscope picture in Figure 1 and 2.

Shale consists of clay minerals, which accounts for about 50-60% of shale composition and are therefore the main reason for many problems when drilling through shale formation (Weaver 1965). Clay minerals consist of illite, kaolinite and smectite. Also, the particles which shale consists are mainly quartz, chert and feldspar (Geoscience). Additional to the grains and these minerals, shale structure consists of organic matter, carbonate minerals, iron oxide, sulfide minerals and other heavy mineral constituents which are often present depending on the environment in which the shales are being deposited (Geoscience). These minerals mostly decide the color of the shales which they have. Figure 3 shows some of the different colors and laminar like structure of shales.

The mineral composition of a typical shale is calculated by various authors is shown in Table 2.

	Shaw and Weaver (1965)	Hillier (2006)
Quartz	30.8	23.9
Feldspar	4.5	3.7 (K-spar) 2.4 (Plag.)
Carbonate	3.6	7.5 (Calcite) 1.3 (Dolomite) 0.5 (Siderite
Fe-oxides	0.5	0.8
Clay minerals	60.9	47.7 (Di-clay) 7.5 (Tri-clay)
Other minerals	2	0.5 (Pyrite)
Organic matter	1	Not determined

Table 2: Mineral composition of a typical shale (Weaver 1965)&(S. Hillier 2006)

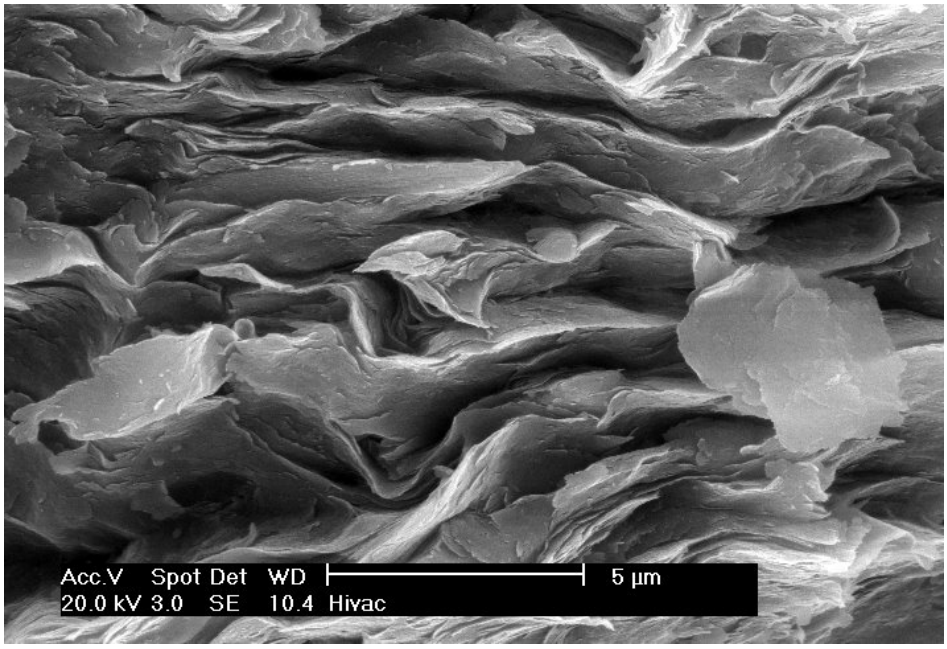

Figure 1: Laminated clay minerals in shale (Institute)

Figure 2: Laminated shale (Institute)

Figure 3: Different types of Shale colors (Geoscience)

Among the different color of shales, black shales are a source of oil and gas. The black color they get is from the organic matter they consist of. This organic matter after a certain amount of time and provided that heat is provide to the rock through natural means changes into oil or gas. Also, shales which usually yield oil and gas are supposed to contain at least 67% of clay minerals (Geoscience). Other shales which do not come into this category can be broken into small pieces to be used as a source of clay that can be used for several purposes such as making objects or the use in cement as a main constituent.

2.2 Oil shale sedimentary deposition

Oil shales are divided into three categories based on their mineral composition. These are the carbonate rich shale, siliceous shale and cannel shale (Lee 1990). Carbonate shales have a large amount of carbonates such as calcite or dolomite. They are generally hard and are resistant to erosion and weathering. Siliceous shales do not have very large amounts of carbonates but they do have other minerals such as quartz, feldspar or clay. They are not that hard as the carbonate shales and are easily weathered or eroded. They are usually black or dark brown in color. Cannel shales have organic matter which encloses the mineral grains completely in them. This type of shale has a lot of impurities and hence is not used for any commercial used. They are also usually dark brown or black in color (Lee 1990).

A.C. Hutton categorized oil shales into three sections according to their depositional environments in 1991 (Dyni 2006). Fluorescent microscopy was used to do so. These three sections of oils shales were subcategorized into further headings. This tree can be seen in Figure 4. Terrestrial oil shales are composed of lipid-rich organic matter such as resin spores, waxy cuticles, and corky tissue of roots and stems of vascular terrestrial pants found in coal forming swamps and bogs. Lacustrine oil shales organic matter is derived from the algae found in the freshwater or saline lakes. Marine oil shales organic matter is derived from the marine algae (Dyni 2006). These categories as seen in the Figure 4 can are further divided into more categories. They are named after the different geological places they were discovered at. For example Torbanite is named after Torbon Hill in Scotland where it was discovered and so on (Dyni 2006).

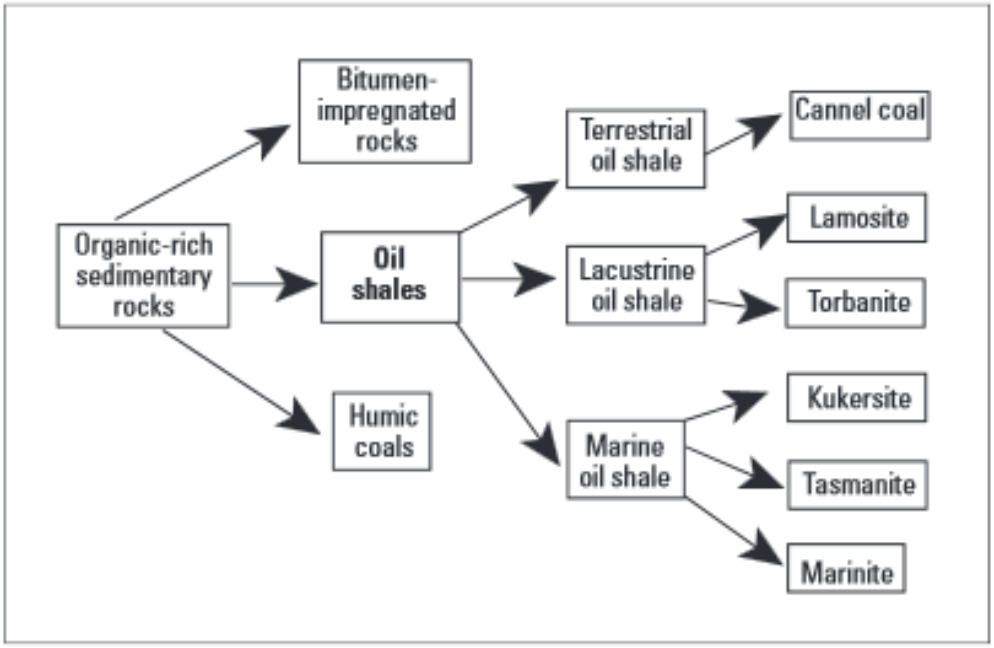

Figure 4:Categories of Oil shale (Dyni 2006)

2.3 Shale Geomechanics

Shale is an anisotropic material and the mechanical properties of it vary in different directions of the load applied to it. Shale as explained above has bedding planes and the properties parallel to and perpendicular to this bedding plane are different. Hence it is very important to understand and know the shale properties in different directions as this can alter the results dramatically while drilling. Also, it will make a key area to look into when deciding the mud weight density and the direction in which the well is being drilled. Table 3 shows some of the anisotropic properties of one of the shale samples tested in the laboratory (Md. Aminul Islam 2013). It can clearly be seen that the maximum Young's modulus of the sample was when then load was at 90 degrees to the normal of the bedding plane that is parallel to the bedding plane. On the other hand, lowest value is observed when this angle is 0 degrees. Note that it is the opposite with the Poisson's ratio. Poisson's ratio is maximum when this angle is zero and minimum when it is at 90 degrees.

Another important factor to look into when looking into shale properties is the confinement pressure due to the presence of pore fluid in the shale. It is observed through an experiment where the Young's modulus of the shale is almost 48% less for the drained sample compared to that of an undrained one (Md. Aminul Islam 2013). Also the Poisson's ratio is 40% lower in value compared to the value of the undrained sample and hence is stiffer than the drained sample (Md. Aminul Islam 2013). Note that these percentages are for a specific sample and the percentages and the values will change depending on the sample but the general big decrease in the values will be seen in the undrained and drained samples. Therefore, getting the values of the mechanical properties at different bedding angles and also getting the undrained and drained values is very essential when drilling into a formation. Table 4 below also shows some of the shales and their unconfined strength with their depositional environments and carbon content percentages with it.

θ (°)	σ_c (MPa)	E_{50} (GPa)	ν_1	ν_2	G_1 (GPa)	G_2 (GPa)	K_1 (GPa)	K_2 (GPa)	λ_1 (GPa)	λ_1 (GPa)
CIU										
0	20	1.360	0.44	0.54	0.47	0.44	3.78	5.67	3.46	5.96
0	25	1.550	0.52	0.53	0.51	0.51	12.92	8.61	13.26	8.95
0	30	1.900	0.41	0.56	0.67	0.61	3.52	5.28	3.07	5.68
45	18	1.150	0.61	0.34	0.36	0.43	1.74	1.20	1.98	0.91
45	25	1.900	0.46	0.35	0.65	0.70	7.92	2.11	7.48	1.64
45	30	2.300	0.58	0.38	0.73	0.83	4.79	3.19	5.28	2.64
60	18	1.450	0.62	0.33	0.45	0.55	2.01	1.42	2.31	1.06
60	25	2.400	0.72	0.38	0.70	0.87	1.82	3.33	2.28	2.75
60	30	2.600	0.56	0.30	0.83	1.00	7.22	2.17	7.78	1.50
90	16	1.730	0.70	0.31	0.51	0.66	1.44	1.52	1.78	1.08
90	20	2.200	0.75	0.32	0.63	0.83	1.47	2.04	1.89	1.48
90	25	2.650	0.65	0.29	0.80	1.03	2.94	2.10	3.48	1.42
CID										
0	17	0.640	0.1	0.1	0.29	0.29	0.27	0.27	0.07	0.07
90	17	1.560	0.19	0.095	0.66	0.71	0.84	0.64	0.40	0.17

θ = angle between loading and normal of the bedding planes, σ_c = confinement pressure, E_{50} = Young's modulus, ν_1 and ν_2 = Poisson's ratios, G_1 and G_2 = shear moduli, K_1 and K_2 = bulk moduli, λ_1 and λ_2 = elastic moduli (Lamé parameters)

Table 3: Mechanical Properties of Shale at different bedding plane angles (Md. Aminul Islam 2013)

Samples	**Age**	**Depositional environment**	**Carbonate content (wt %)**	**Organic carbon content (wt %)**	**Principal clay mineral**	**Unconfined strength (MPa)**
Posidonia (*PS*)	Lower Jurassic	Shallow marine	24	9.7	kaolinite	63
Posidonia (*PN*)	Lower Jurassic		23	12.1	kaolinite	70
Himmetoglu (*H*)	Oligocene	lacustrine	2.2	31.3	Illite	57.7
Torbanite (*T*)	Permian		1.5	51.3	kaolinite	49
Condor (*C*)	Miocene		5	12.6	kaolinite	47
Messel (*M*)	Eocene		7.7	20.3	smectite	5.3

Table 4: Unconfined Strength with respect of depositional environments (E. Eseme 2012)

2.4 Petro-physical properties

Shales have a very low permeability compared to other source rocks due to narrow pore sized in the matrix. This can be seen in Figure 5 which shows the permeability of different rock types (Jefferson 2011). It can easily be se seen in this figure that shale has the lowest permeability among all of them. Also, shales tend to have low porosities too in general. Another interesting factor when looking into the petro-physical properties of shale is the change in the permeability and porosity with the depth. A study was conducted on several wells in North Sea and Figure 6 below shows the results (Okiongbo 2011). It can easily be concluded from Figure 6 that with the increase in the depth, the porosity of the shale formation tends to decrease due to a large overburden stress. In general, if porosity decreases, permeability decreases logarithmically with it (Okiongbo 2011). But another factor which affects the permeability is the pore mean radius and if the radius increases substantially, it will increase the permeability even if the porosity decreases. The density of shales is in the range of 2.65-2.8 g/cm3. Note that the density, pore size and the porosity can be found by different logging tools while drilling into a formation. Once this data is available, permeability can be found through different models or equations which exist. The most general equation which is used to find the permeability is the Darcy's law which states that the rate at which the fluids flow through a permeable material per unit area is equal to the permeability. The equation is as below (Bernt S. Aadnøy 2011):

$$k = \mu \frac{\dot{u}}{\Delta P} \qquad 2.1$$

Where

'k' is the permeability, ΔP is the change in pressure per length, μ is the dynamic viscosity and $\dot{u}$ is the fluid velocity.

Note that the above equation is only valid if the flow is laminar and the fluid is viscous. Also, if the flow is in a different geometry like a circular borehole of a well, a geometry factor is also needed for the equation. In order to overcome this problem and also for bedded planes structure shale, Josef Kozeny and Philip C. Carman derived an equation. The equation known as the Kozeny-Carman equation is as below (E. Eseme 2012):

$$k_{KC} = \frac{c_{KC \cdot \Phi^3}}{S^2 \cdot (1-\Phi)^2} \qquad 2.2$$

where S is the specific surface area (m^2/kg) and Φ is the fractional porosity and k_{KC} is in m^2 . The Kozeny–Carman constant c_{KC} including tortuosity and a generalized factor to account for different pore shapes was taken as 2.064×10^{-13} $m^6 kg^{-2}$.

Note that if the flow is not laminar or if the fluid is not non-Newtonian, the above equations will not be accurate to calculate permeability and other equations and models are used in that case.

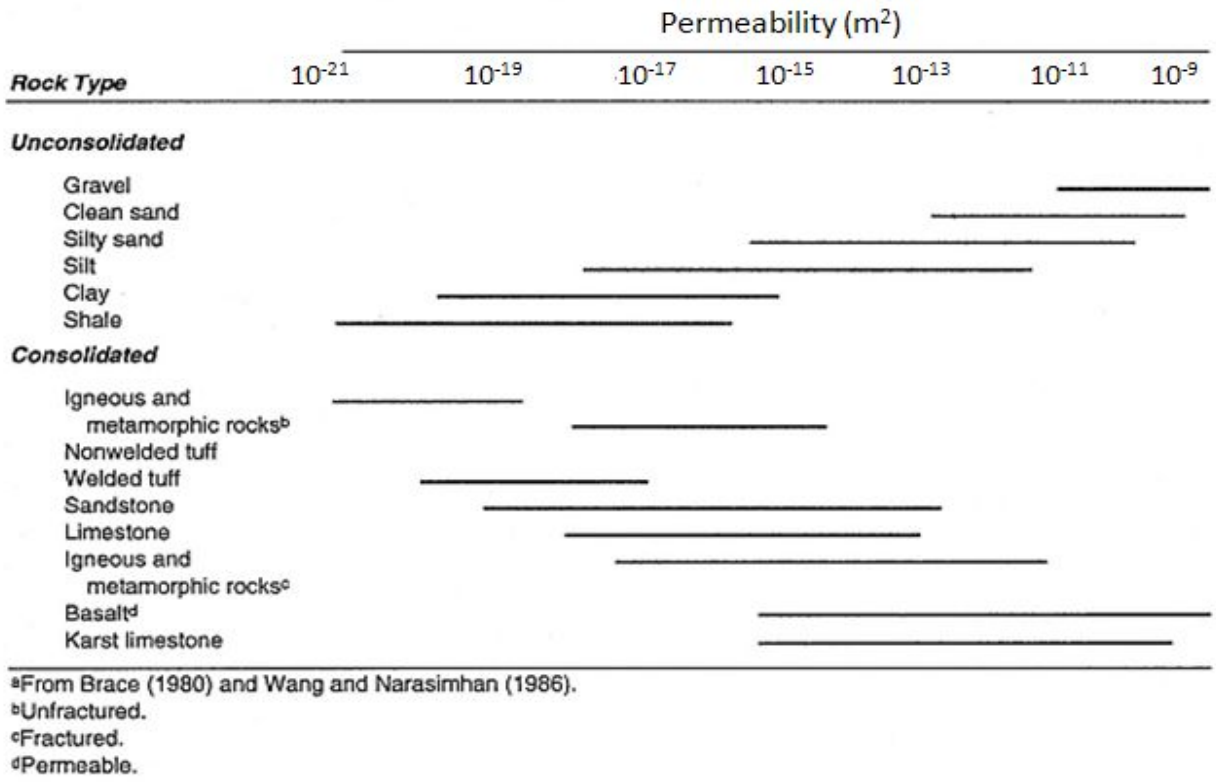

Figure 5:Permeability of different sedimentary rocks (Jefferson 2011)

S.No.	Well no.	Depth (m)	TOC (%)	Grain density (gcm^3)	Porosity	Mean radius (nm)	Permeability (nD)
1	31/2 - 2	1515	4.16	2.69	0.242	13.5	4.800
2	35/11 - 4	1979	4.03	2.69	0.095	14.3	1.400
3	31/4 -10	2007	5.91	2.67	0.110	7.8	0.870
4	31/4 - 9	2117	9.53	2.61	0.205	6.1	1.600
5	31/4 - 6	2132	7.05	2.64	0.192	6.3	1.500
6	34/10 -18	2352	5.61	2.67	0.164	34.5	7.300
7	30/9 - 10	2755	3.69	2.70	0.165	35.6	8.600
8	30/9 - 14	2978	3.06	2.86	0.103	6.3	0.640
9	211/12A - M1	3125	8.21	2.64	0.143	13.0	2.100
10	211/12A - M1	3282	5.81	2.63	0.152	12.7	2.300
11	211/12A - M16	3376	9.77	2.65	0.243	10.9	3.800
12	211/12A - M16	3401	8.18	2.69	0.238	15.7	5.500
13	34/8 - 6	3578	9.43	2.61	0.128	2.3	0.290
14	16/7b - 20	3932	7.53	2.63	0.093	1.2	0.095
15	16/7b - 20	4030	7.42	2.65	0.105	2.2	0.081
16	16/7b - 28	4120	8.34	2.64	0.072	2.9	0.180
17	16/7b - 20	4134	11.10	2.62	0.080	3.8	0.270
18	16/7b - 20	4158	5.85	2.62	0.052	2.5	0.100
19	3/29 - 2	4608	6.91	2.67	0.064	3.2	0.170
20	3/29a - 4	4707	4.46	2.68	0.043	2.0	0.067
21	3/29a - 4	4742	6.37	2.67	0.048	2.5	0.095
22	3/29a - 4	4781	6.16	2.66	0.033	4.3	0.100

Figure 6:Petro-physical properties of shale along the depth (Okiongbo 2011)

2.5 Well instability

The main driving forces for well bore instability are due to mechanical (stress, pressure), thermal and chemical. The failure mechanisms are tensile and collapse (Bernt S. Aadnøy 2011). Shale by its very nature is of brittle and ductile type. The brittle types of shale fail by fracturing and they may cause well pack-off and bridging. The ductile nature of the formation behaves like plasticity and may flow into a well. This may cause drill string sticking. The reactive shale may get swelled when interacting with water based drilling fluid. This as a result reduces the well size and may cause drill string sticking. A high pressure formation in shale formation as illustrated in Figure 7 may cause well collapse. The following are the main causes of instability:

• **Mechanical stress.**

- ✓ Tension failure — fracturing and lost circulation.
- ✓ Compression failure — spalling and collapse or plastic flow.
- ✓ Abrasion and impact.

• **Chemical interactions with the drilling fluid.**

- ✓ Shale hydration, swelling and dispersion.
- ✓ Dissolution of soluble formations.

• **Physical interactions with the drilling fluid.**

- ✓ Erosion

Figure 8 illustrate the well instabilities.

Hole instability is seen most often as sloughing and caving shale, resulting in hole enlargement, bridges and fill. The most common consequences are stuck pipe, sidetracks, logging and interpretation difficulties, and sidewall core recovery difficulties, difficulty running casing, poor cement jobs and lost circulation.

All contribute to increased costs, the possibility of losing part of the hole or the entire well or reduced production.

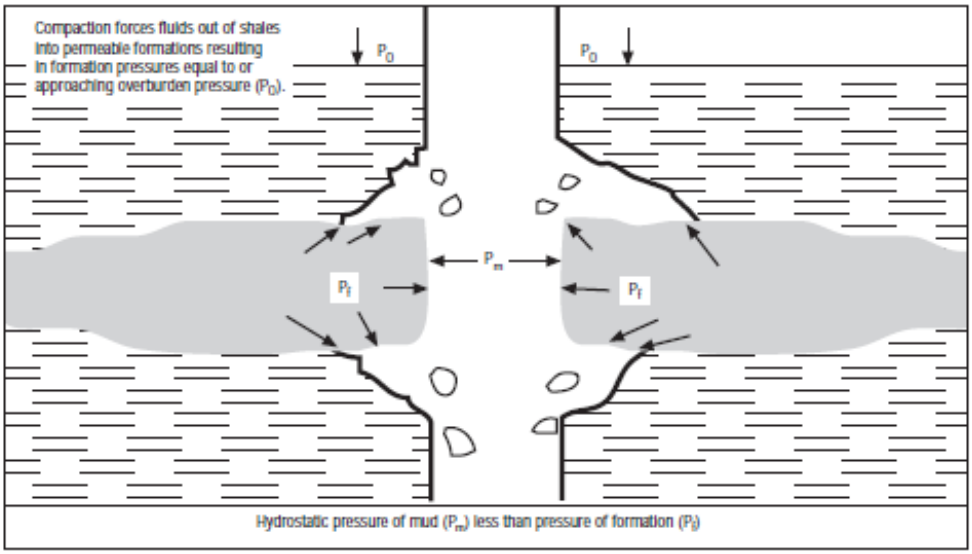

Figure 7: Collapse in pressurized shale formation (SWACO)

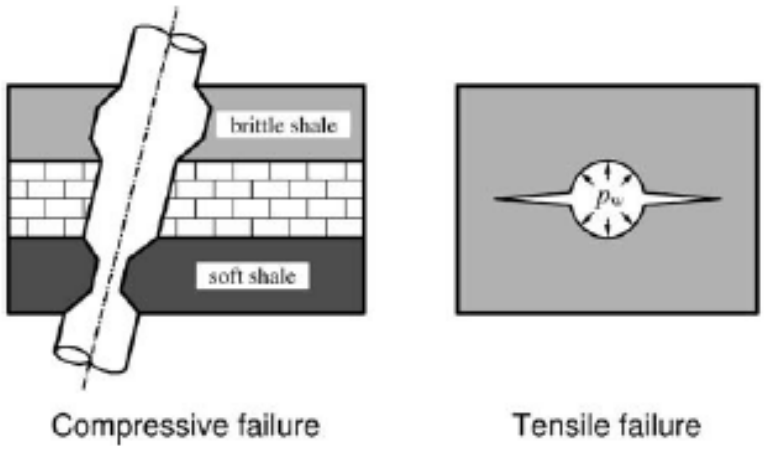

Figure 8: Compressive and tensile failure in shale formation (E. Fjær 2008).

2.6 Additives and Inhibitors for Shale drilling

Shale has a tendency to swell when in contact with water. Because of this, many problems occur while drilling. The most important one is the stuck pipe. In order to solve this problem, oil based muds are used which are not that reactive to shale and therefore don't swell the formation. This was seen in practical when a case study was done on a number of wells in Italy. It was seen that stuck pipe problems incurred in 4 out 26 wells only when oil based muds were used to drill shale section. On the other hand 40 out of 74 wells had a stuck pipe problem due to swelling of shale when water based muds were used (F.J. Santarelli 1995).

It is not always possible to use oil based muds due to environmental and economic concerns as oil base muds are more prone to environment damage and are also very expensive compared to water based muds. Hence in order to use water based muds, additives or inhibitors are used to stop the swelling in shales. Note that the swelling cannot be completely illuminated from the formation as there is always some hydration in the formation due to contact with water (Oort 2003). Note that different salts can be used in water in order to reduce swelling. Each salt will have different effect on the swell reduction depending on the diffusivity of the ions in the salt and the difference in the activity of shale and water base fluid. Also, for different type of shales, different type of salts will have different effects (S.O. Osisanya 1996). In Figure 9 and 10 below, it can easily be seen that for different shales, a different salt is good for swell reduction. Therefore, it is very important to have this type of data when designing a mud for shale formations.

Test Fluid	Linear Swelling After 300 Hours (%)	% Reduction In Swelling Below That Of Water	Rank**
Deionized Water*	0.161	–	
3% KCl solution	0.135	16	8
10% KCl solution	0.106	34	5
4% NaCl solution	0.148	8	9
20% NaCl solution	0.129	20	7
10% Glycerol Mud	0.103	36	4
20% Glycerol Mud	0.077	52	3
30% Glycerol Mud	0.069	57	2
5% KCl/PHPA Mud	0.108	33	6
Mineral Oil*	-0.042	-26 (shrinkage)	1

* Average of two tests

** 1 = Best . . . 9 = Worst

Figure 9: Wellington Shale reduction in swelling with different salts (S.O. Osisanya 1996)

Test Fluid	Linear Swelling After 300 Hours (%)	% Reduction In Swelling Below That Of Water	Rank**
Deionized Water*	0.179	—	
3% KCl solution	0.043	76	1
10% KCl solution	0.061	66	2
4% NaCl solution	0.088	51	5
20% NaCl solution	0.076	58	4
5% KCl/PHPA Mud	0.068	62	3

* Average of two tests

** 1 = Best . . . 5 = Worst

Figure 10: Atoka Shale reduction in swelling with different salts (S.O. Osisanya 1996)

3 Theory of Rock Mechanics

3.1 Stress and Strain

Stress is the force per unit area over any surface. If the force applied is normal to the surface, the stress is called the normal stress and if the force is applied parallel to the surface, stress exerted is called the shear stress. Strain is the ratio of the change in length of any material to that of its original length under any load in the direction of the load.

$$Stress = \frac{Force}{Area} = \frac{F}{A}$$

$$Strain = \frac{Change\ in\ Length}{Initial\ Length} = \frac{\Delta L}{L}$$

$$Young's\ Modulus = \frac{Stress}{Strain} = \frac{FL}{A\Delta L}$$

Any ductile material like steel under a stress will show an elastic behavior. That is the stress will be directly proportional to the strain till the proportionality limit and on the removal of any load applied, the material will return to its original position. This is also known as the Hooke's law. Once the transition from elastic to plastic takes place, the material goes under the maximum load known as the ultimate tensile tress. This is the maximum load which can be applied to a material before its fails. After this point, a material usually becomes weak and fracture. The stress at which the transition from elastic to plastic region takes place is called the yield point and is generally the reference point which is taken when noting the strength of the material because even though ultimate tensile strength is more in magnitude, after this point the material changes its shape and is not in its original position anymore which is not acceptable for most of the applications. Figure 11 below shows such behavior of a ductile material. Note that if the material is brittle such as glass, the material will not show any plastic behavior and will break away right after the elastic behavior shown. Poisson's ratio is the ratio of the change in length in the lateral direction of the force applied to the original length in that direction.

Figure 11 is a typical pore pressure dependent stress-strain behavior of rock material. The curve shows a complete transition from ductile to brittle behaviour as the pore pressure increased.

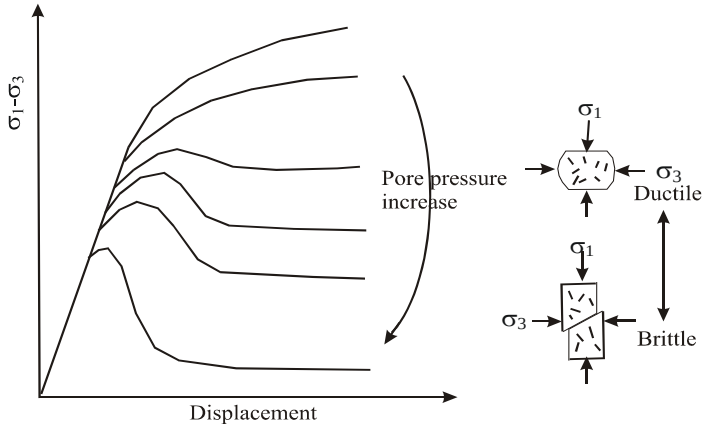

Figure 11: Effect of pore pressure on brittle-ductile transition (Bernt S. Aadnøy 2011)

3.2 Stress Components

In a three dimensional state, the stress on an object can be defined by nine stress vectors. Among these nine stress vectors, three of them are the normal stress vector and six of them are the shear stress vectors. The normal stress vectors are σ_{xx}, σ_{yy} and σ_{zz} and the shear stress vectors are τ_{xy}, τ_{yx}, τ_{xz}, τ_{zx}, τ_{yz} and τ_{zy}. Note that the index letters with each stress vector shows the direction and the face on which the stress vector acts. That is the first letter in the index shows axis normal to the face of the plane and the second letter shows the direction of the stress. Below is a visual illustration of such stress matrix.

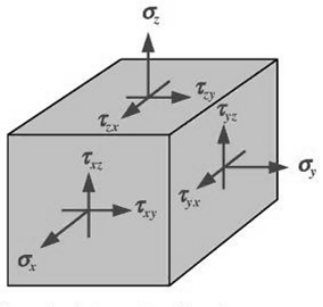

Figure 12: Three-dimensional stress state of a cube (Bernt S. Aadnøy 2011)

When the object is at rest, that is it is not rotating in any direction, the shear stresses in opposite directions become equal as shown below.

$$\tau_{xy} = \tau_{yx}\,, \tau_{xz} = \tau_{zx}\; and\; \tau_{yz} = \tau_{zy}$$

The stress matrix in three dimensional can be shown as below (Bernt S. Aadnøy 2011):

$$[\sigma] = \begin{bmatrix} \sigma_x & \tau_{xy} & \tau_{xz} \\ \tau_{xy} & \sigma_y & \tau_{yz} \\ \tau_{xz} & \tau_{yz} & \sigma_z \end{bmatrix}$$

The above matrix coordinate system can be rotated in a direction such that all the shear stresses disappear. When this happens, only three stress vectors are left in the matrix. These are the three normal stresses also known as the principal stresses. Principal stresses are very important for evaluating rock failure since most shear failure criteria involve two or three principal stresses. The directions of each of them are mutually orthogonal to each other. In an area without a fault and heterogeneities in structure, the overburden is usually one of the principal stresses. The two remaining principal stresses are therefore in the horizontal plane.

3.3 In-situ Stresses

In any formation beneath the earth's crust, the sediments are in equilibrium until disturbed. At this equilibrium state, the stresses which are exerted on the sediment are called the in-situ stresses. They consist of a vertical stress which is due to the overburden of the sediments above, and the two horizontal stresses which are due to the overburden and the tectonics and geological depositions.

3.3.1 Vertical Stress

Vertical stress in the sediments increases with the depth as more overburden will be exerted due to an increase number of sediments. If the formations are homogenous, then the vertical stress is given by$\sigma_v = \rho g z$. If the formations are not homogenous, then the density will not be the same and hence the equation below will be used to determine the overburden stress (E. Fjær 2008).

$$\sigma_v = \int_0^D \rho(z) g dz \qquad 3.1$$

ρ = density of the material, g is the acceleration of gravity, dz = thickness of the formation, σ_v = vertical stress.

3.3.2 Horizontal Stresses

When an overburden stress exists in a formation, it will also push the sediment in the horizontal direction in additional to the vertical squeezing. This will result in horizontal stresses acting on the sediment too. Note that it is assumed that the rock is isotropic. Also, if the tectonic movements are assumed to not exist, then the stresses in the horizontal direction due to them are also excluded. In this case the horizontal in-situ stress is equal to the equation below (E. Fjær 2008):

$$\sigma_h = \frac{v}{1-v}\left(\sigma_v - \alpha_o P_p\right) + \alpha_o P_p \qquad 3.2$$

where σ_h = minimum horizontal stress, σ_v = overburden, P_p = pore pressure, α_o = Biot – coefficient (set as 1.0 for unconsolidated sands, and 0.9 in shale and consolidated sands). Figure 13 illustrates the schematic in-situ stress and the associated fault systems.

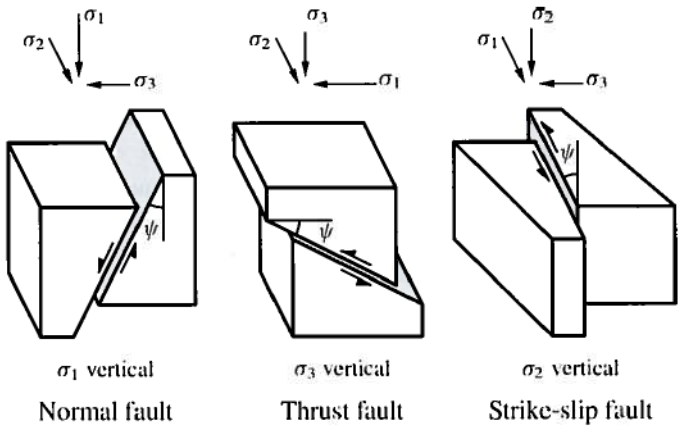

Figure 13: Different types of faults in the formations (E. Fjær 2008)

Normal Fault Stress State: $\sigma_v > \sigma_H > \sigma_h$

Strike/Slip fault stress state: $\sigma_H > \sigma_v > \sigma_h$

Reverse fault stress state: $\sigma_H > \sigma_h > \sigma_v$

In stress relaxed environments, the two horizontal stress tensor components σ_h and σ_H are equal. They will change if tectonic movements are taking place. The stress contribution due to these

movement or the faults as shown above in Figure 13 are not known. Generally the effect of these contributions exits and hence the two horizontal stresses are not equal. If all the in-situ stresses are known, the type of fault which is occurring in the rock can be easily known from the data above.

3.4 Stress around the wellbore

Stresses are exerted on the walls of the well when pressure is applied to it. These stresses make volumetric changes in the well. If the horizontal in-situ stresses are not equal and have different magnitudes and also the overburden stress is different too, in this case an anisotropic condition exists. Kirsch introduced the solution for this condition and generated equations for the stresses around a wellbore in any direction. The equations can be seen below for all directions (Bernt S. Aadnøy 2011). Note that since the in-situ stresses are not equal shear stresses will also exist and the equations for the shear stresses were also found by Kirsch. Figure 14 also shows the direction of these stresses around the wellbore and the coordinate system direction too. (Bernt S. Aadnøy 2011)

$$\sigma_r = \frac{1}{2}(\sigma_x + \sigma_y)\left(1 - \frac{a^2}{r^2}\right) + \frac{1}{2}(\sigma_x - \sigma_y)\left(1 + 3\frac{a^4}{r^4} - 4\frac{a^2}{r^2}\right)cos2\theta + \tau_{xy}\left(1 + 3\frac{a^4}{r^4} - 4\frac{a^2}{r^2}\right)\sin 2\theta + \frac{a^2}{r^2}P_w$$

$$\sigma_\theta = \frac{1}{2}(\sigma_x + \sigma_y)\left(1 + \frac{a^2}{r^2}\right) - \frac{1}{2}(\sigma_x - \sigma_y)\left(1 + 3\frac{a^4}{r^4}\right)\cos 2\theta - \tau_{xy}\left(1 + 3\frac{a^4}{r^4}\right)\sin 2\theta - \frac{a^2}{r^2}P_w \qquad 3.3$$

$$\sigma_z = \sigma_{zz} - 2v(\sigma_x - \sigma_y)\frac{a^2}{r^2}cos2\theta - 4v\tau_{xy}\frac{a^2}{r^2}sin2\theta \rightarrow Plane\ strain$$

$$\sigma_z = \sigma_{zz} \rightarrow Plane\ stress$$

$$\tau_{r\theta} = \left[\frac{1}{2}(\sigma_x - \sigma_y)sin2\theta + \tau_{xy}cos2\theta\right]\left(1 - 3\frac{a^4}{r^4} + 2\frac{a^2}{r^2}\right)$$

$$\tau_{rz} = (\tau_{xy}\cos\theta + \tau_{yz}sin\theta)\left(1 - \frac{a^2}{r^2}\right)$$

$$\tau_{\theta z} = (-\tau_{xz}sin\theta + \tau_{yz}cos\theta)\left(1 + \frac{a^2}{r^2}\right)$$

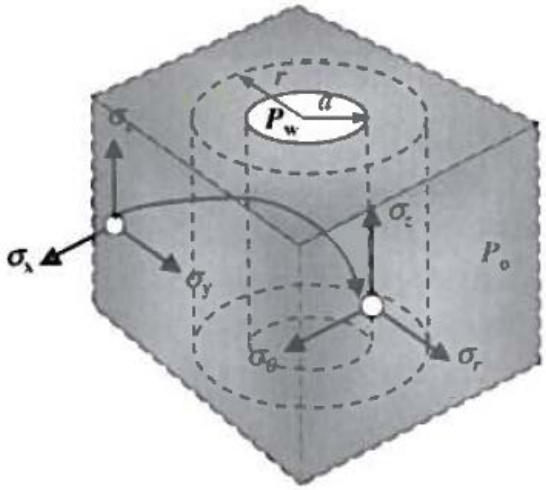

Figure 14: Position of stresses around a wellbore in the rock formation (Bernt S. Aadnøy 2011)

3.5 Stress Transformation

The in-situ stresses (σ_h, σ_H, σ_v) equations are in the x, y and z directions in a plane. If the well is oriented and has an azimuth (φ) or inclination (γ) or both, the in-situ stresses can be transformed into the new coordinate system with the help of the transformation equations below (B.S. Aadnøy 1987):

$$\sigma_{xx} = (\sigma_h \cos^2\varphi + \sigma_H \sin^2\varphi)\cos^2\gamma + \sigma_v \sin^2\gamma$$

$$\sigma_{yy} = \sigma_h \sin^2\varphi + \sigma_H \cos^2\varphi$$

$$\sigma_{zz} = (\sigma_h \cos^2\varphi + \sigma_H \sin^2\varphi)\sin^2\gamma + \sigma_v \cos^2\gamma$$

$$\tau_{xy} = \frac{1}{2}(\sigma_H - \sigma_h)\sin 2\varphi \cos\gamma \qquad 3.4$$

$$\tau_{yz} = \frac{1}{2}(\sigma_H - \sigma_h)\sin 2\varphi \sin\gamma$$

$$\tau_{xz} = \frac{1}{2}(\sigma_h \cos^2\varphi + \sigma_H \sin^2\varphi - \sigma_v)\sin 2\gamma$$

3.6 Principal Stresses around a wellbore

If the normal and shear stresses are known for a well at the wall of the borehole, the principal stresses can easily be calculated by the equations below. The stress tensor at the wall of the wellbore where r = a is given as:

$$[\sigma] = \begin{bmatrix} \sigma_r & 0 & 0 \\ 0 & \sigma_\theta & \tau_{\theta z} \\ 0 & \tau_{z\theta} & \sigma_{zz} \end{bmatrix}$$

The equations below show the principal stresses are simply given as (Bernt S. Aadnøy 2011):

$$\sigma_1 = P_w$$

$$\sigma_2 = \frac{1}{2}(\sigma_\theta + \sigma_{zz}) + \frac{1}{2}\sqrt{(\sigma_\theta - \sigma_{zz})^2 + 4\tau_{\theta z}^2} \qquad 3.5$$

$$\sigma_3 = \frac{1}{2}(\sigma_\theta + \sigma_{zz}) - \frac{1}{2}\sqrt{(\sigma_\theta - \sigma_{zz})^2 + 4\tau_{\theta z}^2}$$

3.7 Failure modes

There are many failure modes which can let a rock fail. It is very important to understand the mechanism through which the rock fails in order to be prepared for such a failure and take precautions to prevent it and to keep the risk of the failure to occur as low as possible. The two main types of these modes are the tensile and collapse failure.

3.7.1 Tensile failure

Tensile failure occurs when the rock effective minimum principal stress reaches its tensile strength. When this happens, the rock tends to break and fail. Many rocks have a lot of cracks in them naturally which tend to make the rocks very weak and the tensile strength for such rocks are set to zero due to this reason. The failure criterion according to Rankine is given as (Fjær, Holt et al. 2008):

$$\sigma_3' = -\sigma_T \qquad 3.6$$

3.7.2 Shear or collapse failure

When a rock undergoes a high compressive load, shear failure normally takes place. This failure takes place due to shear stress along the plane exceeding its shear strength and letting a fault to create along the plane. This will separate the two planes and slide them against each other. Note that the shape of the borehole during compressive loading will depend on the loads. That is if the stresses around the wellbore are uniform and equal, the shape will be like a circle but no changes will be seen on the shape during deformation as seen in Figure 15. On the other hand, if the compressive loading is polyaxial, then the shape will also change into an eclipse like shape. These changes in the wellbore geometry can be observed with the help of the caliper logs. Collapse failure will occur in both situations. In order to analyze the collapse and other failure modes, analytical or numerical modeling is used. Two models that are widely used in the petroleum industry for the collapse failure are Mohr-coulomb criteria and Mogi-coulomb criteria.

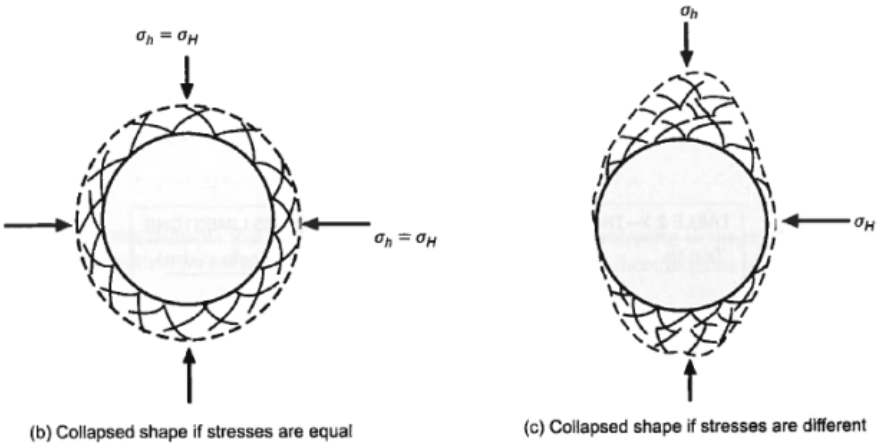

Figure 15: Collapse of borehole wall (Mitchell, Miska et al. 2011).

3.7.3 Creep failure

Creep is the tendency of the material to deform permanently under constant high stress loads for a long period of time. Its severeness changes with the increase in magnitude of this high stress. Note that the stress here is below the yield point. This deformation phenomenon increases even more if the temperature is increased. Hence creep failure will be more severe under high temperature which is a problem in many high temperature wells. There are three stages of creep. The first stage is called the transient creep. During this stage, small fractures occur and deformation takes place. Then if the stress is reduced to zero, the cracks tend to disappear and

the deformation completely vanishes. Second state of creep is called the steady state creep. During this stage, the same things happens as in transient creep but on removing the load, the deformation does not vanishes completely and there remains a small permanent deformation. The third state is the final stage known as the accelerating creep. During this stage, the deformation will exceed rapidly on the exertion of stress and will tend to fracture and hence fail the material instantly.

3.7.4 Pore collapse or compaction failure

This type of failure is mostly seen in the high porosity formations. It happens when the formation is compressed and the grains in the formations tend to lose or break and fall inside the porous holes. This results in filing up the void space making the formation more compact and hence less resistant to failure. Note that this type of failure gets even more importance, when the grain size is much smaller than the pore spaces in the formations. It occurs mainly because of the excessive shear forces acting through the grain and grain contacts in the formation.

4 Collapse modeling

As explained above, whenever a material goes a shear failure, collapse occurs. In order to predict the collapse pressure there exist several collapse failure criteria available in literature. One can then determine a minimum mud weight to help ensure no well collapse during drilling. The collapse pressure increases and the fracture pressure decreases as the well inclination increases.

4.1 Input parameters for well collapse wellbore modeling

4.1.1 In-situ horizontal stress

Using several fracturing data, Breckels and van Eekelen (I.M. Breckels 1982) have developed an empirical correlation equation which relates horizontal in-situ stress with depth. For the US Gulf coast, the authors have presented equation 4.1a and 4.1b.

$$\sigma_h(MPa) = 0.0053(D)^{1.145} + 0.46(P_o - p_{fn}) \qquad \text{For Depth 'D' < 3500m} \qquad 4.1$$

$$\sigma_h(MPa) = 0.0264D(m) - 31.7 + 0.46(P_o - p_{fn}) \qquad \text{For D > 3500m} \qquad 4.2$$

where p_{fn} = normal pore pressure

$p_{fn} = \rho_{fl} gD(\text{water.depth})$

4.1.2 Pore Pressure

Oil companies have lost millions of dollar because of not having the accurate information on the pore pressure. This is due to the loss of the drilling time due to stopping the operations caused by stuck pipe, kicks and other during drilling problems. A commonly used approximation to find the pore pressure was given by Eaton's empirical method and is as below (Eaton 1972):

$$P_o = P_{obs} - (P_{obs} - P_{hyd})\left(\frac{V_i}{V_n}\right)^3 \qquad 4.3$$

P_o = Predicted (shale) pore pressure

Pobs = Overburden pressure (rocks and fluids)

P_{hyd} = Hydrostatic pressure (fluids)

V_i = Interval velocity (seismic data)

V_n = normally compacted shale velocity

Note that the Pp, Phyd and V_n are calculated by the empirical values data collected for each well. 'V_i' is calculated from the seismic data which is collected during well logging. The pore pressure can be calculated from seismic data collected from well logging or calculated while drilling and the mud weight can be adjusted while drilling depending on the pore pressure calculated. Also, instead of putting in the values for velocity, time interval values can also be put in the above equation to find the pore pressure. In this case, the above will equation will be expressed as (Eaton 1975)

$$P_o = P_{obs} - (P_{obs} - P_{hyd})\left(\frac{dt_{actual}}{dt_{normal}}\right)^3 \qquad 4.4$$

4.1.3 Unconfined or uniaxial compressive strength (UCS)

It is the strength of the rock when the rock is compressed in the uniaxial direction without any lateral restraint. A graphical illustration of such a failure can be seen in Figure 16 showing the three main regions which are the elastic, ductile and brittle behavior region during the uniaxial loading. This strength can be explained by the equation below. Note that UCS is a very vital property which should be known as it is used in various failure criteria models (Fjær, Holt et al. 2008).

$$UCS = C_0 = 2S_0 \tan\beta \qquad 4.5$$

$'\beta'$ is the orientation of the failure plane $'S_0'$ is the cohesion strength and is the ability of adhesive molecules to stick together without getting separated under any tensile loading and resist any plastic deformation. Note that there is a force which is attracting the two adjacent molecules in the rock. These forces between the atoms are the cohesive forces.

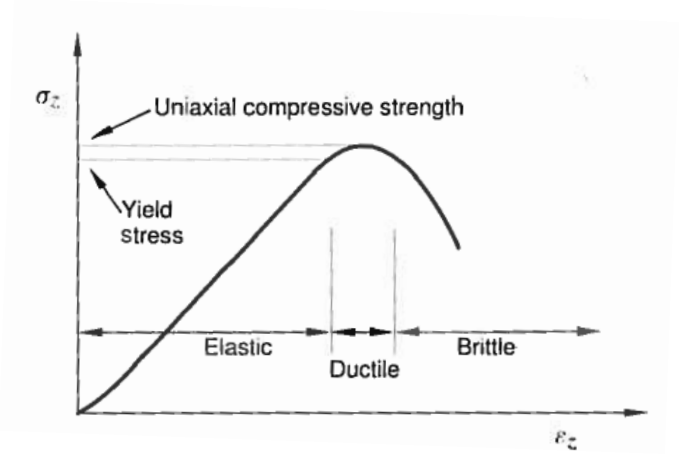

Figure 16: Principle sketch of stress vs. deformation in a uniaxial compression test (Fjær, Holt et al. 2008).

Cohesive shear stress also known as the uniaxial compressive strength can be calculated by two models derived by Horsud (2001) and Lal et al (1999). They used sonic logs to find the above strength. The models were as below (Horsrud 2001):

$$\text{Per Horsrud (2001):} \quad C_o[\text{MPa}] = 0.77\left(\frac{304.8}{\Delta t(\text{sonic})}\right)^{2.93} \qquad 4.6$$

$$\text{Lal (1999)} \quad : \quad C_o[\text{MPa}] = 10\left(\frac{304.8}{\Delta t(\text{sonic})} - 1\right)$$

The cohesive strength also changes with respect to the time. It is as below (Lal 1999):

$$C = (C_o - C_e)\exp(at) + C_e \qquad 4.7$$

Where 't' is time in days, 'a' is a consonant and C_e is the equivalent cohesive strength. After a number of days, the cohesive strength of any formation is reduced to this equivalent cohesive strength. A graph below shows cohesive strength changing with time.

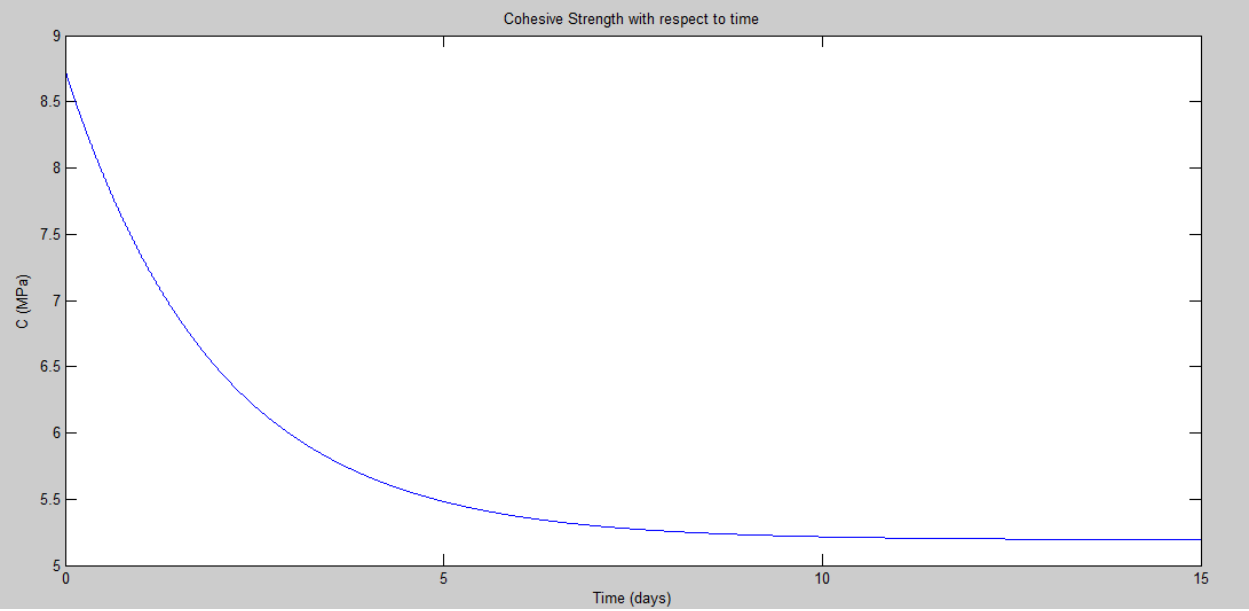

Figure 17: Cohesive Strength as a function of time (Properties taken from Table 6 to plot the graph on Matlab)

4.1.4 Poisson's ratio

Poisson's ratio can be calculated from the in-situ stress equation by making the Poisson's ration 'v' is the equation 3.2 as the subject. The equation will be as below:

$$\upsilon = \frac{\overline{\sigma_h}}{\overline{\sigma_v} + \overline{\sigma_h}} \qquad 4.8$$

where $\overline{\sigma_{h,v}} = \sigma_{h,v} - P_o$

4.1.5 Internal friction angle and inherent shear strength

Internal friction angle is the angle at which the surface of the rock is at an angle where sliding takes place without any external load applied on it and the cohesive strength is the shear stress of the rock without any normal stress applied to it. Cohesive strength 'S_0' of a rock can be determined in the laboratory by applying a rock to a hydrostatic confining pressure and then to an axial load until the rock fails. But it is not practically possible to do so along the whole depth of a well as it will take a lot of time. Therefore empirical models are used which uses the information from the wireline logs to calculate the cohesive strength and the internal friction angle. They were derived by Lal (1999). The models can be seen below in Equations 4.9 and

4.10 (Lal 1999). 'V_p' below is the sonic wave velocity in km/s and cohesive strength is measured in MPa.

$$\sin\phi = \frac{V_p - 1}{V_p + 1} \qquad 4.9$$

$$S_o = \frac{5(V_p - 1)}{\sqrt{V_p}} \qquad 4.10$$

4.1.6 Young's Modulus (E)

Young's Modulus can also be measured through the help of the sonic wave velocity. This young's modulus will take into account the temperature and other changes which might have changed it down the well. The model to do so was derived by Horsrud in 2001 and is as below (Horsrud 2001):

$$E = 0.076 V_p^{3.23} \qquad 4.11$$

where E is in GPa and Vp is in km/s.

4.2 Collapse Failure models

There are several models to analyze the collapse failure mode and to calculate the minimum mud weight to ensure wellbore stability. Two of the most commonly used criteria for this mode of failure are the Mohr-Coulomb criteria and Mogi-Coulomb criteria and both will be explained it more detail in this section.

4.2.1 Mohr-Coulomb criteria

It is the most common and simplest type of failure criteria for geomaterials due to its simplicity. For a well borehole, the linear elastic model can be described as below (Lianyang Zhang 2010):

$$\tau = S_o + \sigma_n' tan\emptyset \qquad 4.12$$

The above equation can also be written in terms of the two principal stresses which are the maximum and minimum principal stresses. Also, if the pore pressure effect is considered, the new poro-elastic model for Mohr-Coulomb failure criteria is given as in equation 4.13 (E. Fjær 2008).

$$\sigma_1 - \alpha_o P_o = C_o + (\sigma_3 - \alpha_o P_o)\tan\alpha \qquad 4.13$$

Where α_o is to denote the Biot's coefficient and P_o is the pore pressure and C_o is uniaxial compression strength. The uniaxial compressive strength can be determined from inherent shear strength and the internal friction angle ϕ as (Lianyang Zhang 2010):

$$C_o = \frac{2S_o\cos\phi}{1-\sin\phi} \quad \text{or Horsrud's empirical model (Eq4.6)} \qquad 4.14$$

Note that 4.14 is just another way of expressing equation 4.5 for the same property and either can be used. Some relations are given below in equation 4.15 for different angles that can be used in the model above (E. Fjær 2008).

$$\tan^2\beta = \frac{1+\sin\phi}{1-\sin\phi}$$
$$\beta = 45^o + \frac{\emptyset}{2} \qquad 4.15$$
$$tan^2\beta = tan\alpha$$

- S_o is the inherent shear strength (cohesion) and calculated by Eq 4.10.
- ϕ is the friction angle and calculated by Eq 4.9.

It can be seen from the above equation 4.13 for this criterion that it does not take into account the intermediate principal stress. This results in an underestimation of the rock strength which ends up in a very conservative collapse pressure curve (A.M. Al-Ajmi 2006). It is also known from

different studies that another failure criterion known as Drucker- Prager does very well with a material under triaxial loading where $\sigma_1 \neq \sigma_2 = \sigma_3$ but when the criterion is applied for polyaxial loading where $\sigma_1 \neq \sigma_2 \neq \sigma_3$, the test is not that accurate and the results are not a true representation of the critical mud weights (Lianyang Zhang 2010).

In order to get the well collapse and fracture equations from this model for well borehole, some assumptions are made. Firstly, it is assumed that the shear stress in the Kirsch's equations is zero as it is usually very small and can be neglected compared to other normal stresses. From the Equations 3.3 above, the normal and shear stresses are calculated at the wall of the borehole where 'a' will be equal to 'r' in the equation and the angle θ is equal to $\pi/2$ to get maximum values for the stresses. When these values are inserted in Equation 3.3, the stress components will be reduced to:

$$\begin{aligned}
\sigma'_r &= P_w - P_o \\
\sigma'_\theta &= 3\sigma_x - \sigma_y - P_w - P_o \\
\sigma'_z &= \sigma_z + 2\upsilon\left(\sigma_x - \sigma_y\right) - P_o \\
\tau_{r\theta} &= \tau_{rz} = 0 \\
\tau_{\theta z} &= -2\tau_{xz}
\end{aligned} \qquad 4.16$$

Now since all the stresses are known in terms of in-situ stresses, the principal stresses can be calculated by inserting these stress equations in the equations 3.4 for principal stresses as shown above.

Assuming a vertical well, isotropic stresses and negligible shear stresses, the principal stresses can be given as (E. Fjær 2008):

$$\begin{aligned}
\sigma_r &= P_w \\
\sigma_\theta &= 2\sigma_h - P_w \\
\sigma_z &= \sigma_v
\end{aligned} \qquad 4.17$$

From the above equations, it can easily be concluded that if the pressure of the well will change, it will have an effect on the radial and hoop stresses and the axial stress will have no effect at all when the well pressure changes. Also, in order for a collapse to happen, hoop stress has to be greater than the radial stress. That means there will only be three situations when this can happen. They are when $\sigma_\theta > \sigma_r > \sigma_z$, $\sigma_z > \sigma_\theta > \sigma_r$ and $\sigma_\theta > \sigma_z > \sigma_r$ (A.M. Al-Ajmi 2006). Therefore taking these three situations and putting the values of maximum and minimum principal stresses in the above model, the equations below were derived for well collapse pressure. Also, for the fracture to happen, the radial stress has to be greater than the hoop stress. This will again result in only three possible outcomes. A table was formed for all the six equations.

Cases	**Borehole failure model**	
$\sigma_\theta \geq \sigma_z > \sigma_r$	$P_w \leq P_o + \frac{2(\sigma_h - P_o) - C_o}{1 + \tan^2 \beta}$	4.18
$\sigma_z \geq \sigma_\theta > \sigma_r$	$P_w \leq P_o + \frac{\sigma_v - P_o - C_o}{\tan^2 \beta}$	4.19
$\sigma_z \geq \sigma_r > \sigma_\theta$	$P_w \geq P_o + 2(\sigma_h - P_o) - \frac{\sigma_v - P_o - C_o}{\tan^2 \beta}$	4.20
$\sigma_r \geq \sigma_z > \sigma_\theta$	$P_w \geq P_o + \frac{2(\sigma_h - P_o)\tan^2 \beta + C_o}{\tan^2 \beta}$	4.21
$\sigma_r \geq \sigma_\theta > \sigma_z$	$P_w \geq P_o + (\sigma_v - P_o)\tan^2 \beta + C_o$	4.22
$\sigma_\theta \geq \sigma_r > \sigma_z$	$P_w \leq P_o + 2(\sigma_h - P_o) - (\sigma_v - P_o)\tan^2 \beta - C_o$	4.23

Table 5: Borehole failure criteria for Mohr-Coulomb (E. Fjær 2008)

4.2.2 Mogi-Coulomb criteria

Mogi-Coulomb is said to most accurate model for the failure criteria for sedimentary rocks like shales. It takes into account all the principal stresses, cohesions strength and the angle of friction. From the studies and experiment conducted on this criterion, it was shown that the intermediate principal stress has indeed a strengthening effect on the strength of the rock (A.M. Al-Ajmi 2006). It is also observed that this failure criteria is very accurate for polyaxial loadings too which is realistically a more common situations for the in-situ stresses. This criterion takes into account the octahedral shear stress and the effective mean stress. It is expressed as below (A.M. Al-Ajmi 2006):

$$\tau_{oct} = a + b\sigma'_{m,2} \tag{4.24}$$

The above values in the equation can be found by the equations below (A.M. Al-Ajmi 2006):

$$\begin{gathered} Effective\ Mean\ Stress = \sigma'_{m,2} = \frac{\sigma'_1 + \sigma'_3}{2} \\ Octahederal\ Stress = \tau_{oct} \\ = \frac{1}{3}\sqrt{(\sigma'_1 - \sigma'_2)^2 + (\sigma'_2 - \sigma'_3)^2 + (\sigma'_3 - \sigma'_1)^2} \\ a = \frac{2\sqrt{2}}{3} c \cos \emptyset \\ b = \frac{2\sqrt{2}}{3} \sin \emptyset \end{gathered} \tag{4.25}$$

From the above equations and the equations for the principal stresses, the two tables below are generated the same way as for Mohr-coulomb criteria. The tables for collapse and fracture are as below:

Cases	**Borehole failure model (Collapse)** **Failure will occur if Pw ≤ Pwb from the following equation**	
$\sigma_z > \sigma_\theta > \sigma_r$	$P_{wb} = \frac{1}{6-2b'^2}\left[(3A+2b'K) - \sqrt{H+12.(K^2+b'AK)}\right]$	4.26
$\sigma_\theta > \sigma_z > \sigma_r$	$P_{wb} = \frac{1}{2}A - \frac{1}{6}\left[\sqrt{12\left[(a'+b'(A-2P_o)\right]^2 - 3.(A-2B)^2}\right]$	4.27
$\sigma_\theta > \sigma_r > \sigma_z$	$P_{wb} = \frac{1}{6-2b'^2}\left[(3A-2b'G) - \sqrt{H+12.(G^2-b'AG)}\right]$	4.28
Where $A = 3\sigma_x - \sigma_y$, $B = \sigma_z + 2\upsilon(\sigma_x - \sigma_y)$, $H = A^2(4b'^2-3) + (B^2-AB)(4b'^2-12)$ $K = a' + b'(B-2P_o)$, $G = K + b'A$		

Table 6: Mogi-Coulomb equations for collapse failure (A.M. Al-Ajmi 2006)

Cases	**Borehole failure model (Fracture)** **Failure will occur if Pw ≥ Pwb from the following equation**	
$\sigma_r > \sigma_\theta > \sigma_z$	$P_{wb} = \frac{1}{6-2b'^2}\left[(3D+2b'N) + \sqrt{J+12.(N^2+b'DN)}\right]$	4.29
$\sigma_r > \sigma_z > \sigma_\theta$	$P_{wb} = \frac{1}{2}D + \frac{1}{6}\left[\sqrt{12\left[(a'+b'(D-2P_o)\right]^2 - 3.(D-2E)^2}\right]$	4.30
$\sigma_z > \sigma_r > \sigma_\theta$	$P_{wb} = \frac{1}{6-2b'^2}\left[(3D-2b'M) + \sqrt{J+12.(M^2-b'DM)}\right]$	4.31

Where, $D = 3\sigma_x - \sigma_y$, $B = \sigma_z + 2\upsilon(\sigma_x - \sigma_y)$, $J = D^2(4b'^2 - 3) + (E^2 - DE)(4b'^2 - 12)$ $N = a' + b'(E - 2P_o)$, $M = N + b'D$

Table 7: Mogi-Coulomb equations for fracture failure (A.M. Al-Ajmi 2006)

4.2.3 Drucker-Prager Criteria

Another failure criteria used widely is the Drucker-Prager Criteria. It is said to be an extended version of the Von Mises criteria. It is as below (Mengjiao Yu 2003):

$$\sqrt{J_2} = AJ_1^{ef} + B \tag{4.32}$$

$$\begin{aligned} Effective\ Collpase\ Stress = Failure\ Index = FI = \sigma_{cl} \\ = -\sqrt{J_2} + AJ_1^{ef} + B \end{aligned} \tag{4.33}$$

where

$$\begin{aligned} J_1^{ef} &= \frac{\sigma_{rr} + \sigma_{\theta\theta} + \sigma_{zz}}{3} - p(r,t) \\ J_2 &= \frac{1}{6}((\sigma_{rr} - \sigma_{\theta\theta})^2 + (\sigma_{rr} - \sigma_{zz})^2 + (\sigma_{zz} - \sigma_{\theta\theta})^2) + \sigma_{rz}^2 + \sigma_{r\theta}^2 \\ &\quad + \sigma_{\theta z}^2 \\ B &= \frac{2\sqrt{2}c\cos\emptyset}{3 - \sin\emptyset} \\ A &= \frac{2\sqrt{2}\sin\emptyset}{3 - \sin\emptyset} \end{aligned} \tag{4.34}$$

Failure occurs when the effective collapse stress or the failure index becomes negative (Mengjiao Yu 2003).

4.2.4 Weakness of plane model

Failure model for laminated rocks

Figure 18 shows laminated shale with an angle β, where the weak plane is along this. The shear collapse failure criteria for laminated layer are different from the non-laminated shales. Figure 19 is the loading on the given laminated rock specimen which consists of plane of weakness inclined at an angle β from the vertical plane and η is the anisotropic of a rock. The problem of sliding along a preexisting plane of weakness is illustrated as Figure 18 and 19 (Gatlin 1965).

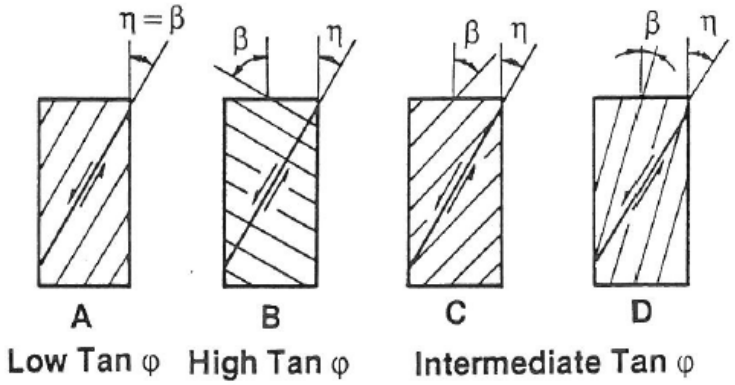

Figure 18: Failure mode for laminated rocks

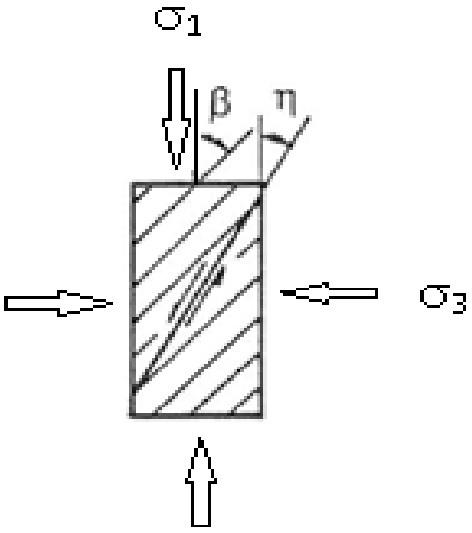

Figure 19: Loading on laminated rocks

If Sw is the inherent shear strength of the plane of weakness and μ_w is the coefficient of internal friction along those planes, then the condition of sliding along these planes can be written as (J.C. Jaeger 2007):

$$\sigma_1 = \sigma_3 + \frac{2(S_w + \mu_w \sigma_3)}{(1 - \cot \beta . \mu_w)\sin 2\beta} \qquad 4.35$$

Where σ_1 and σ_3 are the maximum and minimum principal stresses.

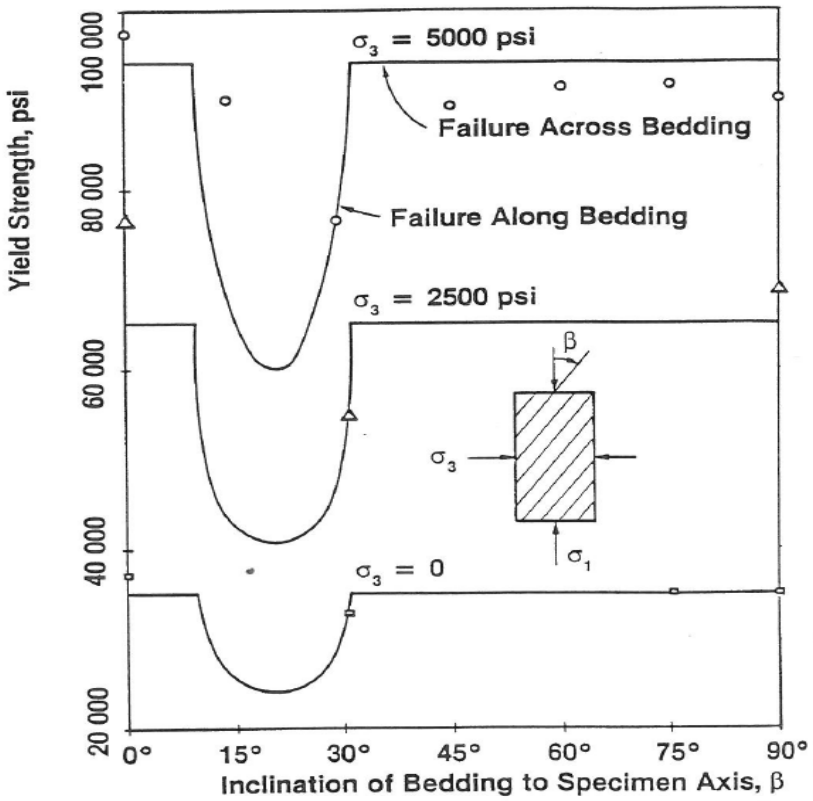

Figure 20: Comparisons of Arkansas Sandstone Data to Single Plane of Weakness Theory (Gatlin 1965)

5 Chemical and thermal effects on Collapse Model

Chemical and thermal effects are of immense importance when dealing with shale formations and they tend to change the collapse and tensile strength significantly when the effects take place. In the early experiments performed by Mody & Hale (C. Chen 2001), it was seen that the initial pore pressure was altered due to these effects. The chemical effects were caused due to osmosis which affects the pore pressure. Osmosis here is the net movement of the solvent into the area of high solute concentration region through a partially permeable membrane. The direction in which the solvent moves is the direction of high solute concentration region such that it tends to equalize the solute concentration between two regions separated by the membrane (CFCF 2013). Figure 21 below shows a visual illustration of such a process where the container on left shows the unbalance position and the container on the right shows the concentration of the solute to be equal on both sides.

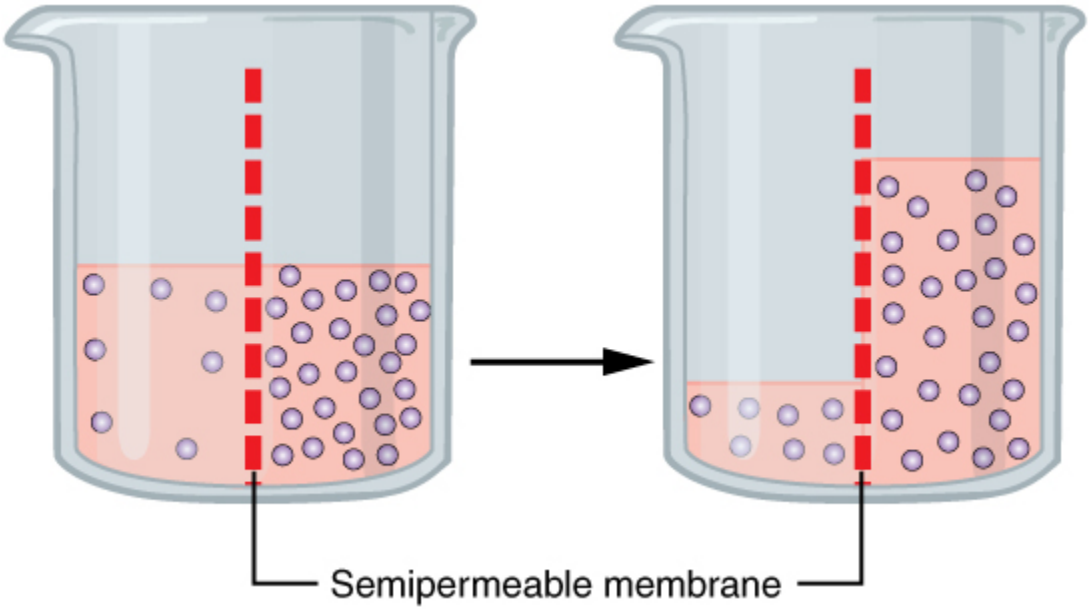

Figure 21: Osmosis process over a semi-permeable membrane (CFCF 2013)

Osmosis effects are function of two main attributes which are the membrane efficiency and the activity of water and formation. Chemical effect due to the difference between the shale water activity and the drilling mud water activity is to be treated as equivalent to the hydraulic potential in the system (C. Chen 2001). Also the membrane efficiency is calculated by taking the ratio of

the observed osmotic pressure to that of the theoretical osmotic pressure. Osmotic pressure here is the force per unit area required to prevent the water to pass through the semi permeable membrane into the area of high solute concentration (CFCF 2013). Note that due to the effect on the pore pressure, these chemical effects therefore have an influence on the wellbore stresses too due to wellbore stresses dependent on the pore pressure.

Thermal stresses can also be induced in the wellbore due to thermal changes in the well. These temperature changes can be due to the injection or production of well where fluids with different temperatures in the annulus tend to change the all temperature at the wellbore. The pore pressure can also change because of the volumetric expansion in the rock matric and the pore fluid and is transient in nature for a low permeable such as shale (Ewy 2005). The thermal and chemical effects can be coupled into thermoporoelastic equations for a radial system such as a wellbore. The details of these equations can be seen below in the report.

There are two main equations which have been introduced which take into account the chemical and temperature effects for a radial system for permeable and non-permeable formations. They are as below (C. Chen 2001):

$$\frac{\partial T}{\partial t} = c_o\left(\frac{\partial^2 T}{\partial r^2} + \frac{1}{r}\frac{\partial T}{\partial r}\right) + c_o'\left(\frac{\partial T}{\partial r}\frac{\partial P}{\partial r} + T\left(\frac{\partial^2 P}{\partial r^2} + \frac{1}{r}\frac{\partial P}{\partial r}\right)\right) \qquad 5.1$$

$$\frac{\partial P}{\partial t} = c\left(\frac{\partial^2 P}{\partial r^2} + \frac{1}{r}\frac{\partial P}{\partial r}\right) + c'\frac{\partial T}{\partial t} \qquad 5.2$$

Where c= hydraulic fluid diffusivity; c_o= thermal diffusivity of the porous medium; c_o'= coupling coefficient; c'= coupling coefficient; T= temperature, P= pore pressure

Hydraulic and thermal diffusivity can also be expressed by the equations below (Venkanna 2010) & (Cosse 1993).

$$c = \frac{k}{\varphi \mu c_t} \qquad 5.3$$

Where k is the permeability, φ is the porosity, μ is the dynamic viscosity and c_t is the compressibility of fluid.

$$c_o = \frac{k_o}{\rho c_p} \qquad 5.4$$

Where k_o is the thermal conductivity, ρ is the density and c_p is the specific heat capacity.

In the equations above, the first terms with the c_o in equation 5.1 is the temperature change due to heat conduction. The first term with c_o' shows the temperature changes due to heat convention and the second term show the temperature change due to pressure diffusion. In equation 5.2, the terms with c shows the pore pressure diffusivity due to net hydraulic force and the term with c' shows the pore pressure change due to temperature variation (Ewy 2005).

In order to generate a less complicated solution to the above equation, some assumptions were taken to get a simplified solution. Firstly, for low permeable formations such as Shale, the convection term above in equation 5.1 can be neglected as it is very small. Also, the coupling coefficient in 5.1 is very small too compared to the thermal diffusivity and hence the whole term with this coupling coefficient can be neglected (C. Chen 2001). In this case the above equations can be partially decoupled and can be expressed as equations 5.5 and 5.6. In order to ensure the validity of the above assumption, a numerically solved solution was plotted for the equations 5.1 and 5.2 and it was compared with their analytical. Figure 22 below shows the visual illustration

of numerical and approximated analytical solution generated by Chen & Chenevert (C. Chen 2001). It was seen that the results had an error of only 1% ensuring that the assumptions taken the heat convection effect and coupling coefficient term equal to zero (C. Chen 2001).

$$\frac{\partial T}{\partial t} = c_o \left(\frac{\partial^2 T}{\partial r^2} + \frac{1}{r} \frac{\partial T}{\partial r} \right) \tag{5.5}$$

$$\frac{\partial P}{\partial t} = c \left(\frac{\partial^2 P}{\partial r^2} + \frac{1}{r} \frac{\partial P}{\partial r} \right) + c' \frac{\partial T}{\partial t} \tag{5.6}$$

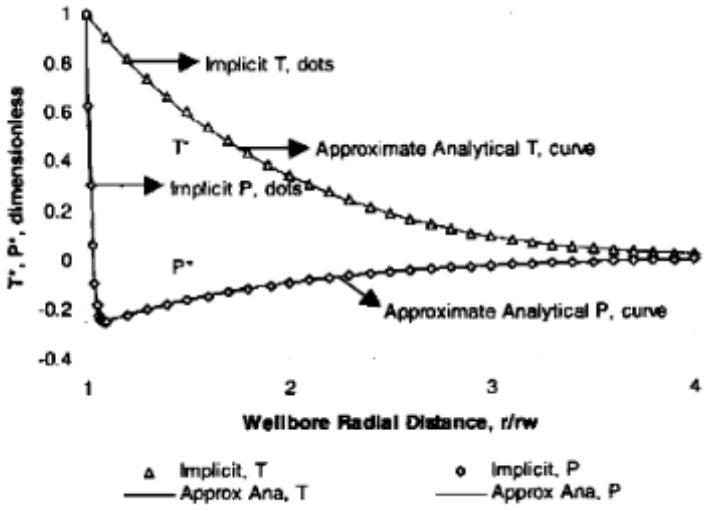

Figure 22: Approximate analytical and implicit solution for the temperature and pore pressure profiles (C. Chen 2001)

5.1 Chemical Potential

In order to find the chemical potential or the osmotic pressure increase in a system, Mody & Hale came up with a model which is as below in Equation 5.7 (C. Chen 2001). Note that the membrane efficiency below is coupled in the equation since shale does not have a permeable membrane during the interaction with water. Therefore, in order to take into account the partial membrane of shale, the membrane efficiency is used. The range of $I_m$is between 0.01-0.1 for shale. Note that the direction of water movement in or out of the shale depends on the activity of the two systems in the well. These are the mud weight water activity and the shale water activity. The activity here is the ratio of vapor pressure of a given liquid divided by the vapor pressure of pure water (Soroush 2013). Activity of any fluid can be controlled by the amount of salt content being put in it which is the salinity. The higher the amount of salt concentration is in a fluid, the lower will be the activity of it (Soroush 2013). The flow of the water will always will be in the direction of the higher activity to low activity and hence the values of activity decide on whether there will be an increase or decrease in pore pressure at the wellbore wall due to the osmotic effect.

If there is an increase in pore pressure, that will decrease the effective stresses in the wellbore which will result in reduced collapse strength and if the pore pressure will decrease the result will be the opposite. Also, if there is an increase in pore pressure due to the chemical effects, then the pore pressure will tend to increase if moved away from the wellbore but it will eventually reduce if the pore pressure profile is observed away from the wellbore wall. This is due to the balancing of the hydraulic effect and the osmotic effect and then the hydraulic effect surpassing this effect resulting in a decrease in pore pressure (Mengjiao Yu 2003). This combine effect of hydraulic and osmotic effect can be seen in Figure 23 and 24 below. It can be seen that when the water is flowing into the formation due to osmotic effect in Figure 24, the pore pressure tends to increase till a certain point after which it starts decreasing again and then when the water is coming out, there is just a decrease in pore pressure when moved away from wellbore wall. Also note that the pore pressure is increased at the wall whenever the mud weight density is increased due to a higher hydraulic force on the wall due to the difference in the initial pore pressure and the well pressure.

$$P_\pi = -I_m \frac{RT}{V} ln \frac{a_{wm}}{a_{wsh}} \qquad 5.7$$

Where P_π is the chemical potential, I_m is the membrane efficiency, R is the gas constant, T is temperature of the well wall, V is the partial molar volume of water, a_{wm} is the activity of drilling mud and a_{wsh} is the activity of shale.

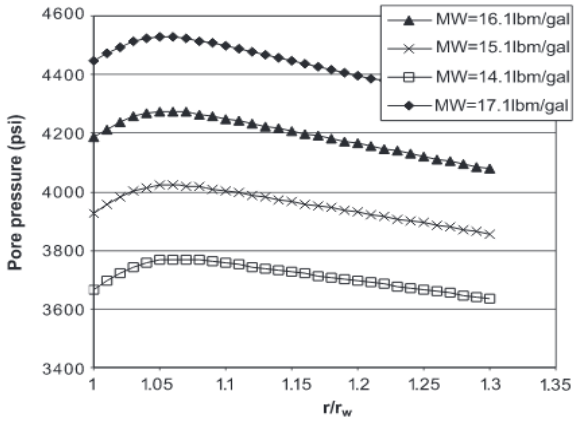

Figure 23:Pore pressure profile when water is being sucked out of shale formation (Mengjiao Yu 2003)

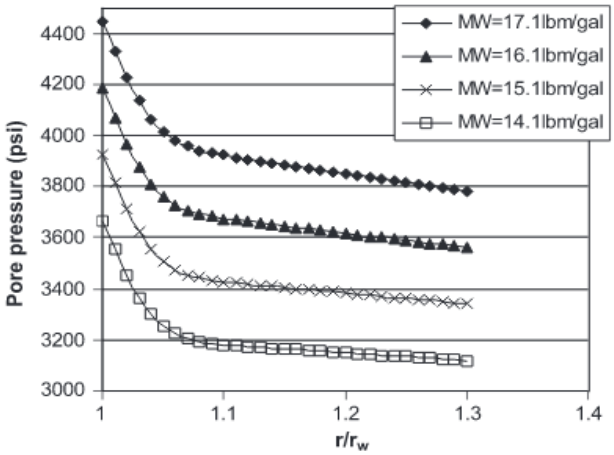

Figure 24: Pore pressure profile when water is being sucked in the shale formation (Mengjiao Yu 2003)

5.2 Rock Temperature

In order to get a solution for equation 5.5, Carslaw & Jaeger (1959) came up with an analytical solution for this equation for short time and distance. The solution was as below (C. Chen 2001):

$$T(r,t) = T_o + (T_w - T_o)\sqrt{\frac{r_w}{r}}erfc\left\{\frac{r - r_w}{2\sqrt{c_o t}}\right\} \qquad 5.8$$

Where erfc is the complementary error function, T_o is the formation temperature, T_w is the well wall temperature, r_w is the well radius, r is the distance away from the wellbore center, t is the time and c_o is the thermal diffusivity.

With the use of the above equation, the temperature profile could be known with respect the wellbore radius and specific radius and at any time for small distances and time. These temperature changes will have an effect on the effective stresses and hence the collapse strength.

5.3 Pore Pressure

A reduced pore pressure solution as also derived analytically from the equation 5.6 above in order to get a profile of the pore pressure with respect to the time and the radius of the wellbore as in equation 5.9 (C. Chen 2001). Note that again the solution here is reduced for short distance and time as that is the main area of interest (C. Chen 2001). The first part in the equation below shows the hydraulic diffusivity effect on the pore pressure. It takes into account the net driving force which is the difference between the well pressure and the sum of chemical potential and initial pore pressure. The second term takes into account the change in pore pressure profile due to the temperature effects in the wellbore or the thermal diffusivity. Note that if the wall temperature is higher than the formation temperature this will tend to increase the pore pressure.

$$p(r,t) = p_o + (p_w - p_\pi - p_o)\sqrt{\frac{r_w}{r}}\,erfc\left\{\frac{r - r_w}{2\sqrt{ct}}\right\} - \frac{c'(T_w - T_o)}{1 - c/c_o}\sqrt{\frac{r_w}{r}}\left[erfc\left\{\frac{r - r_w}{2\sqrt{ct}}\right\} - erfc\left\{\frac{r - r_w}{2\sqrt{c_o t}}\right\}\right] \quad 5.9$$

Where p_w is the well pressure, p_π is the chemical potential and p_o is the initial pore pressure.

5.4 Stresses induced by chemical and thermal changes

Once the temperature and pore pressure profiles are known, the stresses induced due to hydraulics of fluid flow and the temperature can be known from equation 5.10 below (C. Chen 2001). Note that in all the equations, the first term is the induced stresses due to fluid flow. Second term is the induced stress due to the thermal effects and the last term is the stresses induced due to well pressure. The last term only considers pressure for a cylindrical profile. In order to get this term in terms of in-situ stresses for a well, the Kirsch's equation 3.3 above is to be coupled instead to calculate the induced stresses due to well pressure and in-situ stresses around a wellbore. Also note that the first two terms in the equations below have a constant term in the start which depends on the young's modulus, poisons ratio, volumetric expansivity and Biot's constant of the formation.

$$\sigma_{rr} = \frac{\alpha(1-2v)}{1-v}\frac{1}{r^2}\int_{r_w}^{r} p^f(r,t)rdr + \frac{E\alpha_m}{3(1-v)}\frac{1}{r^2}\int_{r_w}^{r} T^f(r,t)rdr + \frac{r_w^2}{r^2}P_w$$

$$\sigma_{\theta\theta} = -\frac{\alpha(1-2v)}{1-v}\left[\frac{1}{r^2}\int_{r_w}^{r} p^f(r,t)rdr - p^f(r,t)\right] - \frac{E\alpha_m}{3(1-v)}\left[\frac{1}{r^2}\int_{r_w}^{r} T^f(r,t)rdr - T^f(r,t)\right] - \frac{r_w^2}{r^2}P_w \quad 5.10$$

$$\sigma_{zz} = \frac{\alpha(1-2v)}{1-v}p^f(r,t) + \frac{E\alpha_m}{3(1-v)}T^f(r,t)$$

Where E = Young's modulus, α_m = volumetric linear thermal expansion coefficient of rock matrix (K^{-1})

5.5 Stresses at the wellbore wall

In order to reduce the above equations at the wellbore wall, the integrals above can be removed from the equation and the above stress equations can be written as below (C. Chen 2001). Again for the wellbore, the kirsch's equations in equation 3.3 are to be coupled with equations below to get final stress fields in wellbore.

$$\sigma_{rr} = p_w$$

$$\sigma_{\theta\theta} = \frac{\alpha(1-2v)}{1-v}(P_w - P_\pi - P_o) + \frac{E\alpha_m}{3(1-v)}(T_w - T_o) - p_w \quad 5.11$$

$$\sigma_{zz} = \frac{\alpha(1-2v)}{1-v}(P_w - P_\pi - P_o) + \frac{E\alpha_m}{3(1-v)}(T_w - T_o)$$

6 Simulation of different scenarios for Well Instability

Since the new pore pressure and stresses around the wellbore can be known from the equations above, any collapse failure model from above can be used with these new stresses and pore pressures in order to get a new collapse pressure profile and observe the effects of the hydraulic diffusion, thermal and chemical changes. For the purpose of this report, Drucker-Prager Criteria is used. The main objective of the simulation study is to learn the effect of various driving forces on the failure envelope and around the near wellbore about 1.3 times the radius of the well. During the study, a single and the combined effects of the driving forces will be evaluated.

In order to see the effects of chemical, diffusion and temperature, the pore pressure variation is observed away from the wellbore to see how these conditions effects the pore pressure and hence the failure index or the effective collapse strength as shown in equation 4.33. The data to perform simulation can be seen in Table 8. The time for all the simulations below was taken to be 10 hours and all the changes in pore pressure are known at this specific time with the help of equation 5.9 above. Equation 5.9 is a complete solution for the chemical, thermal and diffusivity effects. It can be divided into three different parts in order to get the solutions for only one effect or combination of two or all three effects. Also, note that the cohesive strength is to be taken as 8.0695 MPa instead of 8.736 MPa for all simulations at time 10 hours. This is to take into account the change in cohesive strength with respect to time as explained in equation 4.7 above. The initial pore pressure is taken as 66.94 MPa and both horizontal in-situ stresses are assumed to be equal. The mud weight pressure for all simulations is taken to be 78.345 MPa. The well is also assumed to be vertical for the simulations. The effect on the collapse strength due to change of inclination will be shown later in the report. All the pore pressure profiles are calculated using ‘Matlab’ and the data is put into excel to make relevant graphs. Matlab codes are attached to the appendix of this report.

The models presented in the section above for pore pressure and temperature doesn’t take into account the horizontal stresses. In this thesis, these models as explained above are coupled with the Kirsch’s equations and the results are generated.

Variables	Symbol	Value	Unit
Shale activity	a_{wsh}	0.915	Dimen-sionless
Mud activity	a_{wm}	0.78	Dimen-sionless
Membrane efficiency	l_m	0.1	Dimen-sionless
Geothermal gradient	G_g	2	°K/100 m
Overburden gradient	σ_v	0.01945	MPa/m
Minimum horizontal in-situ stress gradient	σ_h	0.01877	MPa/m
Maximum horizontal in-situ stress gradient	σ_H	0.01877	MPa/m
Mud gradient	M_w	0.0180	MPa/m
Pore pressure gradient	p_o	0.01538	MPa/m
Depth (TVD)	D	4352.5	m
Well azimuth	A_{zim}	30	Degree
Well inclination	I_w	0	Degree
Wellbore radius	r_w	0.127	m
Drained Poisson's ratio	v	0.22	Dimen-sionless
Biot's parameter	α	0.80	Dimen-sionless
Tensile strength	σ_t	0.689	MPa
Initial cohesive strength	C_0	8.736	MPa
Equilibrium cohesive Strength	C_e	5.192	MPa
Cohesion alteration Factor	a^*	-0.5	Dimen-sionless
Shale Young's modulus	E	6895	MPa
Failure criteria		Drucker-Prager	
Friction angle	ϕ	30	Degree
Time	t	0, 8640, 86,400, 864,000	s
Pore fluid or mud hydraulic diffusivity	c	3.40e-10	m^2/s
Thermal diffusivity of porous media	c_0	9.54e-7	m^2/s
Coupling coefficient	c_0'	4.25e-14	m^2/s-MPa
Coupling coefficient	c'	0.124	MPa/°K
Volumetric thermal expansion coefficient of pore fluid (water)	α_f	5e-4	$°K^{-1}$
Volumetric thermal expansion coefficient of rock matrix (shale)	α_m	2.59e-5	$°K^{-1}$
Wellbore wall temperature	T_w	350.7	°K
Rock initial temperature	T_0	375.7	°K

Table 8: List of input parameters for modeling (C. Chen 2001)

6.1 Chemical, Diffusion and Temperature effects

Simulations in Figure 25 and 26 takes into account all effects which are the chemical, thermal and diffusion. Initially, the mud weight is increased from the initial mud or well pressure of 78.4 MPa and the effect on the pore pressure at the wall and away from it is observed. It can be seen that pore pressure at the wall increases as the well pressure is increased and decreases in an exponential manner until it reaches its initial state of 66.94 MPa at some distance away from the wellbore wall. The increase in the pore pressure due to well pressure was equal to the increase in mud well pressure from its initial state.

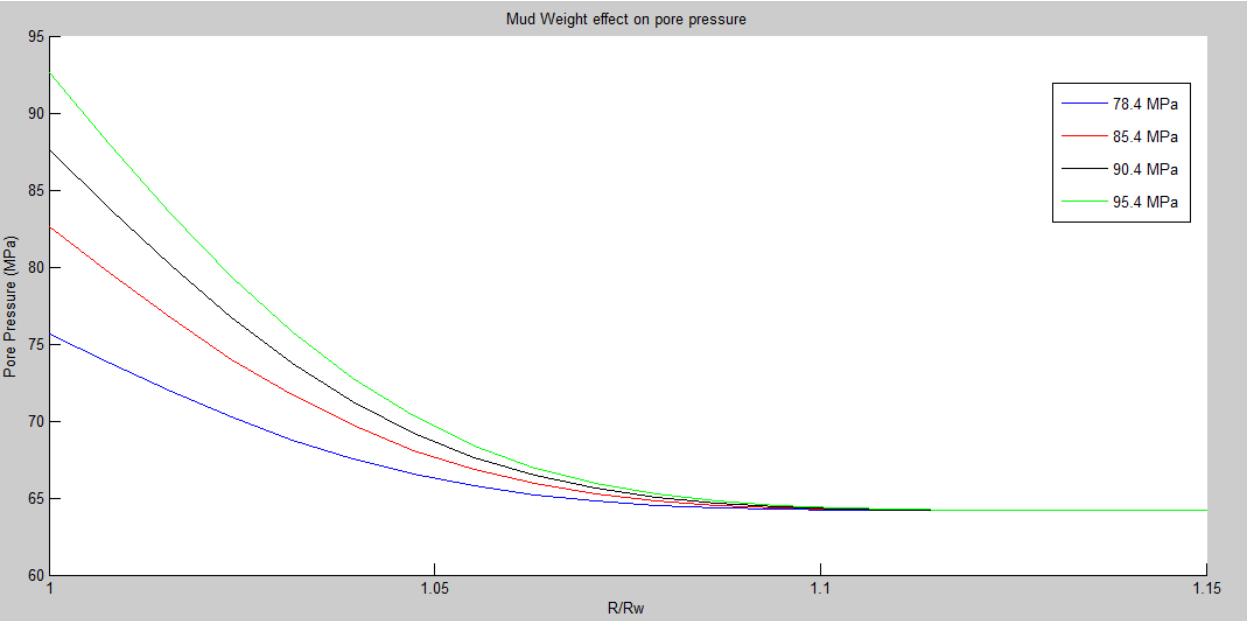

Figure 25: Mud weight effect on pore pressure

Another simulation was run on Matlab to see the effect of time. It can be seen once the time is increased, the effects can be seen further away from the wall on the pore pressure and the initial pore pressure is not even seen at a specific radius of 1.3 for long times as for the case when the time was 1 minute. At 1 minute, the effects were only seen at the very near wellbore wall and the pore pressure at any distance away was equal to the initial state.

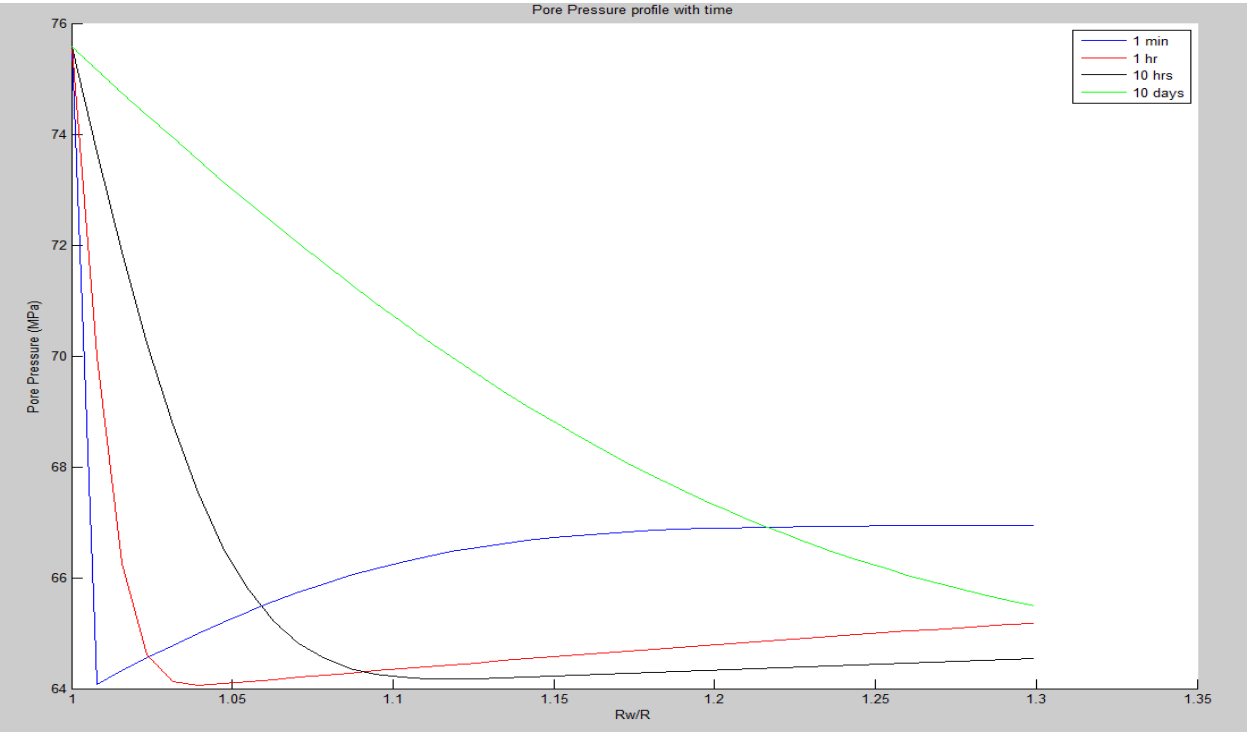

Figure 26: Pore pressure profile at different times

6.1.1 Chemical

In order to observe the chemical effects, equation 5.7 is used. Note that the chemical effects are only applicable to the wellbore wall and the effect can only be seen when specific radius 'R/Rw' is equal to one. This effect can be seen in Figure 27 below. A reduction in initial pore pressure is seen only on the wall and if moved away from the wall, the pore pressure tends to go back to its original initial position. Due to the pore pressure decrease at the wall, an increase in the effective collapse stress is seen in Figure 28. Once the effect is not there anymore, effective collapse stress graph tends to follow the same path as it had without any effects considered as seen in Figure 29. Note that since the activity of the formation was higher than the activity of the mud, the formation fluid was flown out of the formation which resulted in this decrease of the pore pressure. If the activity would have been higher in the mud compared to that of the shale formation, an increase in the pore pressure at the wall would have been observed. Such an observation will be shown below in the report when discussing the effects for different properties affecting the collapse stress results.

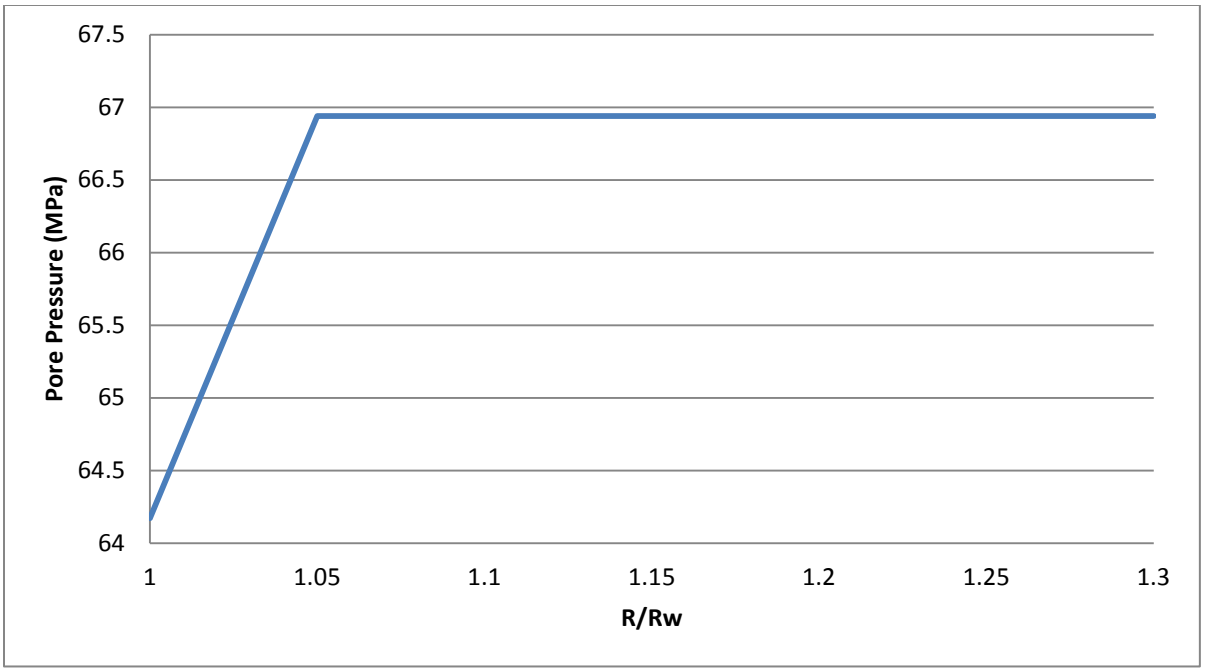

Figure 27: Pore Pressure graph for chemical effects

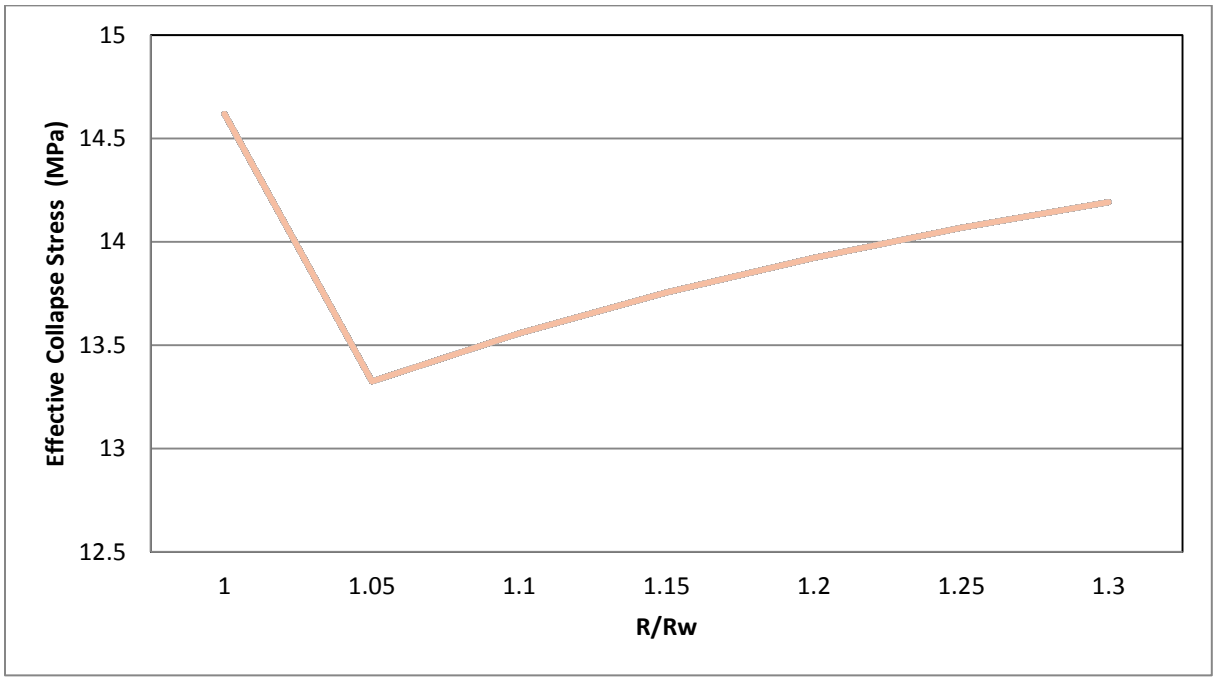

Figure 28: Effective Collapse Stress graph for chemical effects

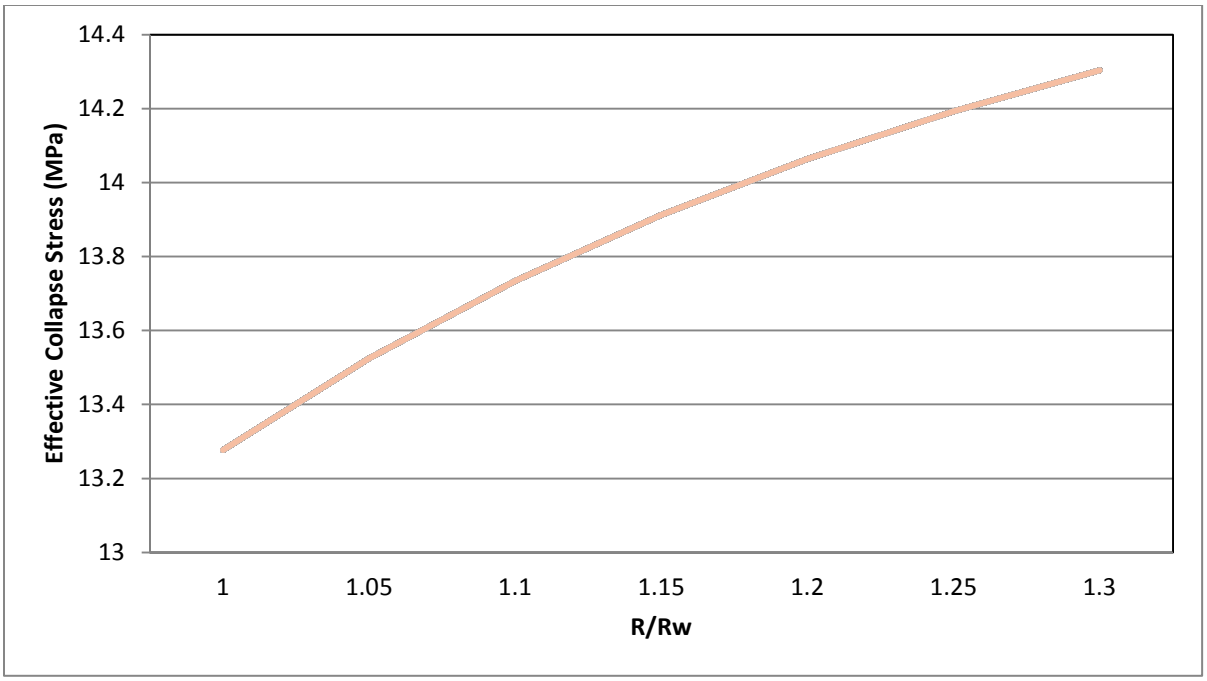

Figure 29: Effective Collapse Stress graph for no effects

6.1.2 Thermal

In order to evaluate the profile of pore pressure due to the temperature effects, equation 5.9 for pore pressure is used. Note that only the second term in the equation 5.9 is used since it takes into account the temperature effects. The pore pressure profile is seen in Figure 30. Near wellbore temperature is lower than the temperature of the formation which results in the thermal diffusivity of the pore pressure. This results in a decrease in the pore pressure as the position is moved away from the wellbore wall. Note that there is no effect at the wall since that is the starting point of the thermal diffusion effect to take place. That is the pore pressure at the wall is 66.94 MPa at all times. Some effects can be seen even till a specific radius of 1.3 as the pore pressure at this point has still not reached its initial state showing the existence of still some temperature effects. An increase in effective collapse stress is seen in the Figure 31 below due to the decrease in the pore pressure till the specific radius of 1.1 after which the gradient of the slope of effective collapse stress decreases due to a slight increase in pore pressure until the specific radius of 1.3.

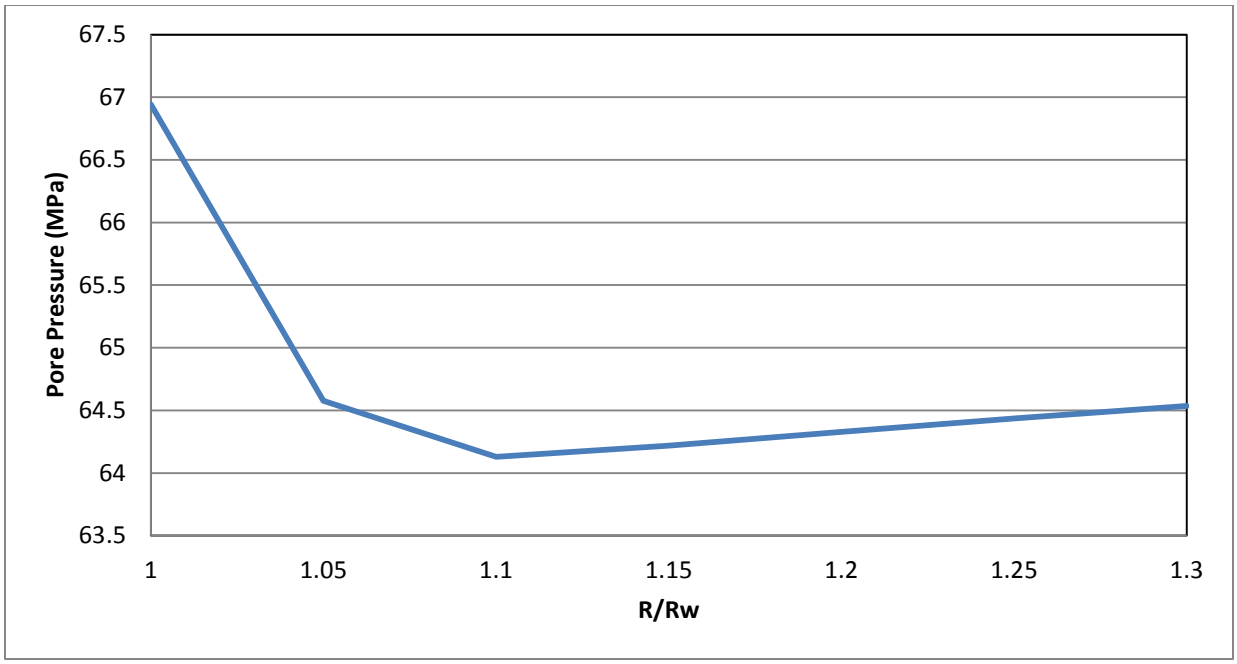

Figure 30: Pore Pressure graph for thermal effects

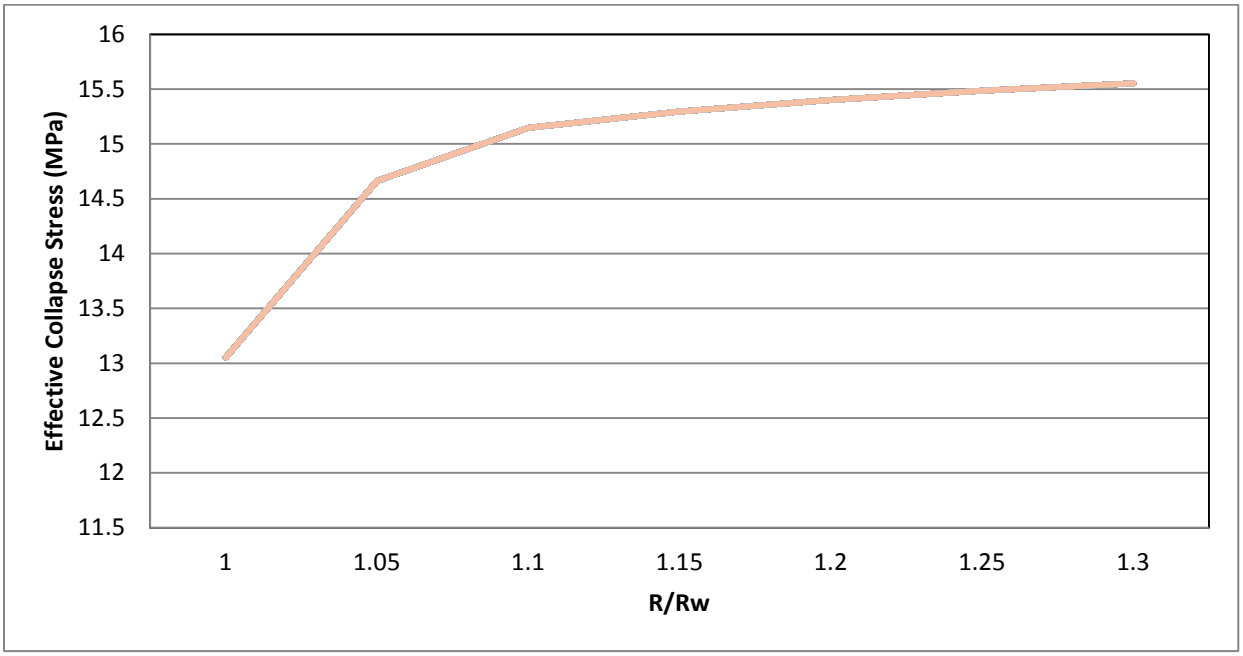

Figure 31: Effective Collapse Stress graph for thermal effects

6.1.3 Diffusion

In order to observe the hydraulic diffusion affect in the formation, the first part for the equation 5.9 only is taken into account which consist of the net hydraulic force. Since, the well pressure is higher than the initial pore pressure; an increase in the pore pressure is seen at the wall due to this hydraulic force. Note that when moved away from the wellbore wall, the pore pressure tends to reduce exponentially until at a certain point where it equalizes to the initial pore pressure. Further away from this point, there will be no more diffusivity effect. At 10 hours, this effect tends to disappear at specific radius of around 1.1. Due to this decrease in pore pressure, the effective collapse stress is hence increased until the point where this effect takes place after which the effective collapse curve tends to follow the normal curve. Also, the effective collapse stress is minimum at the wall due to the increase in pore pressure there and highest in magnitude at the wall.

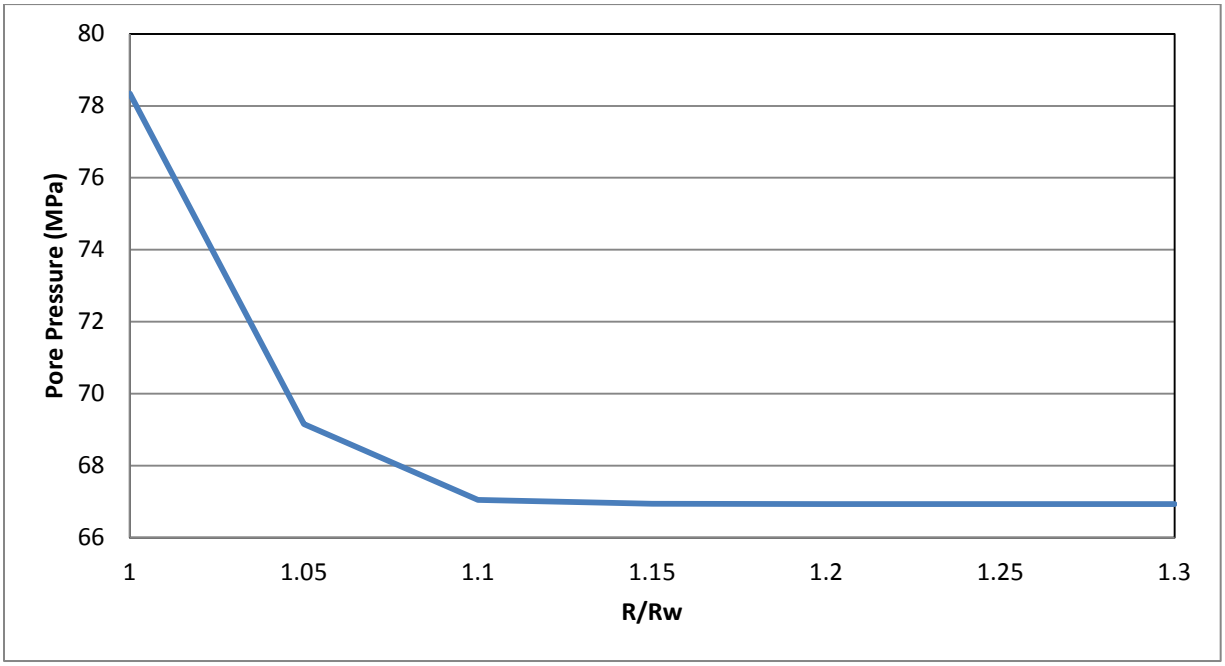

Figure 32: Pore Pressure graph for diffusion effects

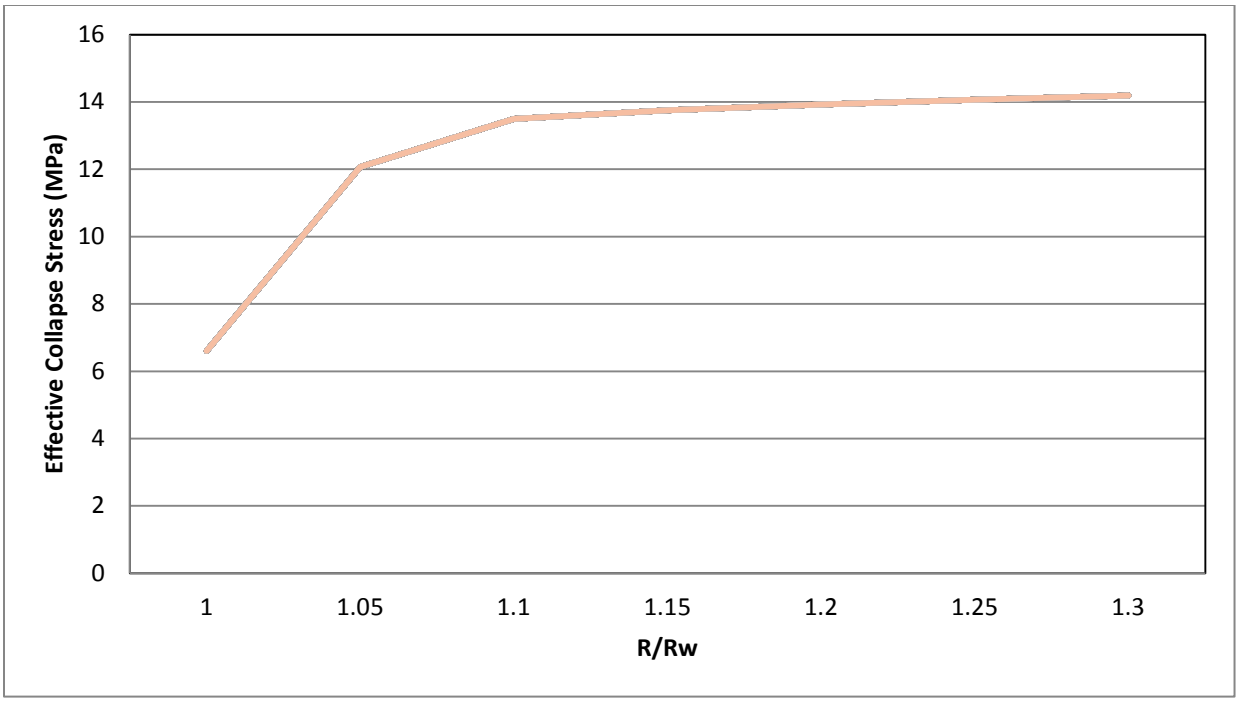

Figure 33: Effective Collapse Stress graph for diffusion effects

6.1.4 Thermal & diffusion

If both thermal and diffusion effects are taken into account, the pore pressure equation above is used again. Note that the only thing not taken into account when dealing with these two is that the near wellbore pressure doesn't involve the chemical potential. The two graphs below were plotted for the pore pressure and the effective collapse stress. Again, the near well bore which is an area of interest shows an increase in pore pressure due to hydraulic diffusivity only and no temperature changes as the thermal effect takes place as moved away from the wall rather than at the wall.

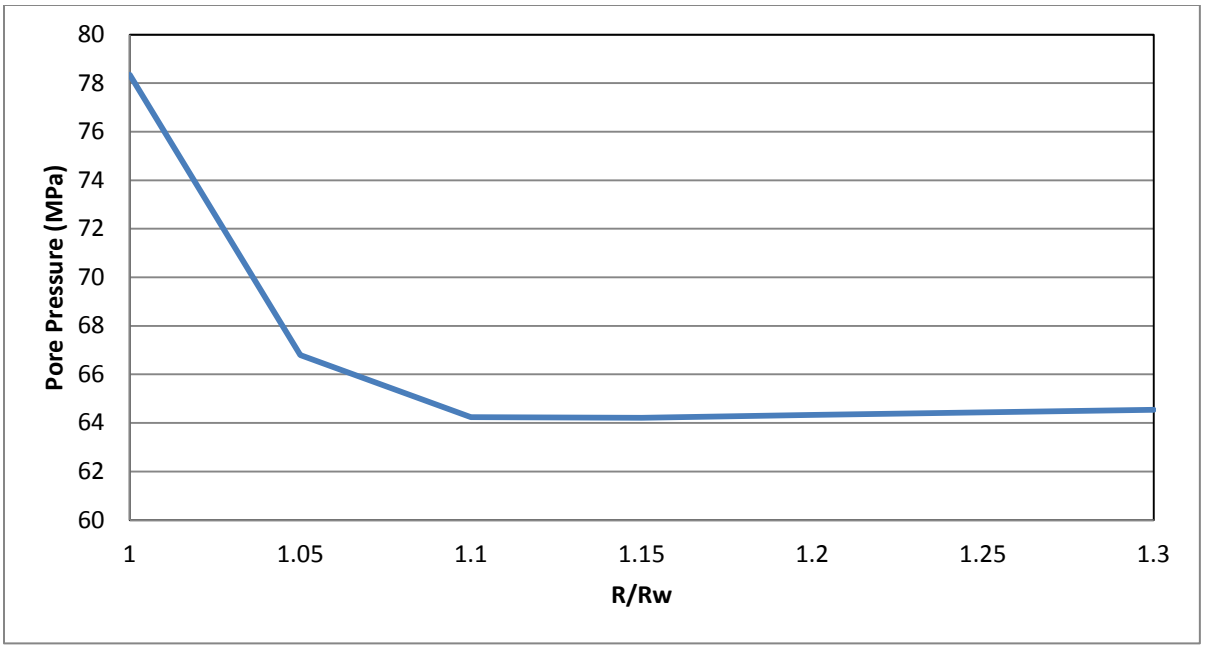

Figure 34: Pore Pressure graph for thermal and diffusion effects

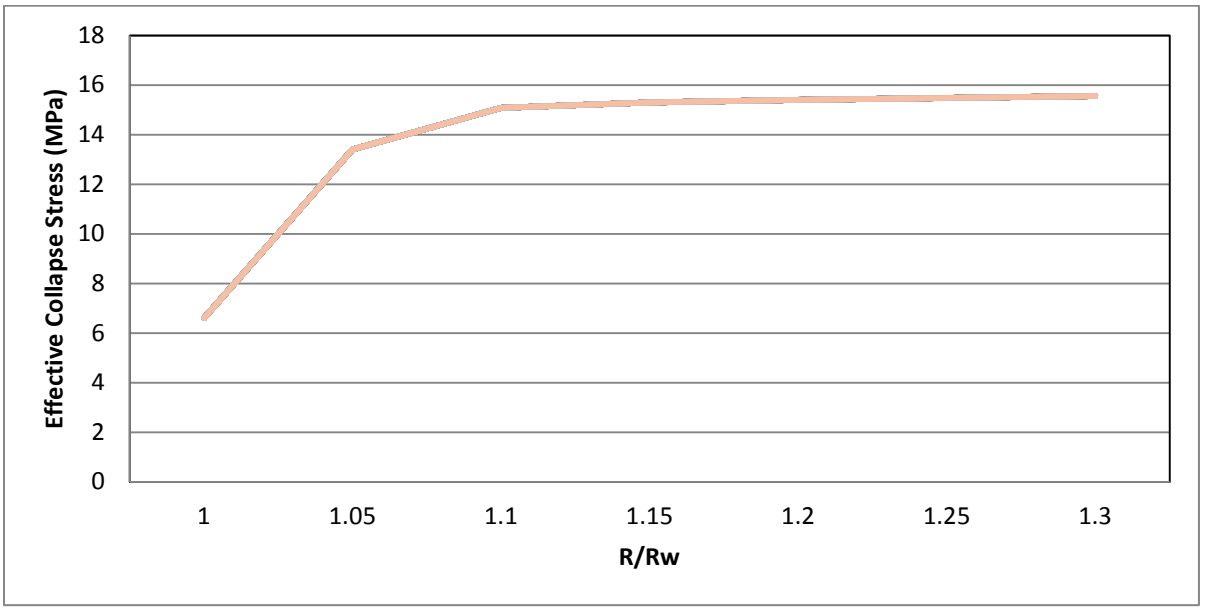

Figure 35: Effective Collapse Stress graph for thermal and diffusion effects

6.1.5 Thermal & chemical

Below is a combination of thermal and chemical effects on the pore pressure and the effective collapse stress.

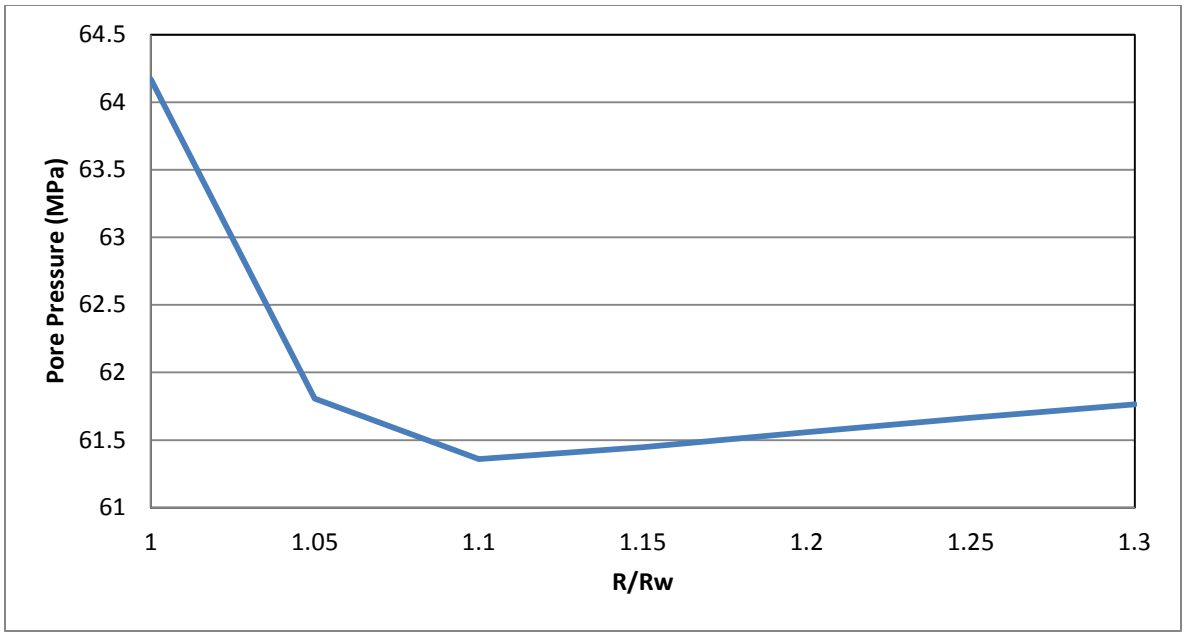

Figure 36: Pore Pressure graph for chemical and thermal effects

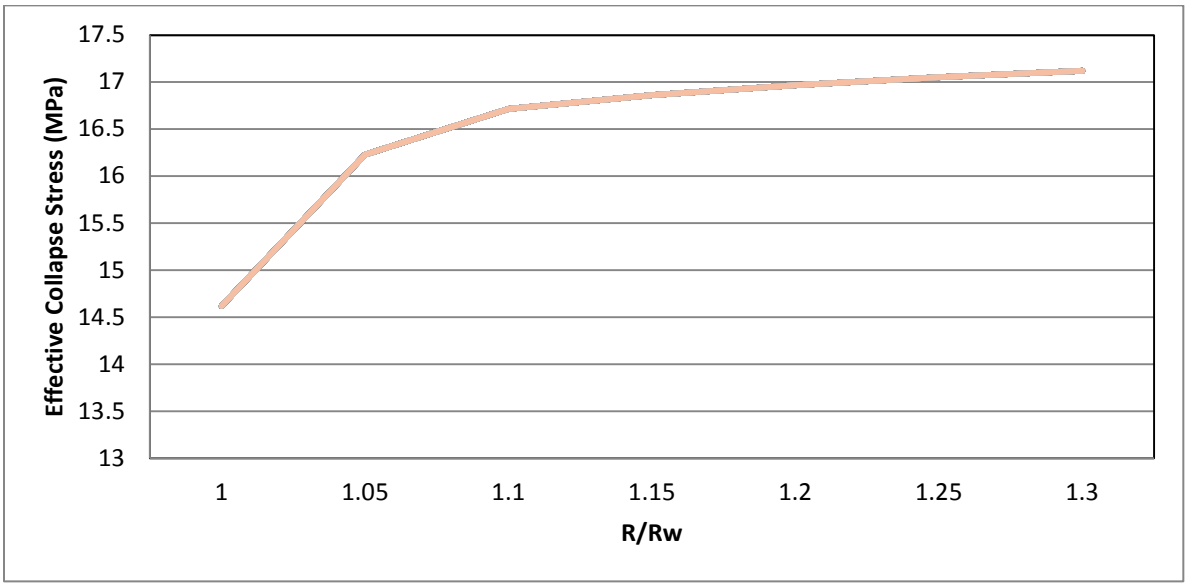

Figure 37: Effective Collapse Stress graph for chemical and thermal effects

6.1.6 Chemical & Diffusion

An interesting thing seen here is that the diffusion effects cannot be seen that far from wellbore. This is because the hydraulic diffusivity effects are less dominant in the early times as permeability is very low for shale and it takes time for this effect to take time compared to the

thermal effects that might be taking place more significantly further away in the wall. This is due to the very low value for hydraulic diffusivity compared to thermal diffusivity resulting in a very slow propagation of the pressure into the formation.

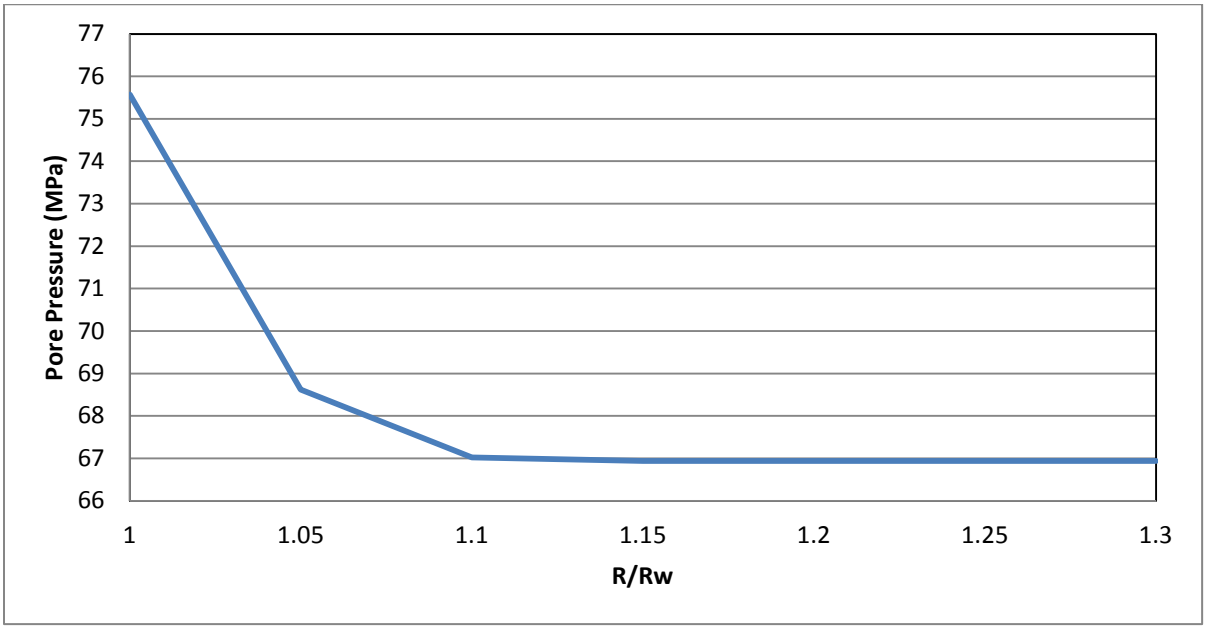

Figure 38: Pore Pressure graph for chemical and diffusion effects

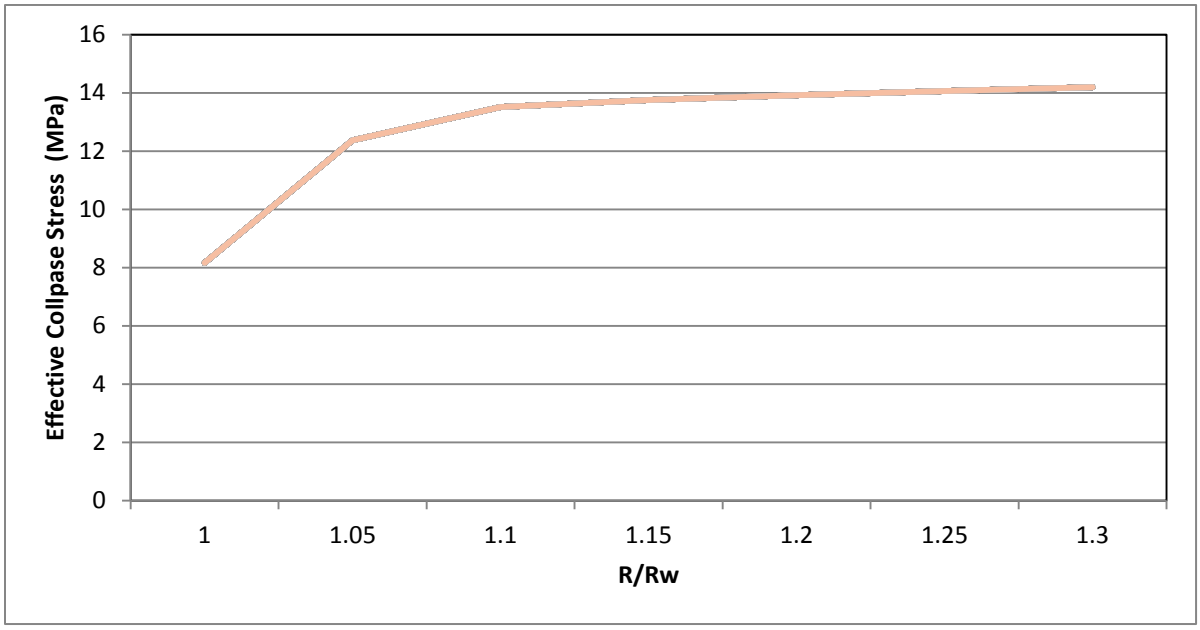

Figure 39: Effective Collapse Stress graph for chemical and diffusion effects

6.1.7 Thermal, chemical & diffusion

Below is a pore pressure and effective collapse curve if all the effects are taken into consideration. They are very similar to the diffusion and temperature graph. The only difference is a further reduction in pore pressure at the wellbore wall due to chemical change.

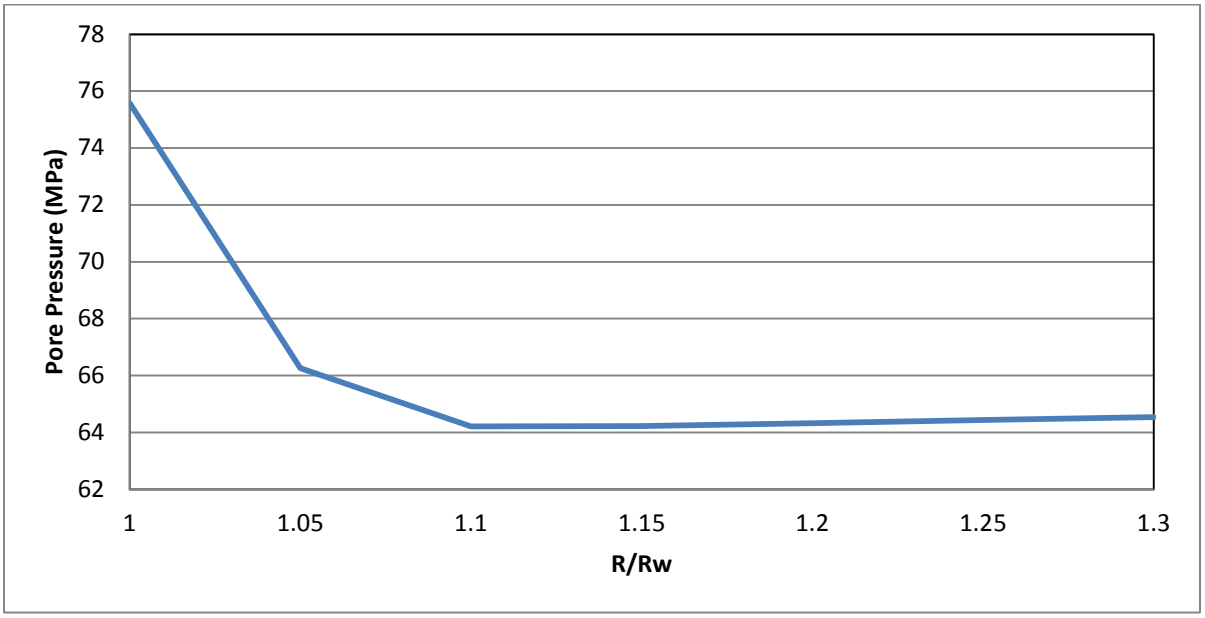

Figure 40: Pore Pressure graph for chemical, thermal and diffusion effects

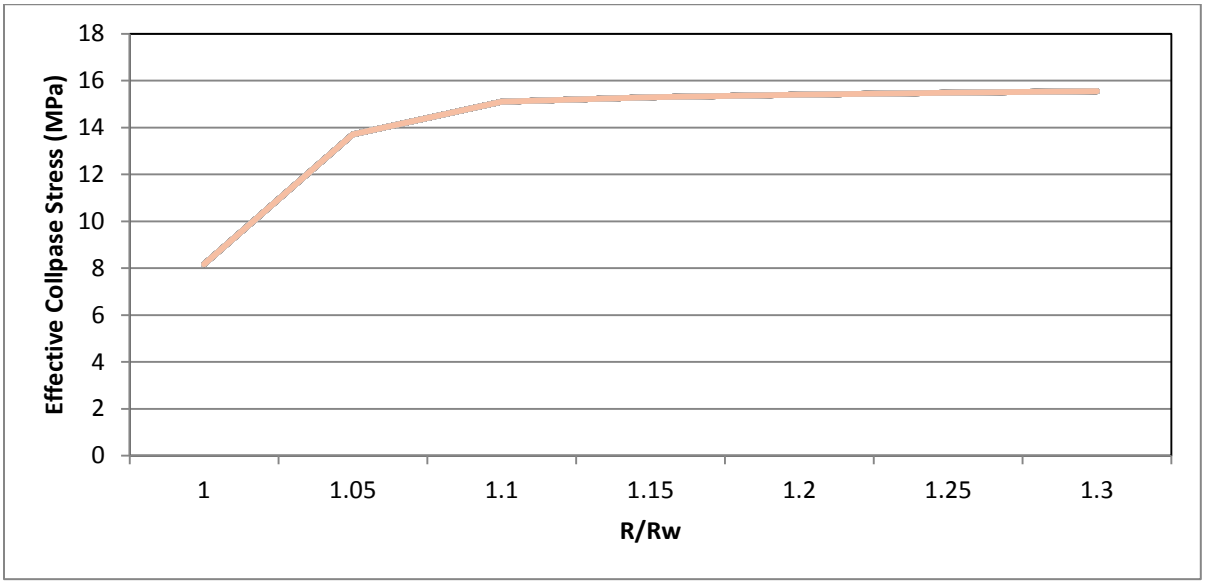

Figure 41: Effective Collapse Stress graph for chemical, thermal and diffusion effects

6.1.8 Discussion and Comparison of different scenarios

From the above results for pore pressure and effective collapse stress under different scenarios, some observations were made at the wellbore wall. The pore pressure tends to decrease at the wall only due to chemical change and no effects are seen away from the wall. For the diffusion effect, an increase in pore pressure is seen due to the net hydraulic force at the wall due to overbalance drilling mud conditions. This is due to assumption made by M. E. Chenevert that the wall is completely penetrating and any increase in well pressure will increase by the magnitude of the difference of the well pressure and the initial pore pressure (C. Chen 2001). In reality, this is not the case and because of this the results might be overstating the pore pressure at this stage. Also, there was no change seen due to temperature effects at the wall. On the other hand, the effects were seen far away from the well even at specific radius of 1.3 due to the temperature effects. This was not seen in diffusion or chemical scenarios where the effects stopped taking place just near the wellbore as the pore pressure tend to return to its initial state. Different pore pressure profiles for different scenarios can be seen in Figure 42 below.

It can easily be seen from Figure 42 and 43 below that the different effects have quite a prevailing effect on the pore pressure and the effective collapse stress and hence cannot be ignored when designing the mud weight window. It can be seen that the effects significantly either reduce or increase the effective collapse strength depending on their respective effects. It was seen that all the curves with the diffusion effect in it tend to reduce the effective collapse strength due to increase in pore pressure due to hydraulic diffusion. Whereas temperature and chemical effects tend to increase the effective collapse strength or decrease the pore pressure.

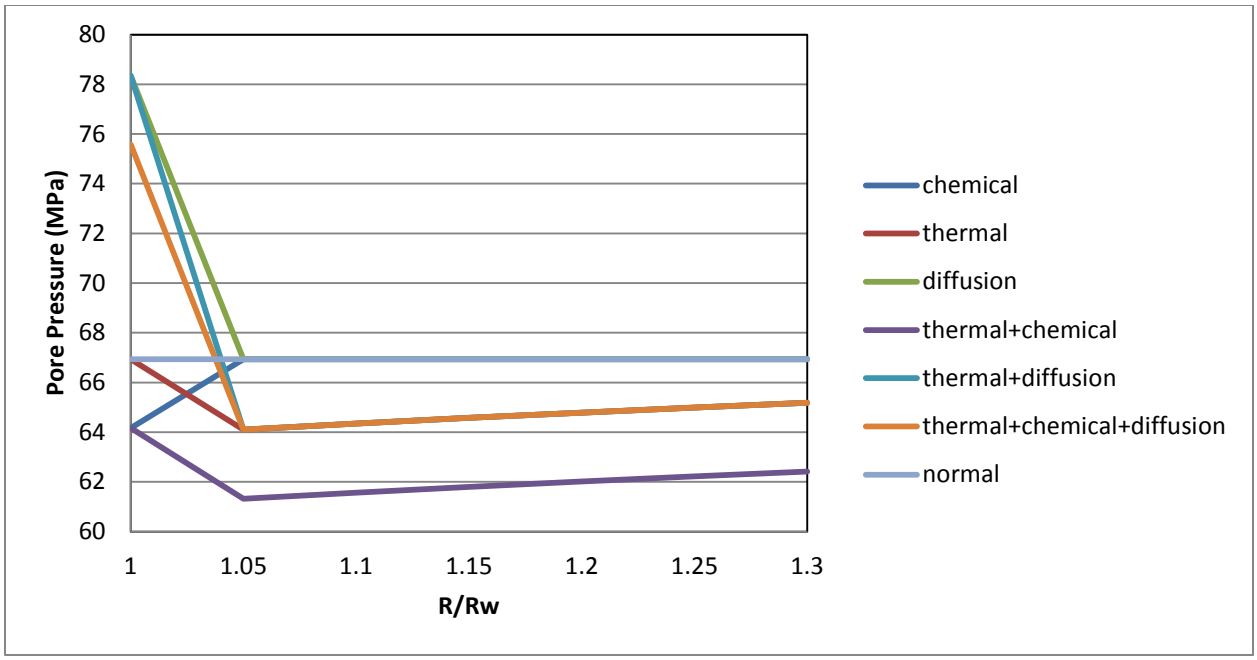

Figure 42: Pore Pressure graph for all scenarios

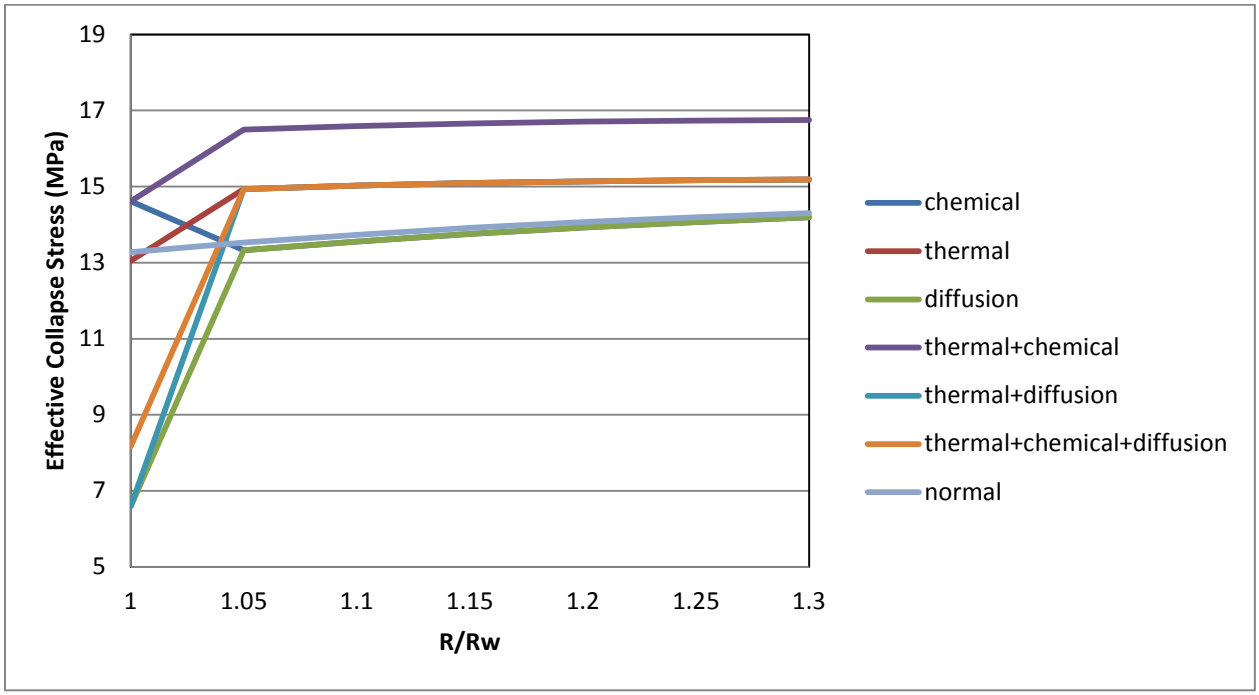

Figure 43: Effective Collapse Stress graph for all scenarios

6.2 Effect of different properties

For the analysis of the effect of different properties, time and inclination of well, all the effects which are chemical, thermal and diffusion are taken into account when performing simulations. The normal pore pressure or effective collapse stress is the one which is performed taking initial parameters which can be seen in Table 8.

6.2.1 Wellbore Wall Temperature

The increase in wall temperature will tend to reduce the temperature difference between the wall and the formation. This resulted in a reduction of the temperature effect on the pore pressure. This can be seen in figure 44 below. Once the wall temperature is reduced or cooled down, the temperature difference increased resulting in a higher decrease in pore pressure and hence a higher collapse stress at specific radius of 1.1 approximately. Note that the temperature will have no effect on the effective collapse stress at the wellbore wall as seen in Figure 45 below.

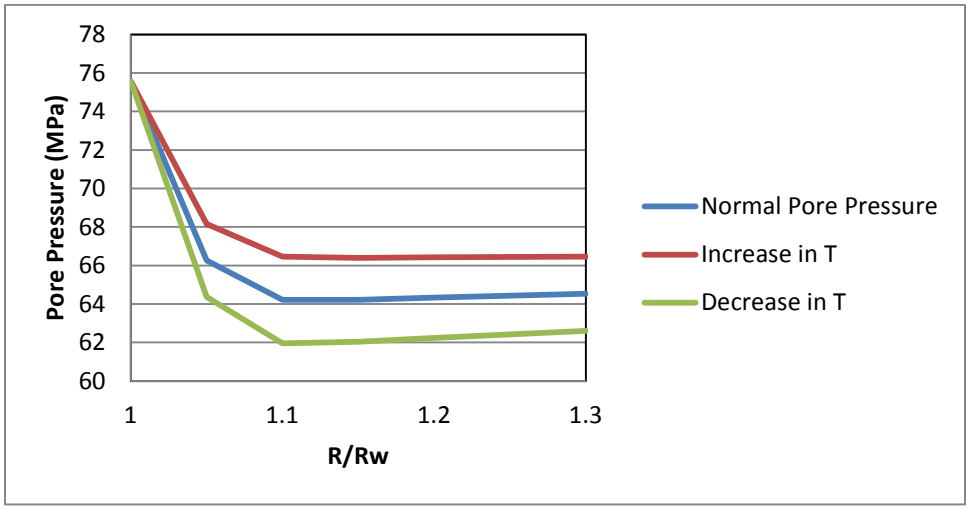

Figure 44: Pore Pressure graph for wall temperature effects

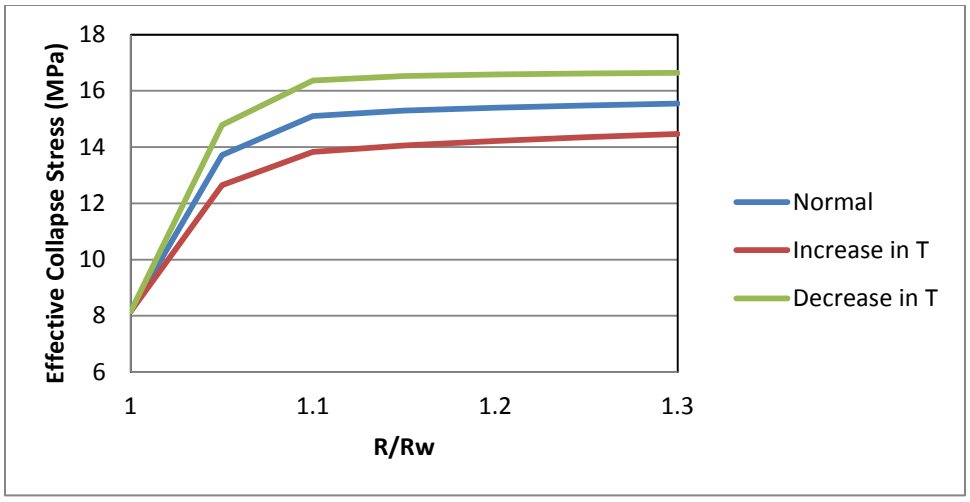

Figure 45: Effective Collapse Stress graph for temperature effects

6.2.2 Effect of activity values

This is one of the most important properties when looking into chemical effects and can affect the collapse stress results significantly. It was seen that with a change in activity, the flow of the fluids direction can be controlled. In this case, activity of the water was kept such that it was higher than the activity of the shale formation which resulted in the pore pressure to increase considerably at wellbore wall. This resulted in reduced collapse strength at the wall which is an important area of interest as most of the collapse happens at the wellbore wall. Therefore, if required the activity of the mud can be always be altered by adding of different solutes in order to get the desired results and flow direction depending on the formation and situation.

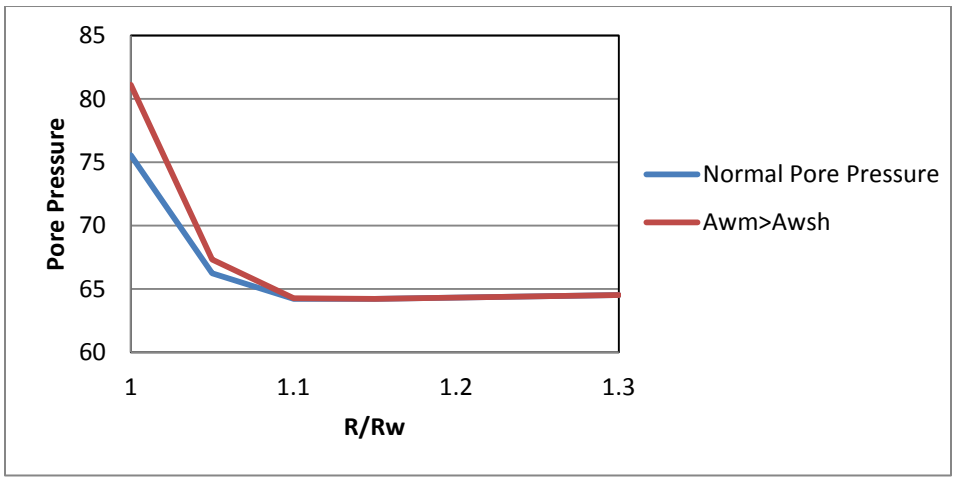

Figure 46: Pore Pressure graph for activity effects

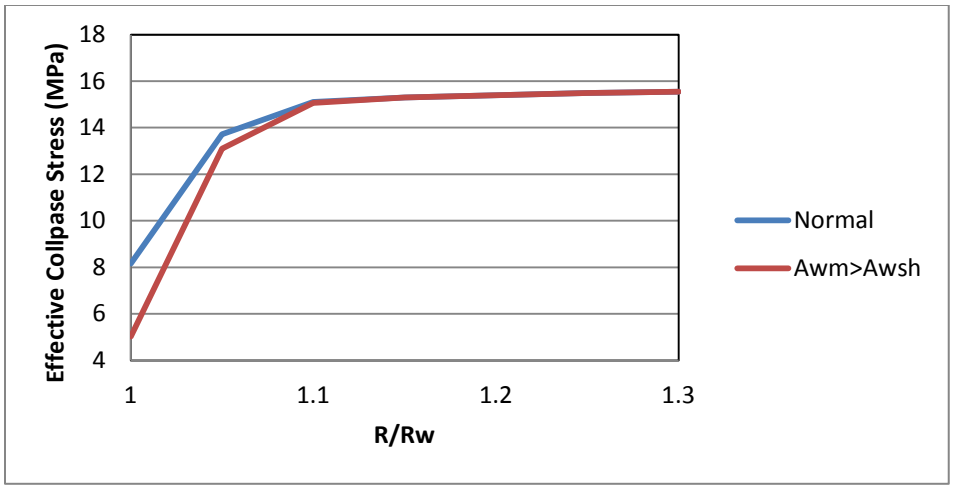

Figure 47: Effective Collapse Stress graph for activity effects

6.2.3 Permeability

When the permeability was increased 100 times in order to see the effect on pore pressure and effective collapse strength, it was seen that the hydraulic diffusivity tends to be more prevailing now compared to the initial permeability condition. It was seen that the pore pressure tends to decrease in a smoother manner rather than the drastic change seen in the original curve. The profile seems to be going a long way away from the wellbore showing that the penetration of this effect is much higher now. This resulted in evener and reduced effective collapse strength in nearby wellbore area. The smooth curve of pore pressure tends to increase the pore pressure due to fluid flowing into formation more easily. Another thing to take into consideration is the assumptions taken at the start of this report regarding the convection component in the pore pressure equation 5.1 which was assumed to be zero as the permeability was very low. Since the permeability is increasing, the convection component might not be very small anymore and because of this there might be a small error in the analysis below.

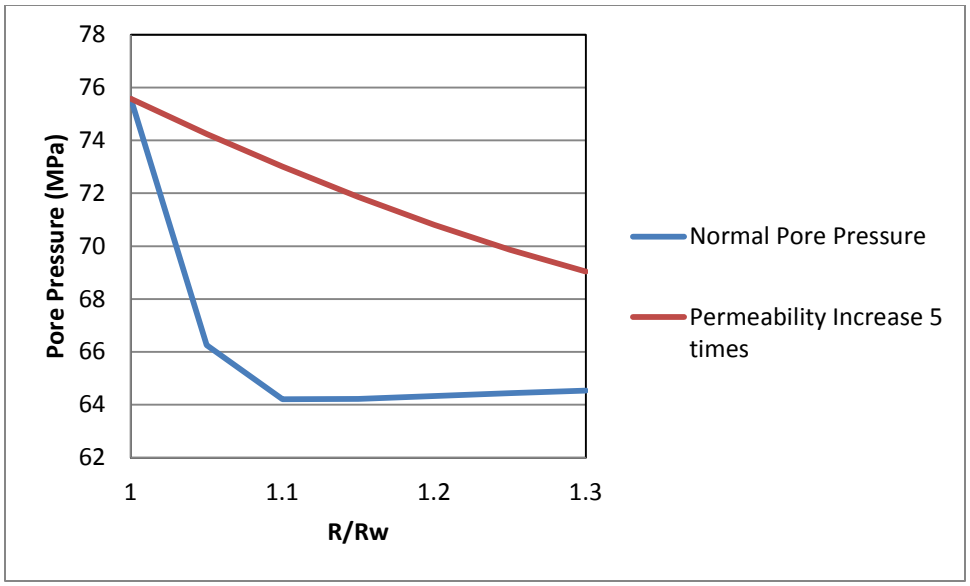

Figure 48: Pore Pressure graph for permeability effects

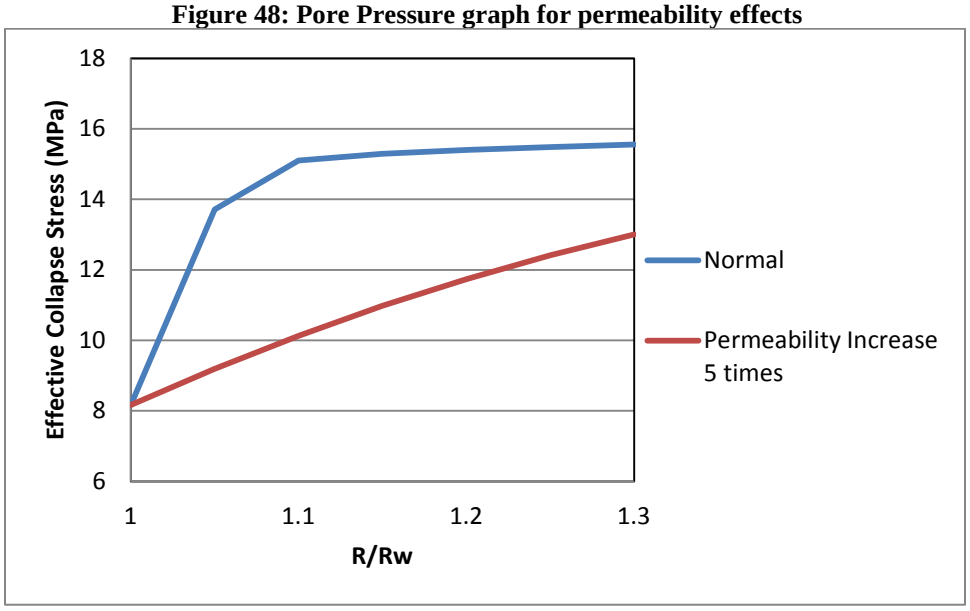

Figure 49: Effective Collapse Stress graph for permeability effects

6.2.4 Thermal diffusivity

The thermal diffusivity was also increased 100 times to see its effect on the pore pressure and effective collapse strength. It was seen that the change in thermal diffusivity affected the pore pressure very minutely. An almost same curve was seen for the new diffusivity. Therefore, it can be concluded that it is a less significant value when dealing with pore pressure effects. The change in temperature difference plays a more significant role when looking for changes in pore pressure.

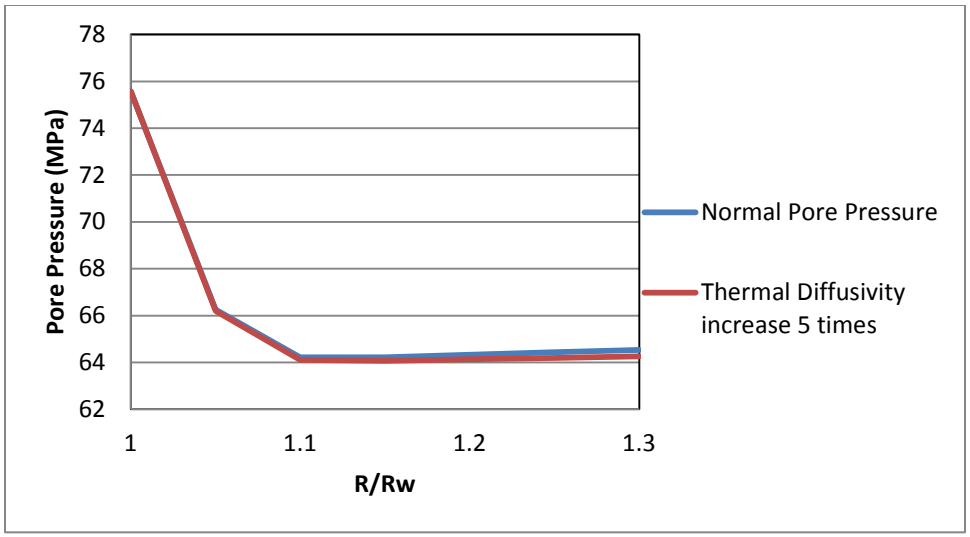

Figure 50: Pore Pressure graph for thermal diffusivity effects

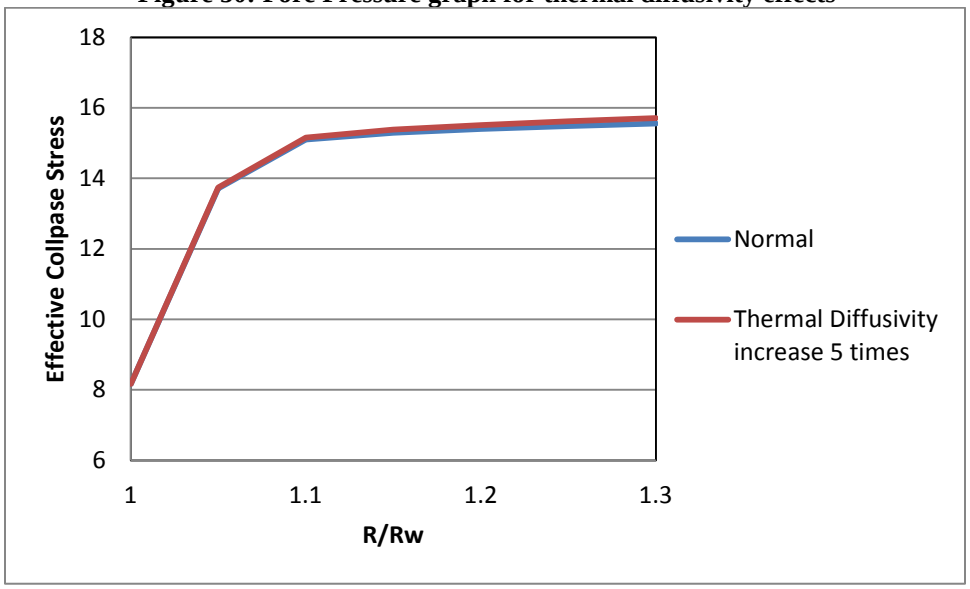

Figure 51: Effective Collapse Stress graph for thermal diffusivity effects

6.3 Effect of time

It can easily be seen that with time the pore pressure tends to go into formation further until reached a far point away from the wellbore wall. The time also results in a significant reduction in effective collapse strength away from the wellbore wall. This can be seen in Figure 53 below. It can be seen that with time the effective collapse stress at the wall remains the same but the nearby area of well becomes weaker with time. Also, another effect on the effective collapse strength with time is due to the reduction in cohesive strength as shown below in Figure 53. This

effect is due to the hydration of shales which weakens it. It can be calculated at different times using equation 4.7. It can be seen that the change is at the wellbore wall which can be a worrying factor when designing the mud weight window. Therefore it is very important to take into account all the changes with time too in order to avoid any well collapse after days from the initial point of drilling.

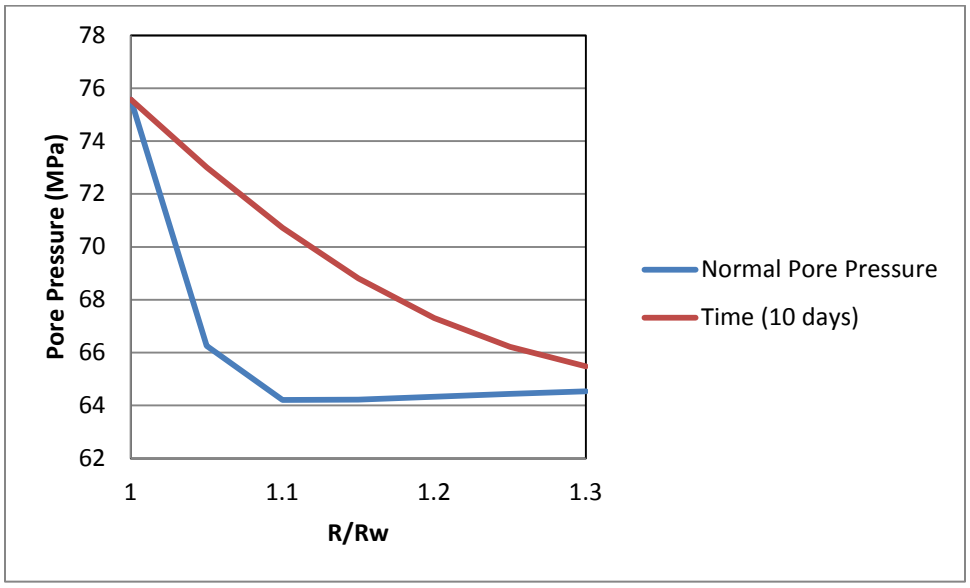

Figure 52: Pore Pressure graph for time effects

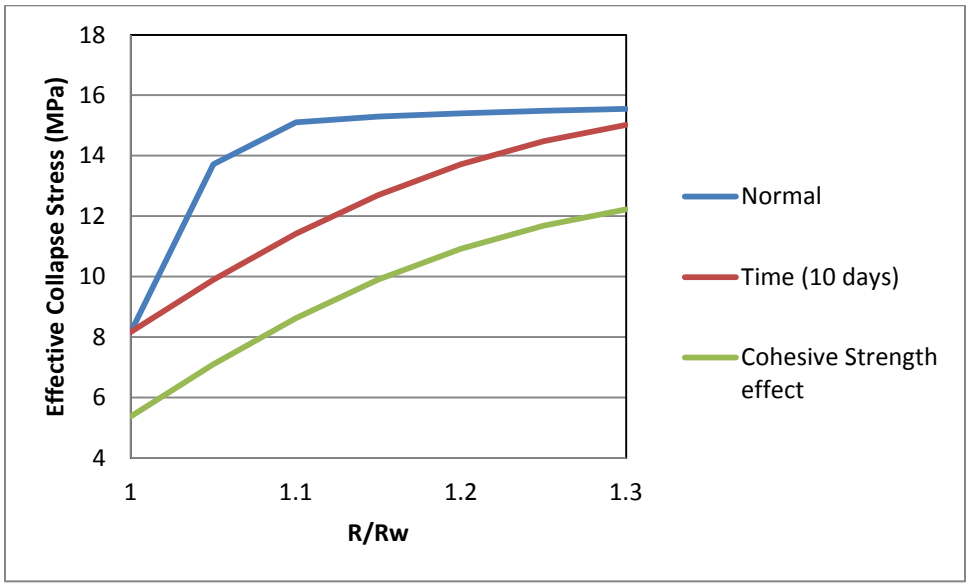

Figure 53: Effective Collapse Stress graph for time effects

6.4 Effect of the inclination of well

Inclination of well has a very strong influence on the stresses around the wellbore as well as the effective collapse stress. In order to observe the changes in principal stresses around a wellbore and the effective collapse stress, some results were generated. Below in Figure 54, hoop stresses for well at zero degrees to the vertical is shown with another one (Figure 55) shown at 90 degrees which will be a horizontal well. It can be seen that for a well at zero inclination, the stresses around the wellbore at a certain radius is same around it at any angle whereas for a horizontal well the stresses around the wellbore vary with respect to the angle. The angle here is the angle with respect to the direction of maximum horizontal in-situ stress. All the stresses are in MPa. All the simulations are done taking into account the chemical, diffusion and thermal effects.

6.4.1 Radial Stresses

The radial stresses tend to increase as moved away from wellbore. For an asymmetrical result, almost same results were seen for the vertical and oriental well. The minimal radial stress was seen at specific radius of one after which the chemical and diffusion effects took place at the wall increasing the pore pressure significantly which resulted in a reduced effective radial stress. Once moved away from wall, the radial stress tends to increase significantly and then starts reducing as moved along the wellbore.

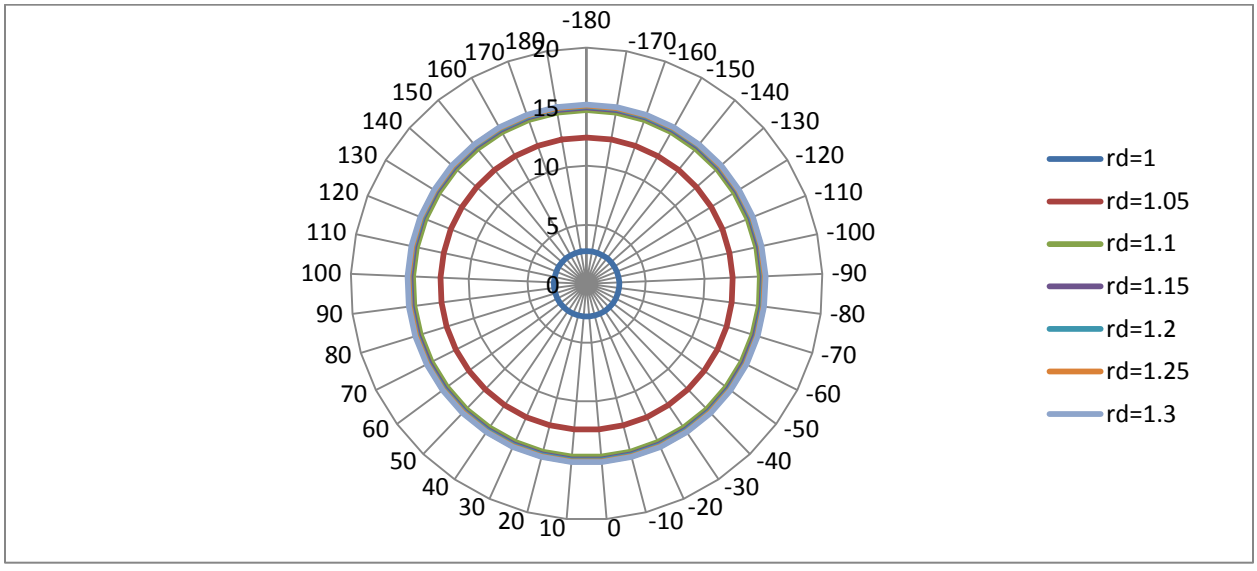

Figure 54: Radial stresses around a wellbore at different specific radius values for a vertical well

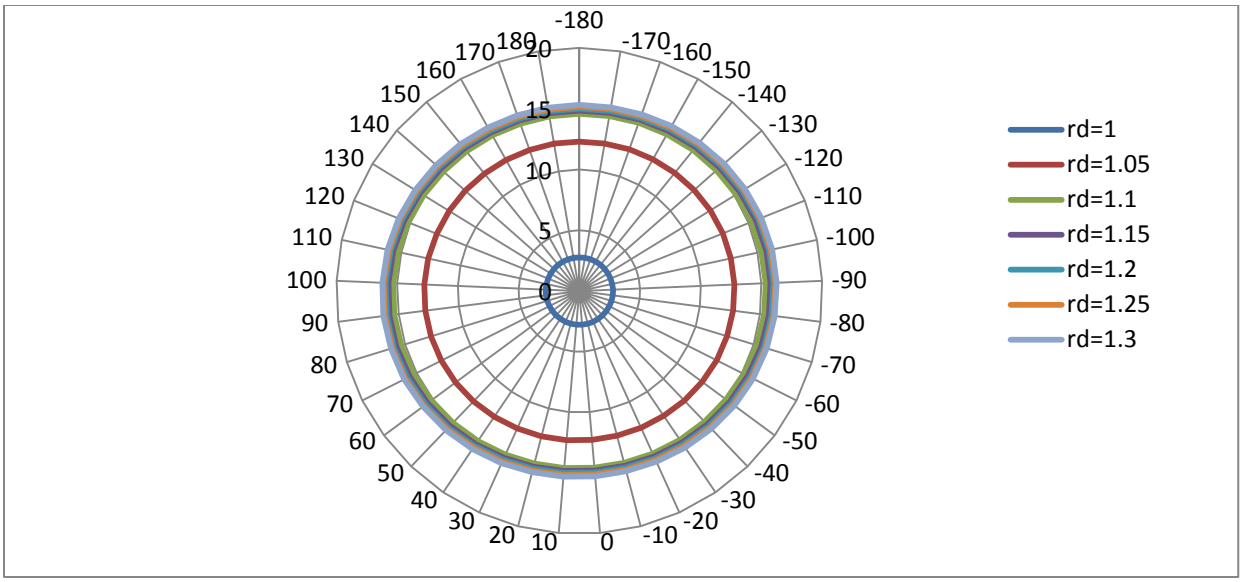

Figure 55: Radial stresses around a wellbore at different specific radius values for a horizontal well

6.4.2 Hoop Stresses

The hoop stresses tend to increase as moved away from the wellbore wall due to pore pressure changes due to chemical, thermal and diffusion effects but once the effects tend to reduce as moved away from wellbore wall, the hoop stress starts to reduce slowly. For the stresses for the horizontal well, the hoop stresses are minimum at 0 degrees and maximum at 90 degrees around the wellbore as expected form the equations.

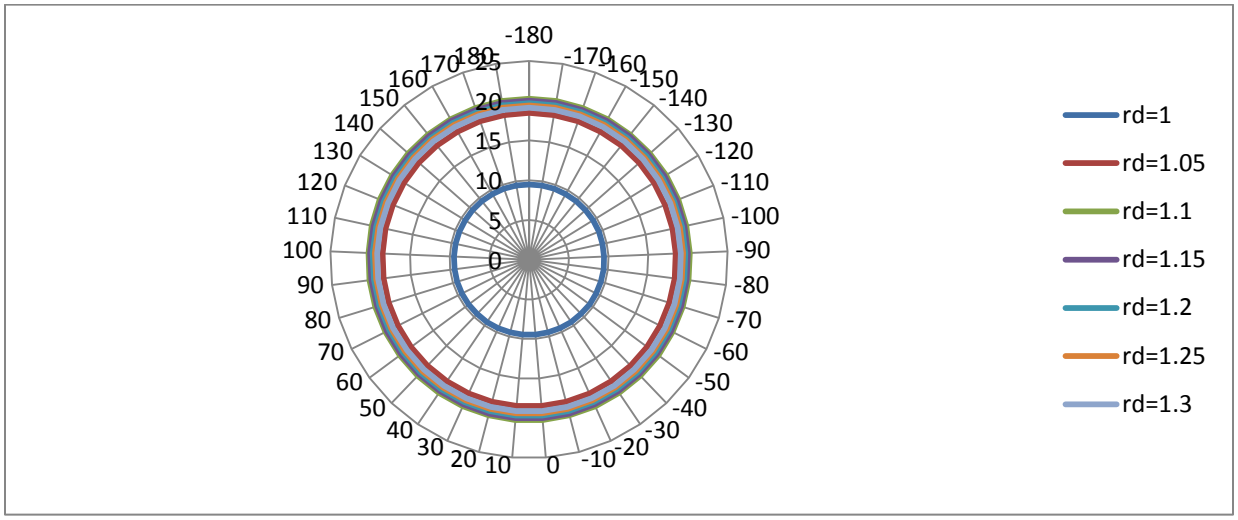

Figure 56: Hoop stresses around a wellbore at different specific radius values for a vertical well

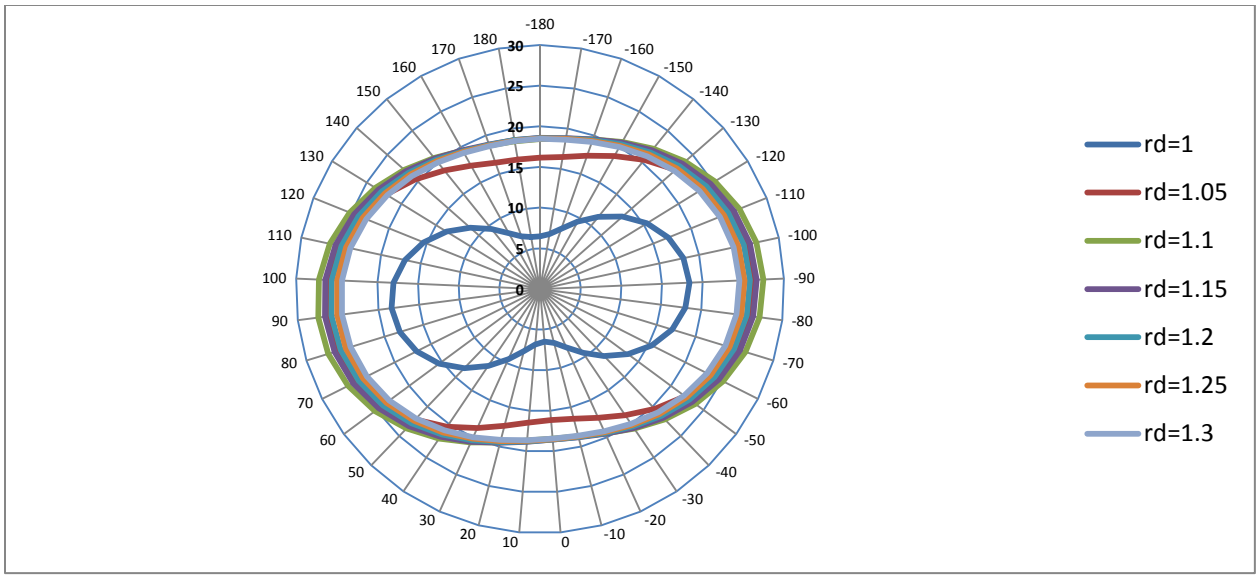

Figure 57: Hoop stresses around a wellbore at different specific radius values for a horizontal well

6.4.3 Axial Stress

Axial stresses tend to show the same behavior as the hoop stress. Only difference is the less eccentric shape of graph for the horizontal well.

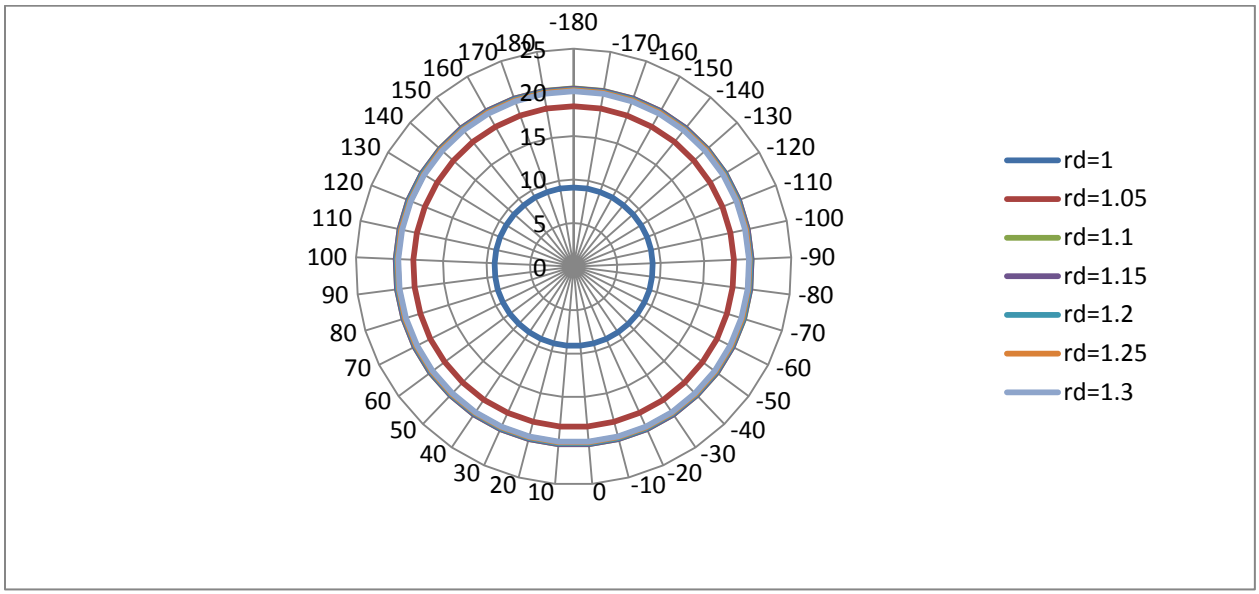

Figure 58: Axial stresses around a wellbore at different specific radius values for a vertical well

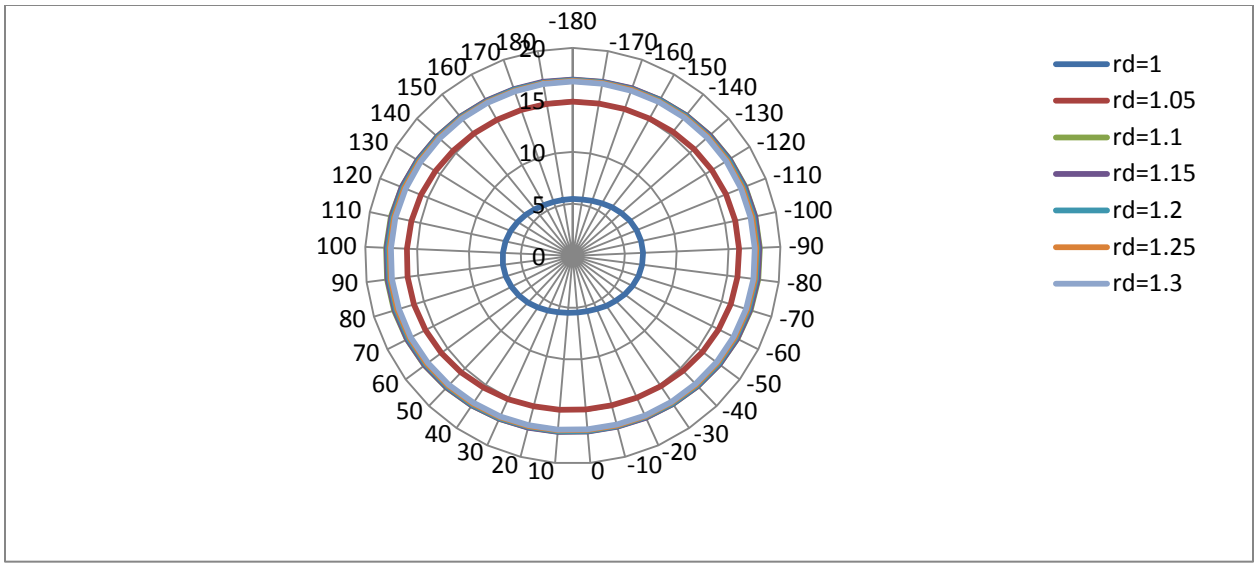

Figure 59: Axial stresses around a wellbore at different specific radius values for a horizontal well

6.4.4 Effective Collapse failure

The effective collapse stress for a vertical well tends to have the same magnitude around the wellbore for a specific well radius. Also, it is minimum at 90 degrees around the wellbore and maximum at 0 degrees around the wellbore for the horizontal well. Note that eccentricity in all the graphs is due one of the horizontal in-situ stresses value increase due to inclination.

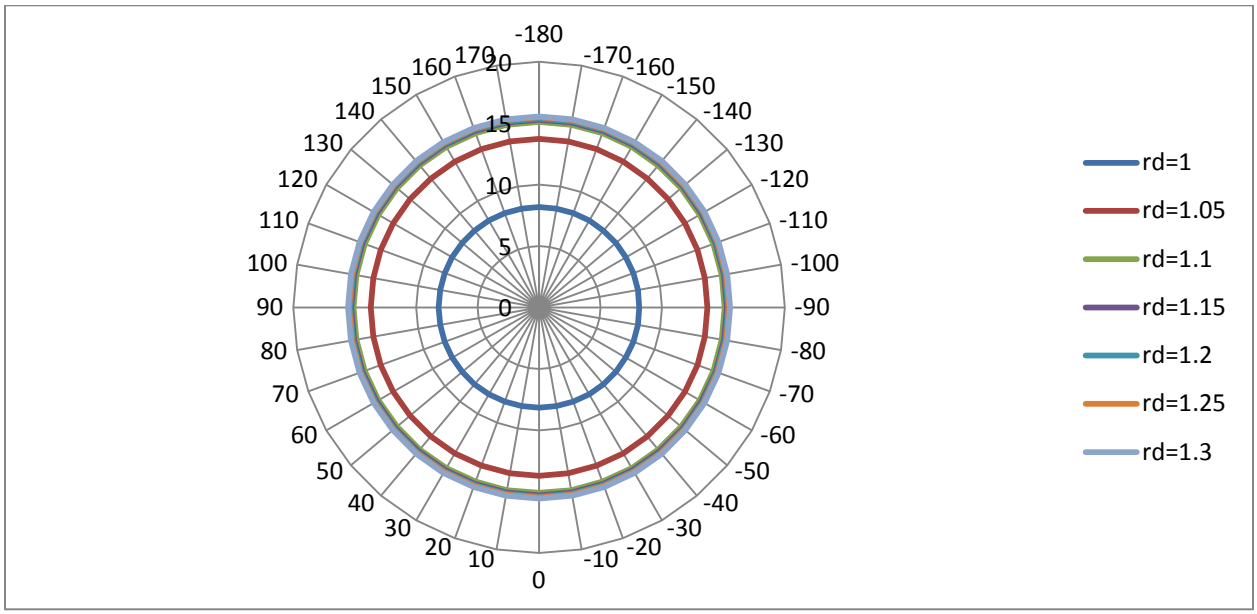

Figure 60: Effective collapse stresses around a wellbore at different specific radius values for a vertical well

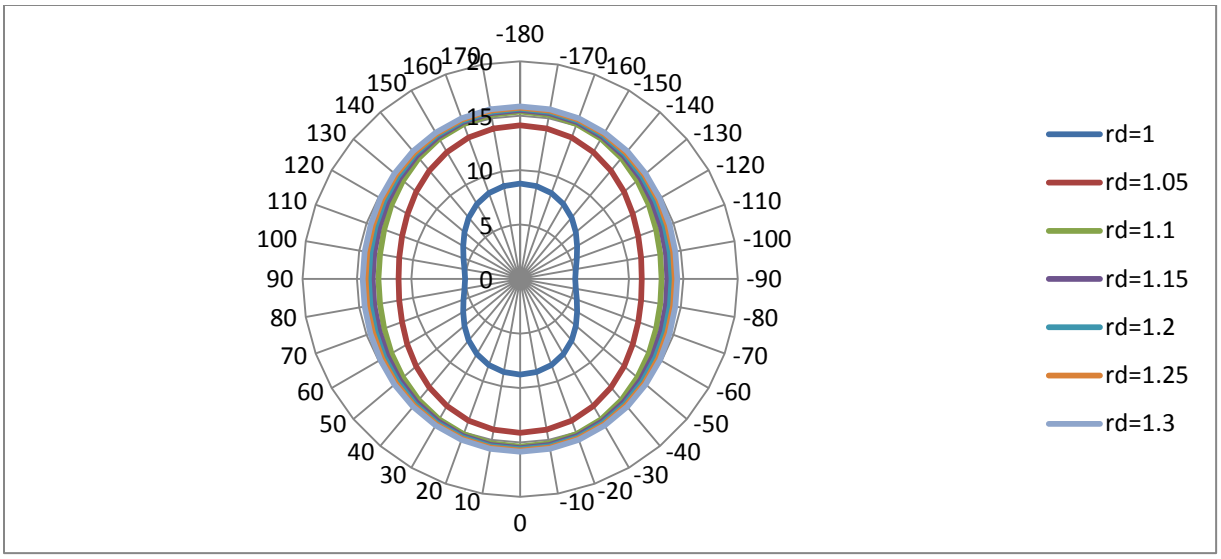

Figure 61: Effective collapse stresses around a wellbore at different specific radius values for a horizontal well

Figure 62 below shows the effective collapse stress at all well inclination angles. It can easily be concluded that for any specific radius away or at the wall, the effective collapse stress is a maximum at well inclination of zero degrees and minimum at a well inclination for 90 degrees. It tends to decrease slowly as the inclination of the well is increased to 90 degrees as seen below.

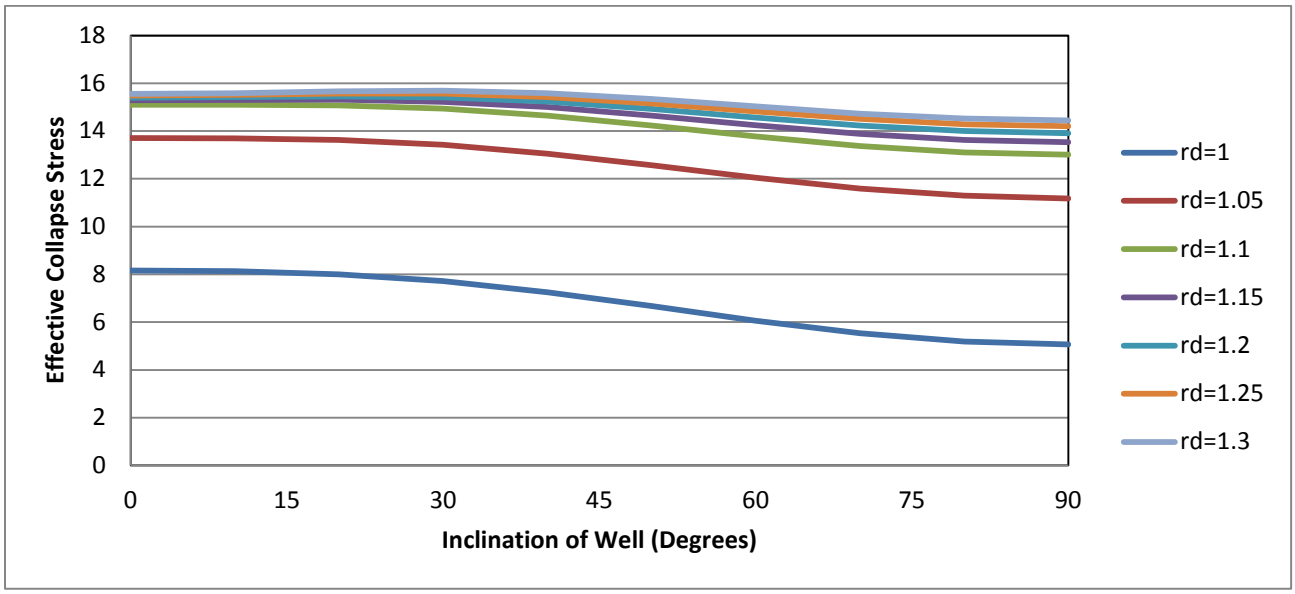

Figure 62: Effective collapse stress at different well inclination

7 Case Study

7.1 Introduction

Heidrun field was discovered in 1985 in the Haltenbanken area offshore Mid-Norway (G. Stjern 2003). Figure 63 below shows the location of this field on a map. The field is located in a very environmentally vulnerable area therefore the use of oil based mud is not possible (G. Stjern 2003). Water based muds are used on the fields which can be a problem for shale as water tend to swell the shale formation which exits in this field. Therefore, inhibitive like KCl is used in the water based mud which acted as reactive clay to drill wells on this field. All the wells were drilled on a Tension Leg Platform (TLP). Most of wells on the field are extended reach wells with inclination of wells in the range of 55 to 70 degrees (E. Fjær 2008). Also, the salt content in the mud was also reduced as this helped drilling a stable borehole. Reducing the salt content tends to increase the mud activity and a change in chemical effect on the pore pressure. A case study is initiated in order to see the chemical, thermal and poro-elastic effects on the wellbore wall on one of the wells on the Heidrun field.

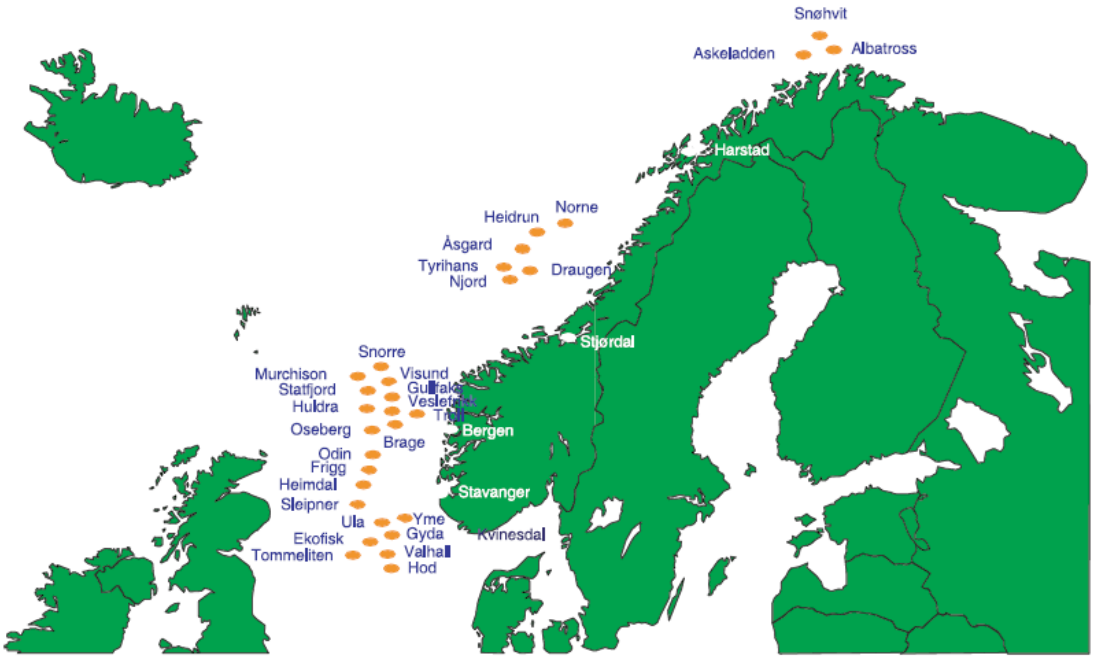

Fig. 1. Field location map offshore Norway.

Figure 63: Field location fo Heidrun field (G. Stjern 2003)

Before drilling the primary step is the design of the drilling program. The drilling program is used to avoid well instability problems. These well instabilities are collapse and well fracture. Figure 64 shows the well program.

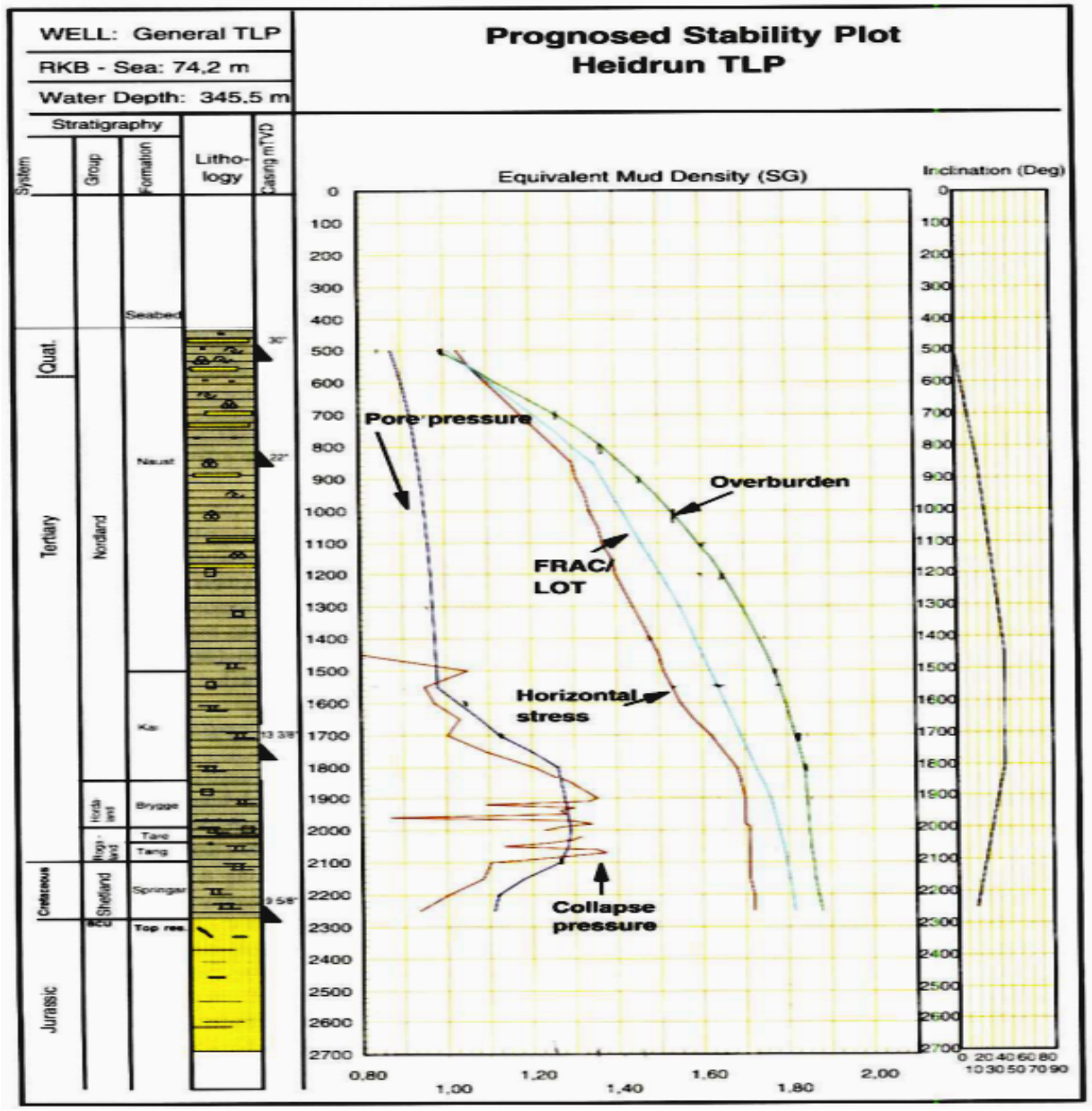

Figure 64: Prognosis stability plot for a typical Heidrun TLP well (G. Stjern 2003)

7.2 Model used for chemical and temperature

In order to investigate the poro-elastic, chemical and temperature effects on the well collapse pressure, a model was derived. Initially, Mohr-Coulomb model is used as listed above in equation 4.18 using stress transformations equation 3.4 to take into account the well inclination at all depths. In order to take into account the effects, the set of equations in equation 5.11 were coupled with the model which takes into account all the induced chemical and temperature stresses. At the wall, there is no change in pore pressure due to temperature. In order to calculate the change in pore pressure needed for the model, equation 5.9 was used to find the change in pore pressure. The model derived from for these effects are below for chemical, temperature and chemical and temperature.

$$P_w \leq \frac{3\sigma_x - \sigma_y - C_o - \alpha_o P_0^N (1 - \tan\alpha) - 2\eta P_0 - 2\eta P_\pi}{1 + \tan\alpha - 2\eta} \qquad 7.1$$

$$P_w \leq \frac{3\sigma_x - \sigma_y - C_o - \alpha_o P_0 (1 - \tan\alpha) + K}{1 + \tan\alpha - 2\eta} \qquad 7.2$$

$$P_w \leq \frac{3\sigma_x - \sigma_y - C_o - \alpha_o P_0^N (1 - \tan\alpha) - 2\eta P_0 - 2\eta P_\pi + K}{1 + \tan\alpha - 2\eta} \qquad 7.3$$

Where

$$K = \frac{E\alpha_m}{3(1-v)}(T_w - T_o) \qquad 7.4$$

$$\eta = \frac{\alpha_o(1-2v)}{1-v} \qquad 7.5$$

7.3 Sensitivity analysis

In order to perform sensitivity analysis and see which properties influence the well collapse pressure the most, first the data in Figure 64 above was digitized and Mohr-Coulomb collapse curve was generated using equation 4.18. The reason for choosing this equation out of the other equations was that the stresses calculated from the digitized date in Figure 64 were in the order $\sigma_\theta \geq \sigma_z > \sigma_r$. Once that was achieved, the above poro-elastic models equations were used to see the effects of chemical and temperature. All the properties for the analysis were taken from Table 8 above unless stated otherwise. The activity and the temperature values were changed as for a temperature, a temperature profile was used all along the well depth and for the activity the values in Table 8 were very high and were giving unrealistic results. Note that the normal 'Collapse' line in all the figures below is the line plotted from the equation 4.18 without any effects and is the reference line to see any effects. Activity was increased and decreased 5% in order to see the effect of it on the collapse pressure. All other parameters were increased and decreased by 10% to observe changes on the collapse pressure.

7.3.1 Activity of shale and mud

The chemical effects were investigated using the poro-elastic model for chemical effects only. The activity of shale and mud were taken as 0.87 and 0.915. The values were reversed to see the effect of activity on the chemical changes. Figure 65 was generated in excel using the above values and model. It can be seen that chemical effects change the collapse curve dramatically and has a big influence on the collapse curve. Since the activity of formation cannot be controlled, the activity of the drilling mud should be controlled by used of different additives or inhibitive in order to get desirable results. Figure 66 shows the effect of increasing and decreasing the activity of drilling fluid. It can be seen from the results that the change in activity have a very big impact on the collapse pressure.

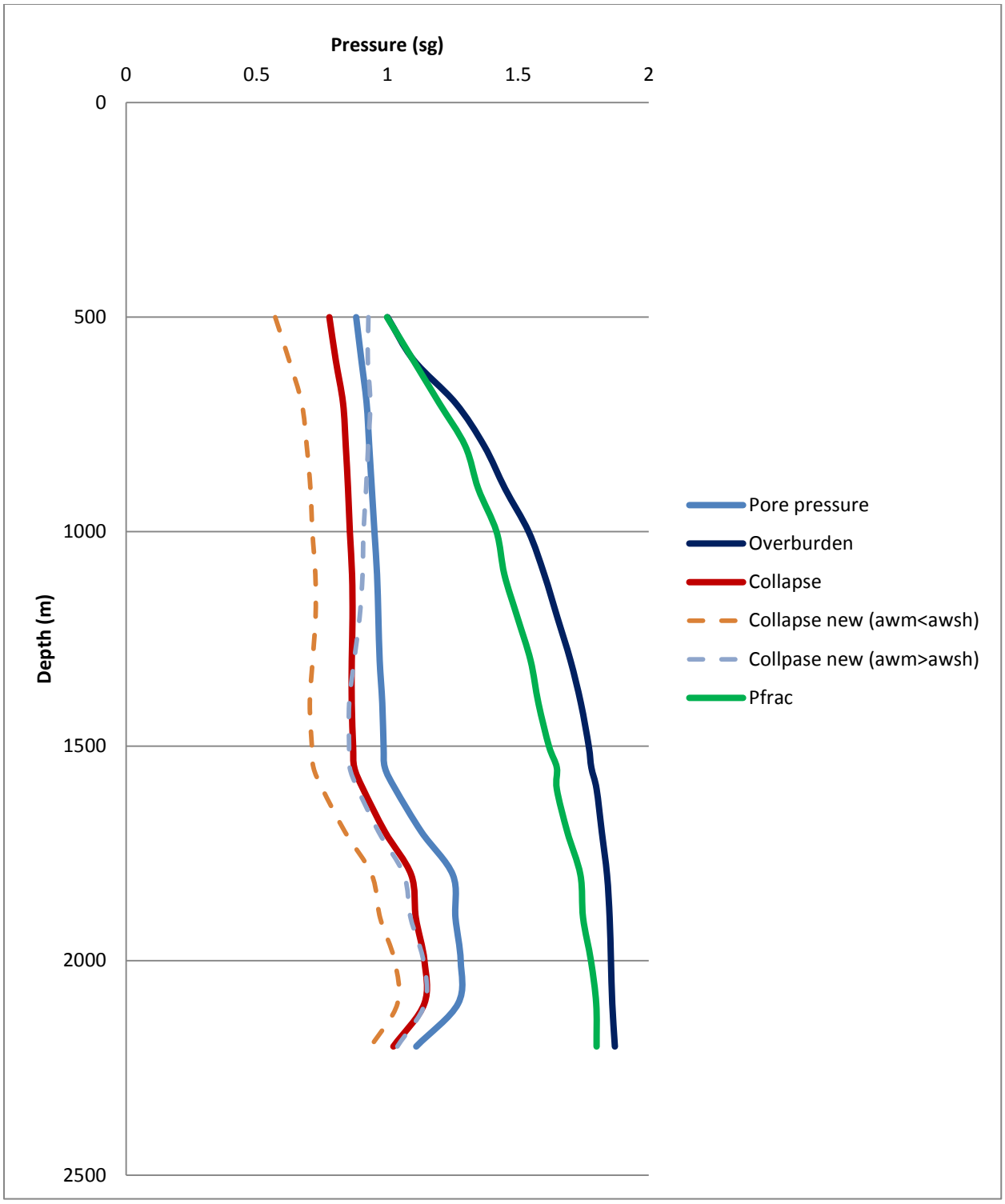

Figure 65: Collapse pressure graph for chemical effects

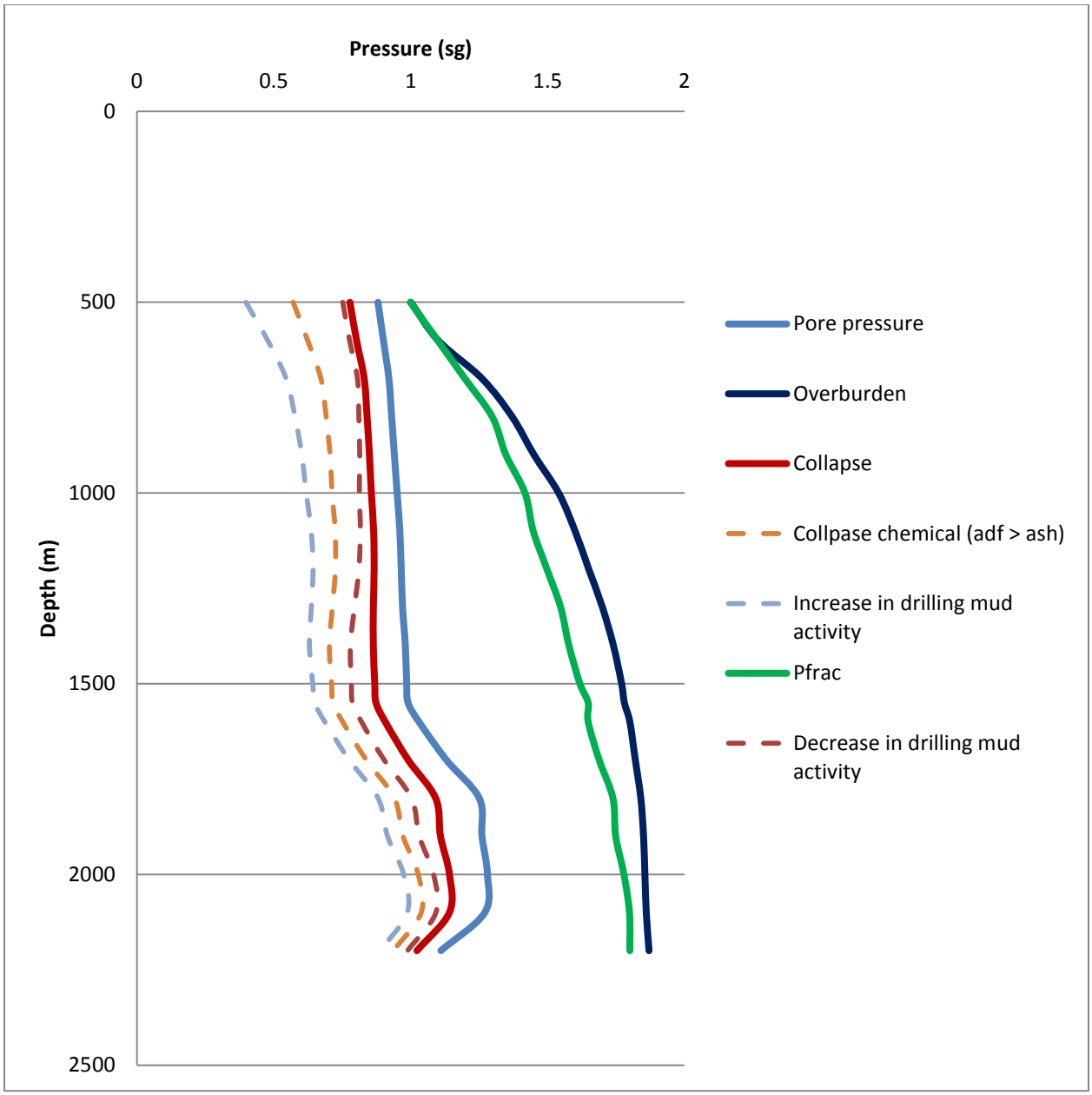

Figure 66: Collapse pressure graph for activity effects

7.3.2 Temperature effect

In order to get the effect of temperature only, the normal mode for Mohr-Coulomb is coupled with equation 7.4. The linear thermal expansion coefficient was taken as 15E-6 K^{-1} for weak shale (North Sea) and Young's modulus was taken to be 1000 MPa (E. Fjær 2008). The results below were achieved. It shows that the wall temperature also has a significant effect on the collapse pressure and this effect tends to disappear as the temperature difference of the wall and

formation reduces down the depth. This is due to the decrease in wall temperature gradient. For the wall and formation temperature profile along the depth, a temperature profile was generated. It can be seen in Figure 68. Digitized data used to generate the temperature profile can also be seen in Table 9 below.

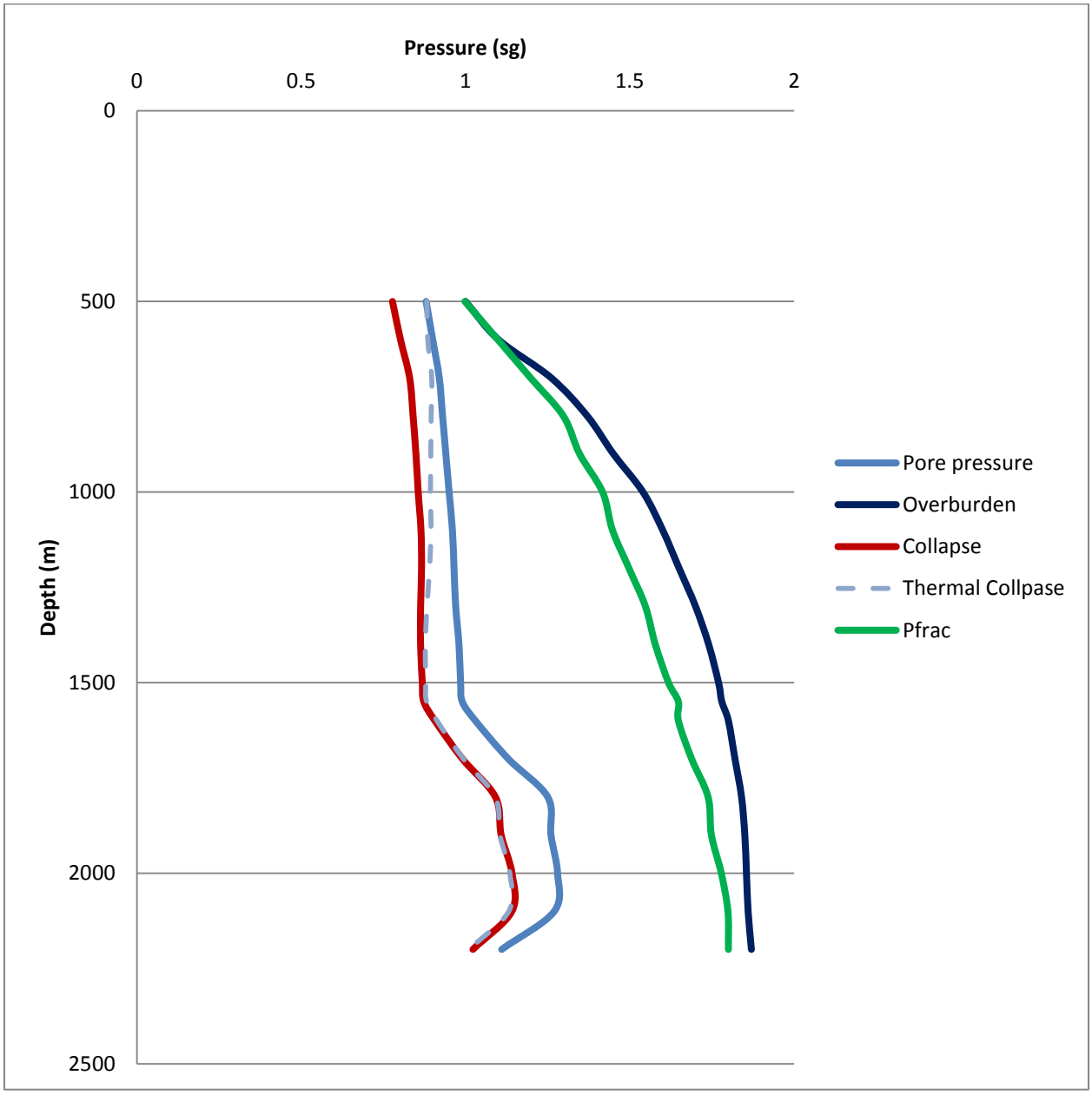

Figure 67: Collapse pressure graph for thermal effects

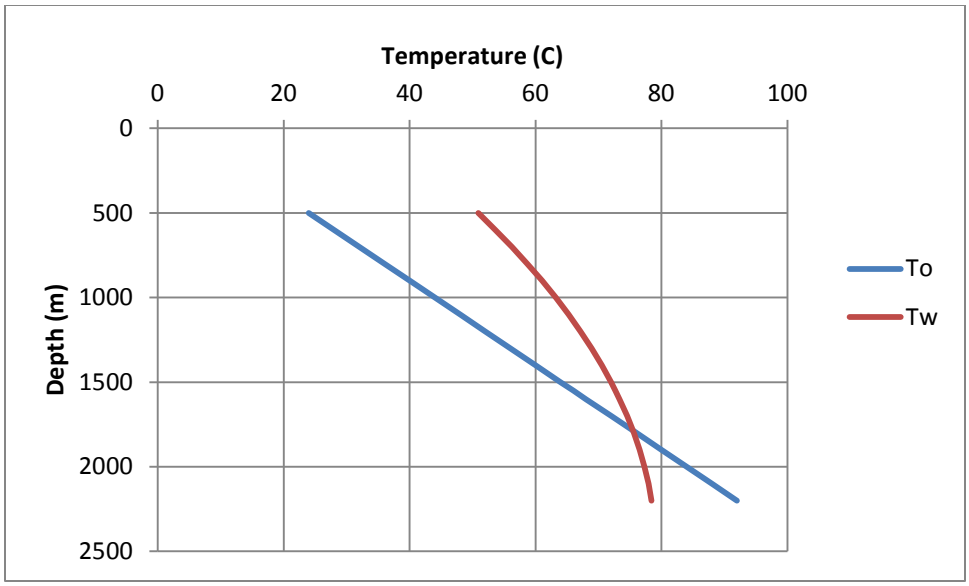

Figure 68: Formation and wall temperature profile with respect to depth

Depth (m)	To (°)	Tw (°)
500	24	50.895
600	28	53.635
700	32	56.235
800	36	58.695
900	40	61.015
1000	44	63.195
1100	48	65.235
1200	52	67.135
1300	56	68.895
1400	60	70.515
1500	64	71.995
1550	66	72.6825
1600	68	73.335
1700	72	74.535
1800	76	75.595
1900	80	76.515
2000	84	77.295
2100	88	77.935
2200	92	78.435

Table 9: Formation and wall temperature data at different depths

7.3.3 Temperature and chemical combined effect

When both results were combined, it can easily be concluded that the chemical effects dominate the temperature effects at the wall. But in the upper part of the formation, the collapse pressure exceeds even the fracture pressure due to very narrow mud weight window and high chemical and thermal effects in that region. Therefore it is very vital to evaluate these changes more thoroughly when generating the final results in the drill program.

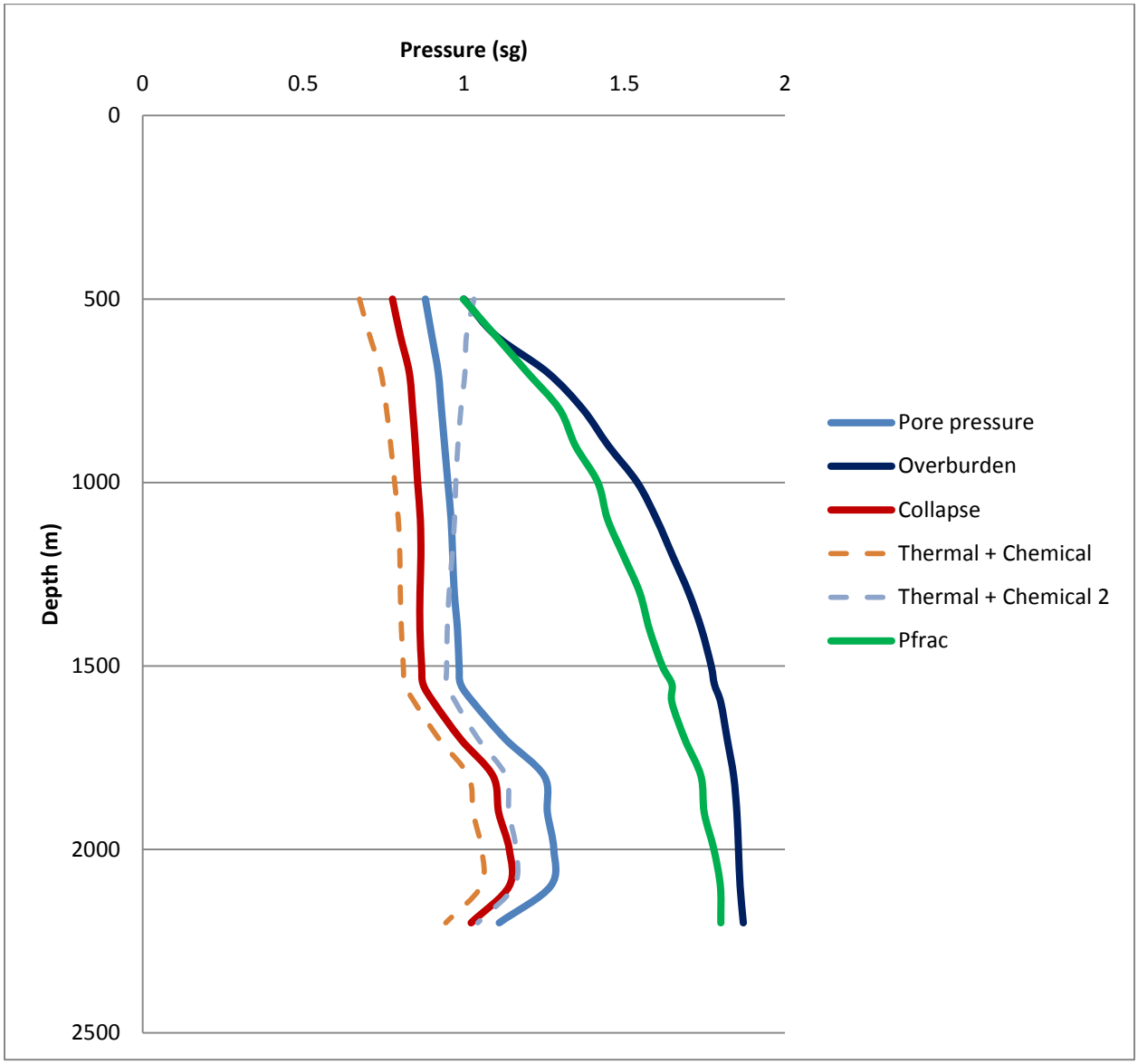

Figure 69: Collapse pressure graph for combined thermal and chemical effects

7.3.4 Biot's constant

Biot's constant value was increased and decreased by10 percent of its initial value to see the effect of this property on the collapse curve. As seen below in Figure 70, Biot's constant has a very strong effect on the collapse curve.

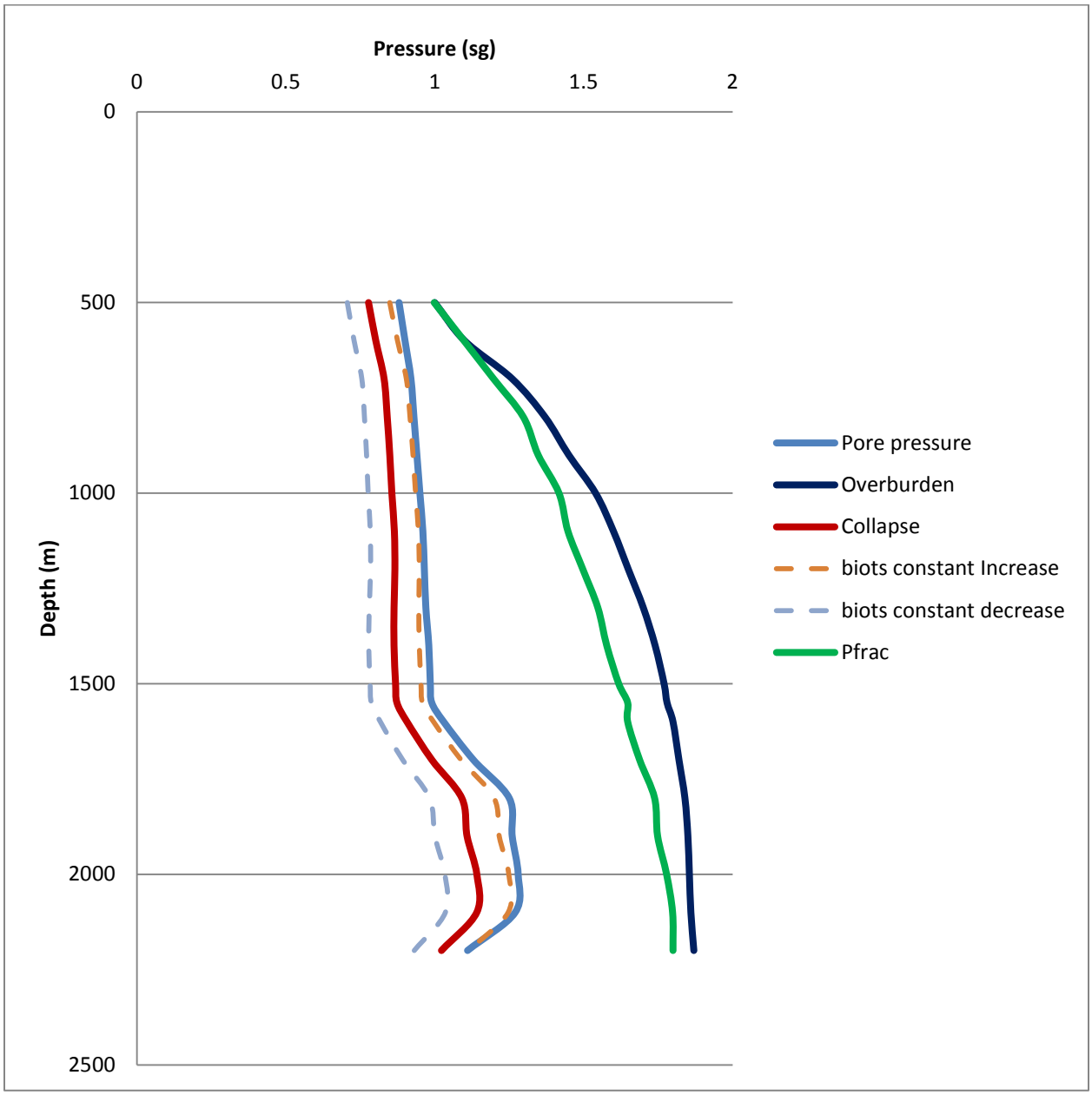

Figure 70: Collapse pressure graph for Biot's constant effects

7.3.5 Friction angle

The effect of friction angle was also seen in Figure 71. It can be seen that the change in friction angle does not affect the collapse curve that much and is less vital property when evaluating the collapse curve.

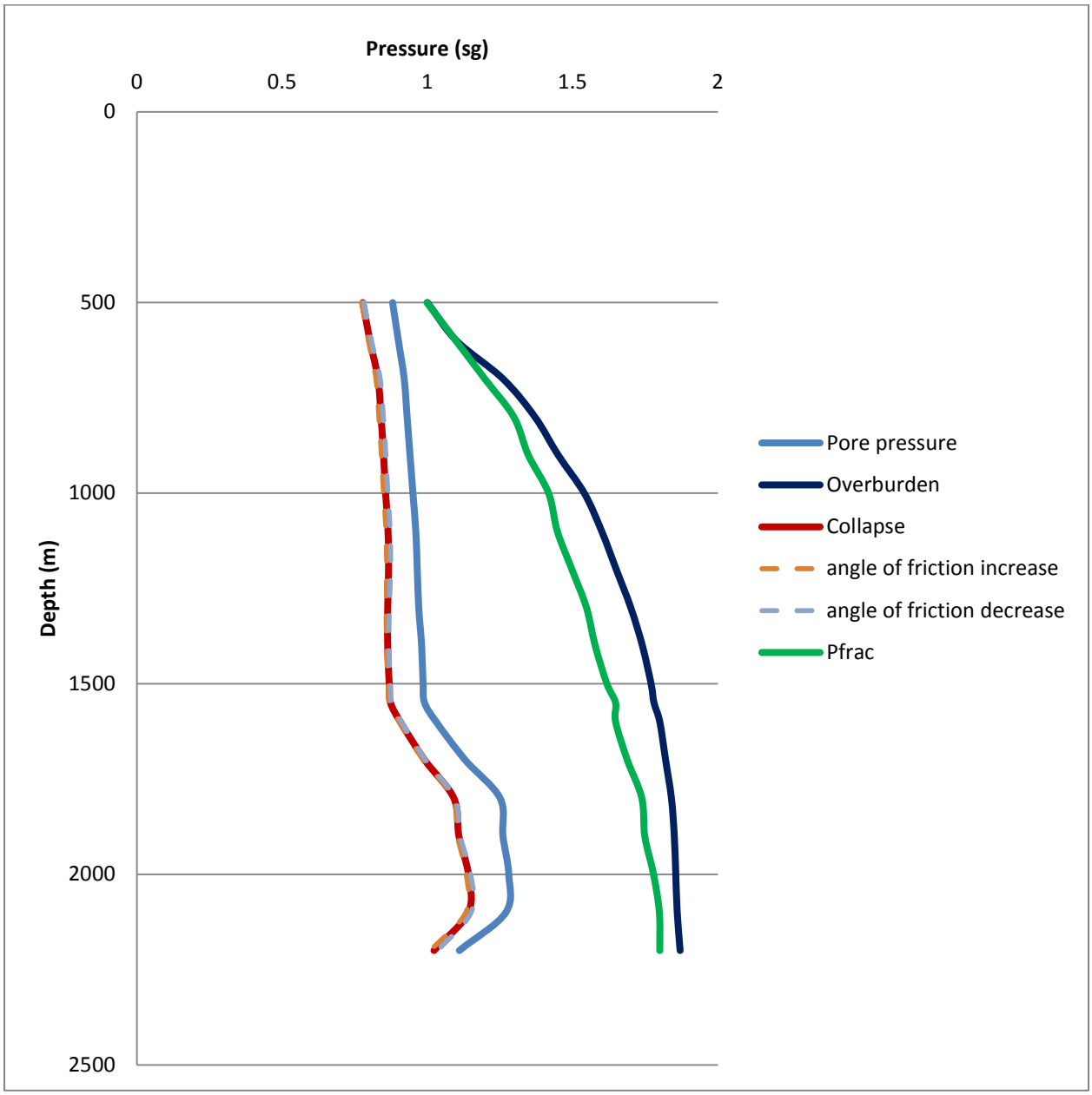

Figure 71: Collapse pressure graph for friction angle effects

7.3.6 Poisson's ratio

This property tends to show a little effect on the initial collapse curve. But in comparison to the Biot's constant, the effect is very small.

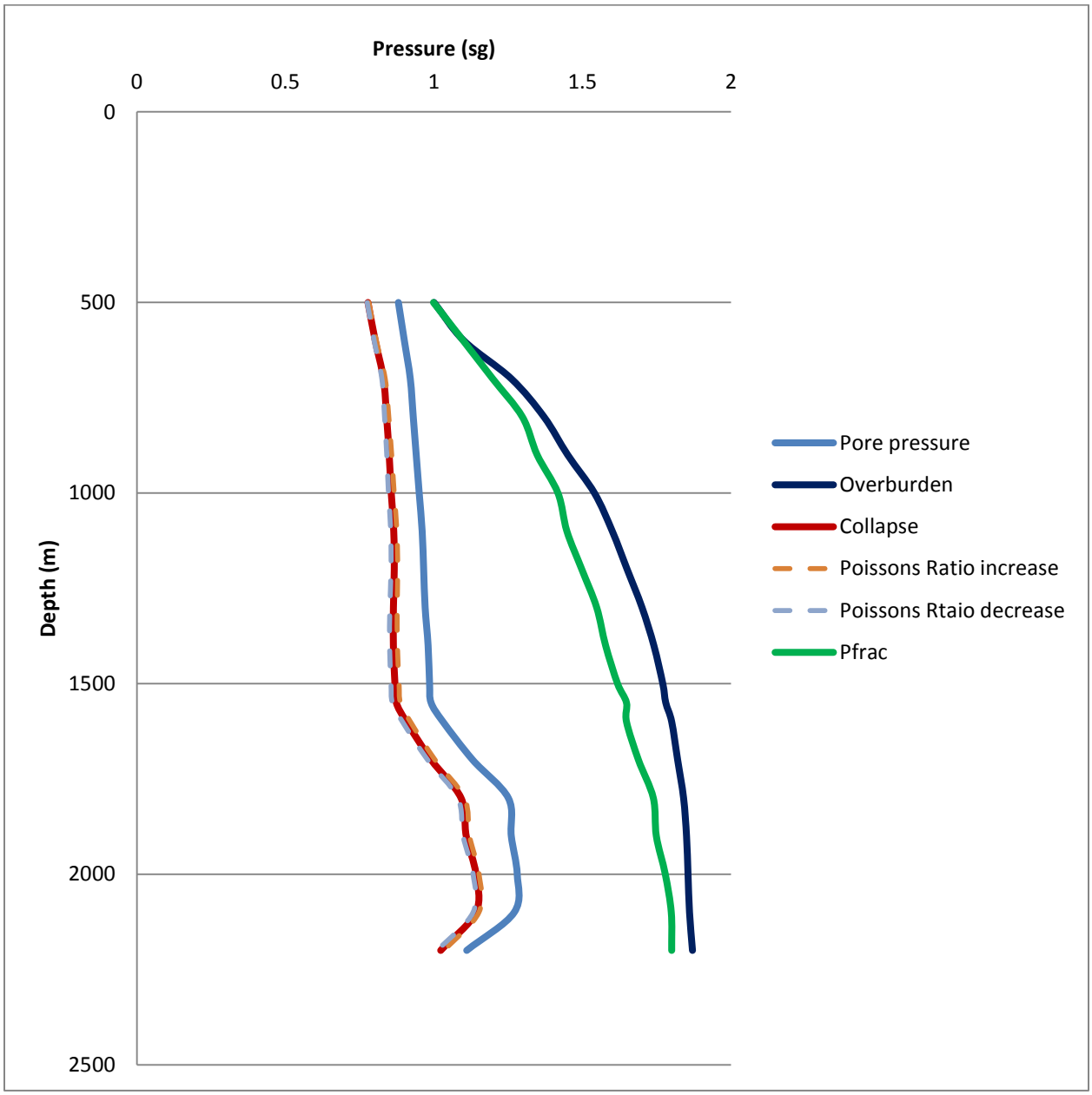

Figure 72: Collapse pressure graph for Poisson's ratio effects

7.3.7 Cohesive strength

The change is cohesive strength also shows very minute alterations to the collapse curve.

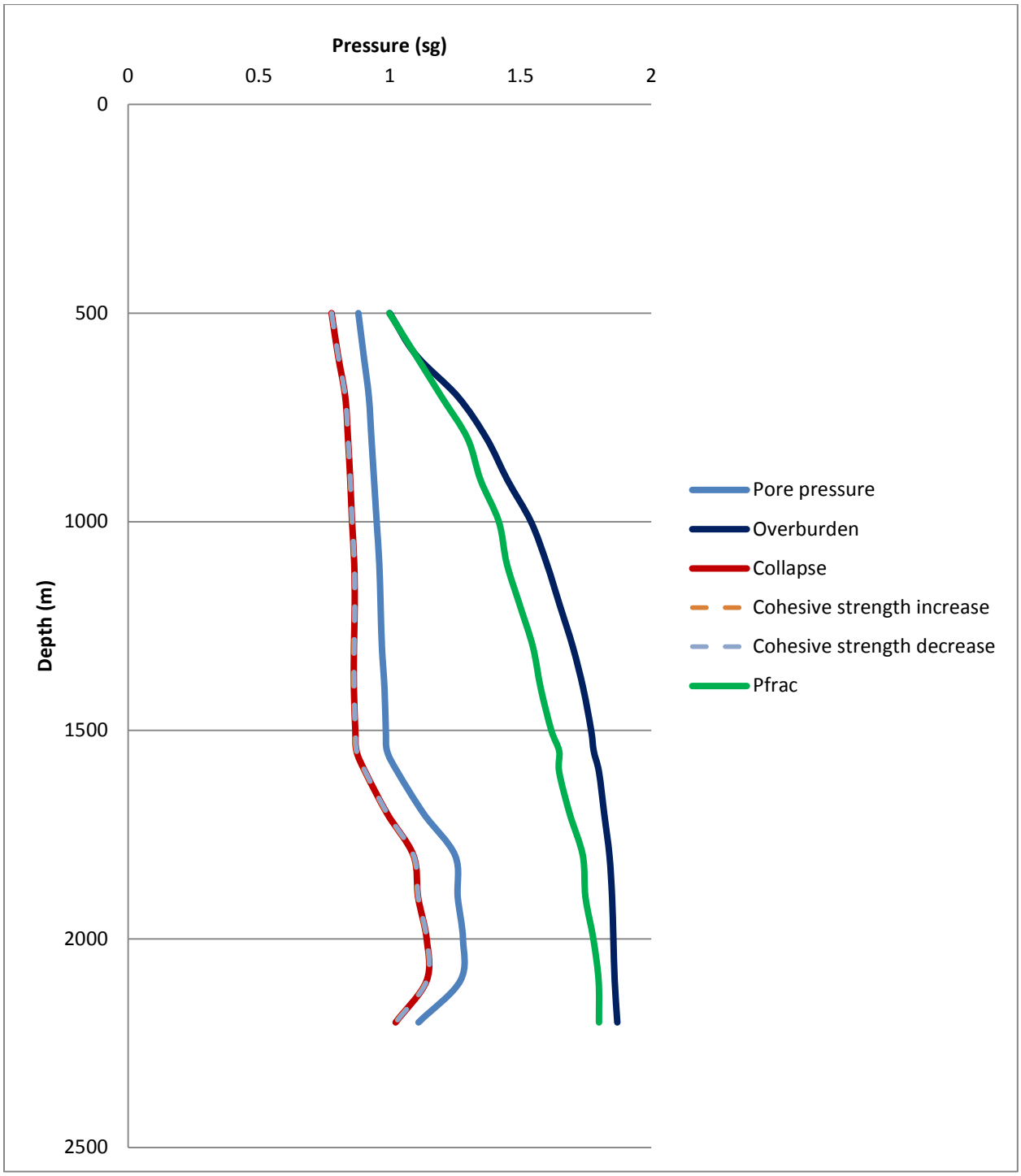

Figure 73: Collapse pressure graph for cohesive strength effects

7.3.8 Wall temperature

Wall temperature of the well was increase and decreased by 20 degrees in order to see the effect of it. In the upper depths, the increase and decrease had a significant effect in the curve whereas down the formation, the effect is becoming more and more insignificant.

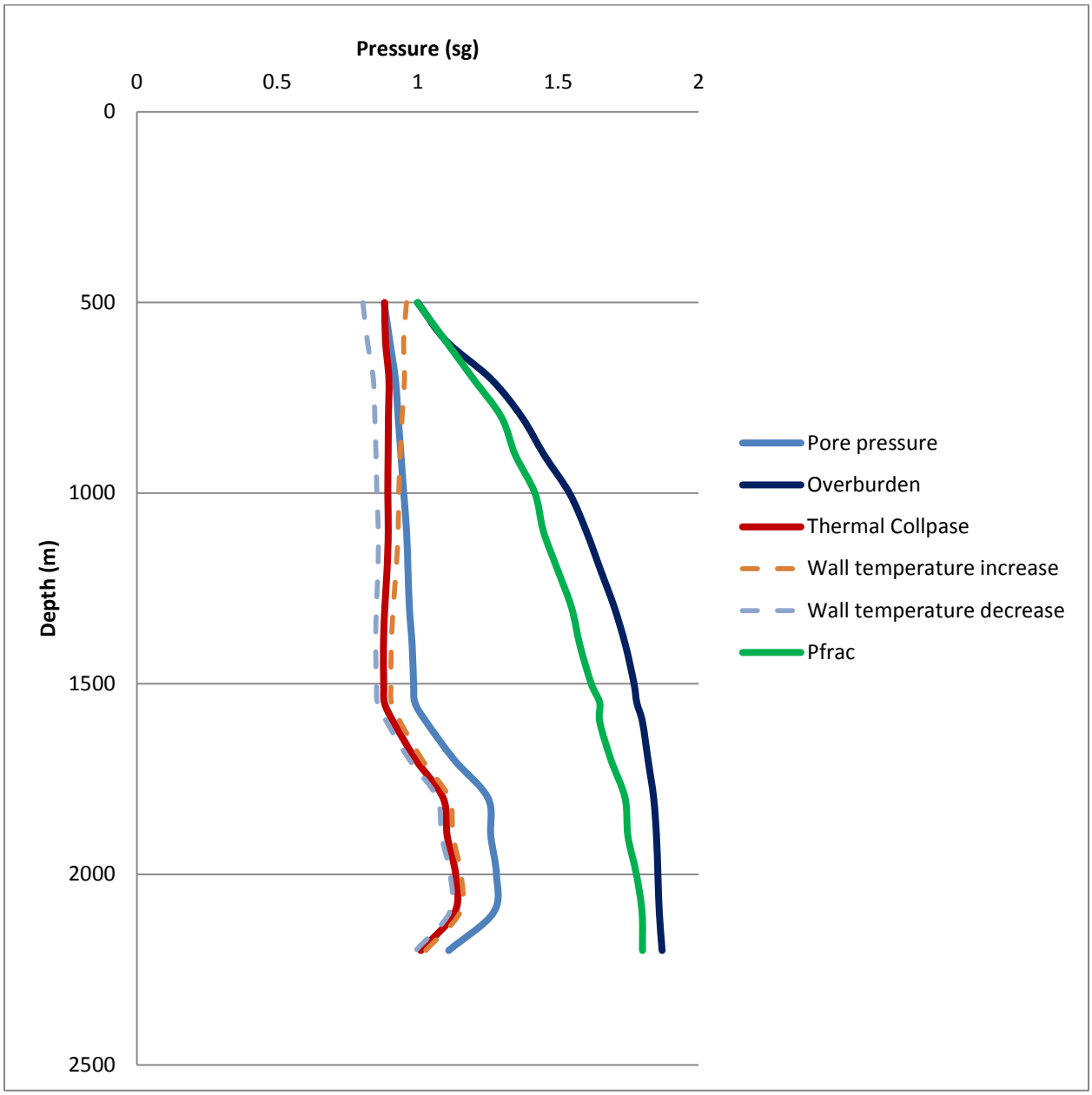

Figure 74: Collapse pressure graph for wall temperature effects

7.3.9 Discussion and Comparison

It can be seen from results in the case study that the activity of drilling fluid is the most dominating of all properties in terms of the changes on the collapse pressure. It can be seen that only a 5% change in this value changes the collapse pressure immensely. Figure 75 shows that if the drilling fluid activity is decreased, the collapse pressure will tend to return to its original position where there were no effects. This is because the difference of the formation and drilling fluid activity is reduced. Once this difference is increased the change in the well collapse pressure will be increased again. Therefore, even though it is the most dominating parameter, it can be controlled by altering the activity of drilling mud.

For other parameters, Biot's constant was proven to be the most dominating parameter as a change of 10% in this value resulted in large changes in the well collapse pressure. This can be seen below in Figure 76. Another important factor for the dominance of Biot's constant is that the horizontal in-situ stress was calculated from this value using equation 3.2. Therefore, the results also included the Biot's constant effect on the in-situ stresses. If the in-situ stresses are known using other models in equation 4.1 and 4.2, the results can be more accurate and a better representation of the Biot's constant effect on the collapse pressure can be known. Temperature is also a sensitive parameter in the upper depths of the formations where the change in collapse pressure due to temperature was very high. Figure 76 also included the well collapse pressure lines for other parameters too. The other properties showed very small changes and didn't alter the initial collapse pressure that much. But note that if all the values are overestimated or underestimated, the combination of the effects even for the small changes can amend the results greatly resulting in quite affective changes in well collapse pressure.

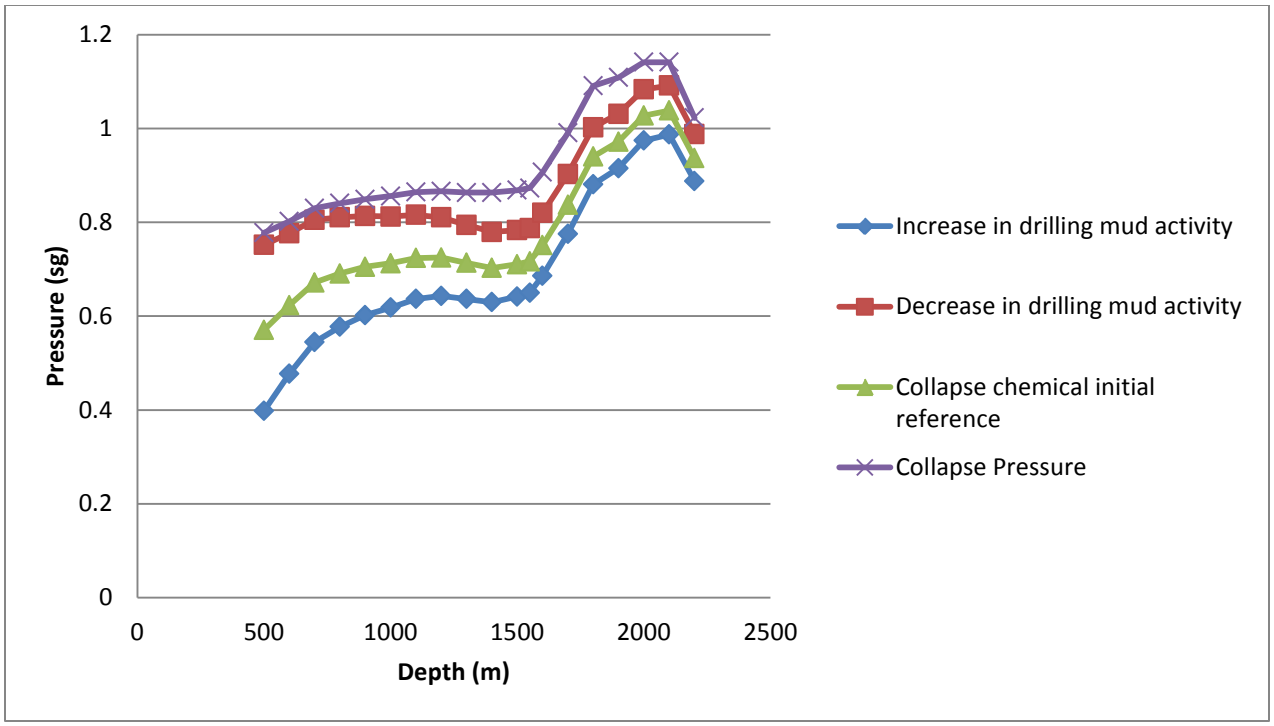

Figure 75: Collapse Pressure graph for change in drilling mud activity

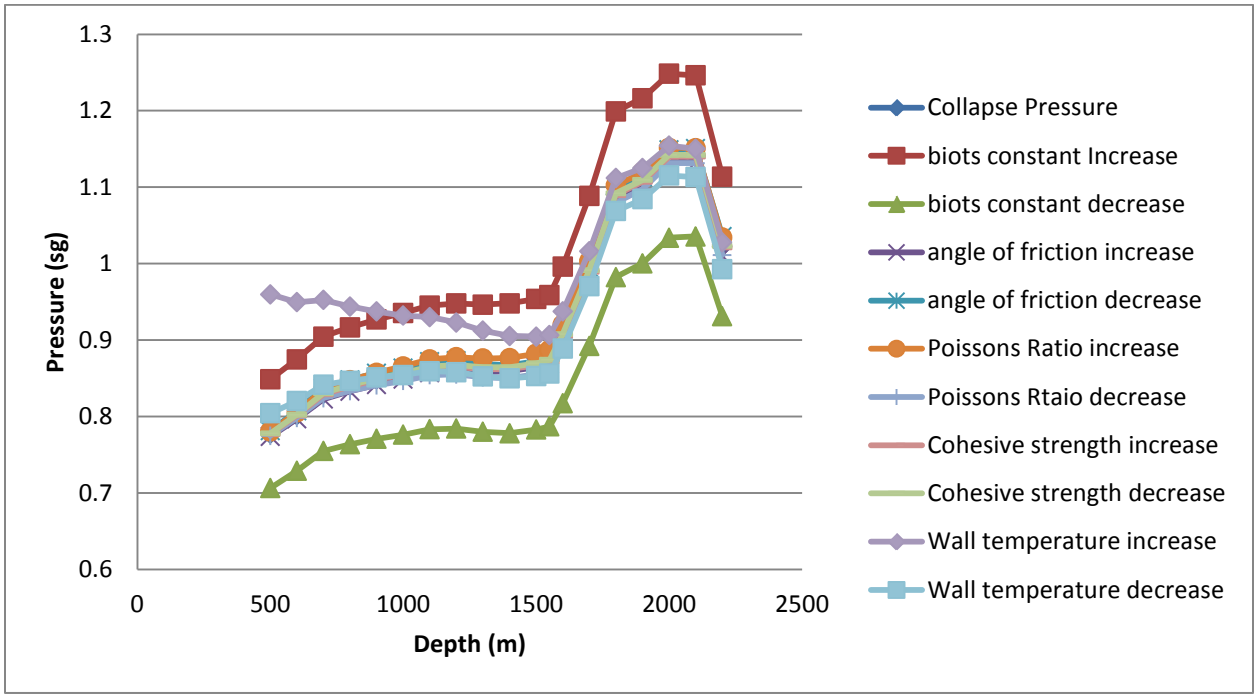

Figure 76: Collapse pressure graph for different scenarios

8 Conclusion

It was concluded from the simulations performed for different effects that the chemical and hydraulic diffusion effects were quite dominating at the wall of the wellbore. Both of these effects could be controlled by using right design for mud weight density for hydraulic diffusion affects as the higher the well pressure will be the greater will be the increase in pore pressure. Chemical effects can be controlled by changing the activity of the drilling fluid and can increase or decrease the pore pressure depending on the formation and drilling fluid activity. Thermal effects had no influence on pore pressure at the wall even though it was more dominating when moved away from wellbore wall. Also, cohesive strength reduces with respect to time because of which the effective collapse strength reduced significantly at the wall. An increase in pore pressure tends to decrease the effective collapse stress and vice versa.

For the case study, activity of the drilling fluid activity was the most sensitive parameter for the well collapse pressure. The second parameter that was found to be very sensitive to well collapse pressure after the activity of drilling fluid was the Biot's constant. A small increase in this value changed the well collapse pressure dramatically. Temperature was quite sensitive in the upper depths where the change in temperature between the formation and the wall was significantly high. All the other properties analyzed had very small effects on the well collapse pressure. In terms of chemical and thermal, the case study showed that chemical effects were far more dominating than the thermal effects for this Heidrun well program.

References

A.M. Al-Ajmi, R. W. Z. (2006). "Stability Analysis of vertical boreholes using the Mogi-Coulomb." International Jounal of Rock Mechanics and Mining Sciences **43**(8): 1200-1211.

Aadnøy, B. S. (2003). "Introduction to special issue on wellbore stability." Journal of Petroleum Science and Engineering **38**: 79-82.

B.S. Aadnøy, M. E. C. (1987). "Stability of highly inclined boreholes." SPE Drilling Engineering **2**(04): 364-374.

Bernt S. Aadnøy, R. L. (2011). Petroleum Rock Mechanics. USA, Gulf Professional Publishing.

C. Chen, M. E. C., M.M. Sharma & M. Yu (2001). Poroelastic chemical, and thermal effects on wellbore stability in shales. U.S. Symposium on Rock Mechanics. Washington D.C, American Rock Mechanics Association.

CFCF (2013). "Osmosis." from http://en.wikipedia.org/wiki/Osmosis.

Cosse, R. (1993). Basic of reservoir engineering. France, Editions Technip.

Dyni, J. R. (2006). "Geology and Resources of Some World Oil-Shale Deposits." USGS

5294.

E. Eseme, B. M. K., R. Littke (2012). "Evolution of petrophysical properties of oil shales during high-temperature compaction tests." Marine and Petroleum Geology **31**(1): 110-124.

E. Fjær, R. M. H., P. Horsrud, A.M. Raaen & R.Risnes (2008). Petroleum Related Rock Mechanics. Hungary, Elsevier publications.

Eaton, B. A. (1972). "Graphical method predicts geopressure worldwide." World Oil **182**: 51-56.

Eaton, B. A. (1975). "The equation for geopressure prediction from well logs." SPE 5544.

Ewy, G. C. R. T. (2005). "Thermoporoelastic Effect on Wellbore Stability." SPE **10**(02): 121-129.

F.J. Santarelli, S. C. (1995). "Do shale swell? A critical review of available evidence." SPE-29421-MS.

Fjær, E., et al. (2008). *Petroleum related rock mechanics*, Elsevier Science.

G. Stjern, A. A., P Horsrud (2003). "Local rock mechanical knowledge proves drilling performance in fractured formations at the Heidrun field." Journal of Petroleum Science and Engineering **38**(3-4): 83-96.

Gatlin, C. a. (1965). "Mechanical Anisotropies of laminated sedimentary rocks." SPE **5**(1).

Geoscience. "Shale." 2014, from http://geology.com/rocks/shale.shtml.

Horsrud, P. (2001). "Estimating Mechanical Properties of Shale from Empirical Correlations." SPE Drilling & Completion **16**(02): 68-73.

I.M. Breckels, H. A. M. v. E. (1982). "Relationship between horizontal stress and depth in sedimentary rocks." Journal of Petroleum Technology **34**(09): 2,191-192,199.

Institute, T. j. H. "Clay minerals."

J.C. Jaeger, N. G. W. C., and R.W. Zimmerman (2007). Fundamentals of rock mechanics. Singapore, Blackwell Publishing.

Jefferson, A. (2011). "Geology is destiny." from http://all-geo.org/highlyallochthonous/2011/01/geology-is-destiny-globally-mapping-permeability-by-rock-type/.

Jianguo Zhang, M. Y., T.M. Al-Bazali, Seehong Ong, M.E. Chenevert, M.M. Sharma (2006). "Maintaining the stability of deviated and horizontal wells." SPE.

Lal, M. (1999). "Shale stability: Drilling fluid interaction and shale strength." SPE 54356.

Lee, S. (1990). Oil Shale Technology. Florida, CRC Press.

Lianyang Zhang, P. C., K.C. Radha (2010). "Evaluation of rock strength criteria for wellbore stability analysis." International Jounal of Rock Mechanics and Mining Sciences **47**(8): 1304-1316.

Md. Aminul Islam, P. S. (2013). "An experimental investigation of shale mechanical properties through drained and undrained test mechanisms." Rock Mechanics rock engineering **46**: 1391-1413.

Mengjiao Yu, M. E. C., Mukul M. Sharma (2003). "Chemical-mechanical wellbore instability model instability model for shales." Journal of Petroleum Science and Engineering **38**: 131-143.

Mitchell, R. F., et al. (2011). *Fundamentals of drilling engineering*, Society of Petroleum Engineers.

Okiongbo, K. S. (2011). "Petrophysical Properties of North Sea Shales." Research Journal of Applied Sciences **3**(1): 46-52.

Oort, E. v. (2003). "On the physical and chemical stability of shales." Journal of Petroleum Science and Engineering **38**: 213-235.

Ronald Steiger, P. R., Leung, K. peter (1992). "Quantitative Determination of the Mechanical Properies of Shales." SPE **7**.

S. Hillier, G. R., I Sims and JC Cripps (2006). "Clay materials used in construction, A mineralogical and chemical data." Engineering Geology speical publications **21**: 449-459.

S.O. Osisanya, M. E. C. (1996). "Physico chemical modelling of wellbore stability in shale formations." Journal of Canadian Petroleum Technology **35**(02).

Soroush, D. H. (2013). Shale Gas Geomechanics. Stavanger, European Association of Geosciences & Engineers

SWACO, M. Drilling fluids and Engineering handbook.

Venkanna, B. K. (2010). Fundamentals of heat and mass transfer. New Delhi, PHI Learning.

Weaver, D. B. S. C. E. (1965). "The mineralogical composition of shales." Journal of Sedimenatry Reseacrh **35**: 213-222.

Appendix

M-file for the equation 5.9 to calculate the thermal, chemical and hydraulic diffusion effects

```
function [porep]=porep;
```

```
po=0.01538*4352.5;   % Pore pressure
ppi=-(0.1*0.462*375.7*log(0.78/0.915));    %chemical potential
rw=0.127;       % radius of well
r=[0.127 0.13335 0.1397 0.14605 0.1524 0.15875 0.1651]%specific radius
c=3.4e-10;          %hydraulic diffusivity
pw=0.0180*4352.5;   % well pressure
k=0.124;            %coupling coefficient
co=9.54e-7;         %thermal diffusivity
Tw=350.7;           %temperature of wall
To=375.7;           %temperature of formation
t=864000;           %time 10 hours
for m=1:length(t)
    porep(m,:)=po+((pw-ppi-po).*(sqrt(rw./r).*(erfc((r-
rw)./(2.*sqrt(c.*t(m)))))))-((k*(Tw-To)/(1-(c/co))).*(sqrt(rw./r).*((erfc((r-
rw)./(2.*sqrt(c.*t(m))))))-(erfc((r-rw)./(2.*sqrt(co.*t(m)))))));
end
hold on
plot(r./rw,porep(1,:),'b');
hold off
```

M-file for the equation 5.9 to calculate the thermal, chemical and hydraulic diffusion effects at different times

```
function [porep]=time;
po=0.01538*4352.5;
ppi=-(0.1*0.462*375.7*log(0.78/0.915));
rw=0.127;
r=[0.127:0.001:0.1651];
c=3.4e-10;
pw=0.0180*4352.5;
k=0.124;
co=9.54e-7;
Tw=350.7;
To=375.7;
t=[60 3600 36000 864000];
for m=1:length(t)
    porep(m,:)=po+((pw-ppi-po).*(sqrt(rw./r).*(erfc((r-
rw)./(2.*sqrt(c.*t(m)))))))-((k*(Tw-To)/(1-(c/co))).*(sqrt(rw./r).*((erfc((r-
rw)./(2.*sqrt(c.*t(m))))))-(erfc((r-rw)./(2.*sqrt(co.*t(m)))))));
end
%
hold on
plot(r./rw,porep(1,:),'b');
plot(r./rw,porep(2,:),'r');
plot(r./rw,porep(3,:),'k');
plot(r./rw,porep(4,:),'g');
hold off
```